

The SAMI Galaxy Survey: stellar population and structural trends across the Fundamental Plane

Francesco D'Eugenio^{1,2*}, Matthew Colless^{2,3}, Nicholas Scott^{4,3}, Arjen van der Wel¹, Roger L. Davies⁵, Jesse van de Sande^{4,3}, Sarah M. Sweet⁶, Sree Oh^{2,3}, Brent Groves⁷, Rob Sharp², Matt S. Owers^{8,9}, Joss Bland-Hawthorn^{4,3}, Scott M. Croom^{4,3}, Sarah Brough^{3,10}, Julia J. Bryant^{4,3,11}, Michael Goodwin¹¹, Jon S. Lawrence¹¹, Nuria P. F. Lorente¹¹ and Samuel N. Richards¹²

¹*Sterrenkundig Observatorium, Universiteit Gent, Krijgslaan 281 S9, B-9000 Gent, Belgium*

²*Research School of Astronomy and Astrophysics, Australian National University, Canberra, ACT 2611, Australia*

³*ARC Centre of Excellence for All Sky Astrophysics in 3 Dimensions (ASTRO 3D), Australia*

⁴*Sydney Institute for Astronomy, School of Physics, The University of Sydney, NSW, 2006, Australia*

⁵*Sub-department of Astrophysics, Department of Physics, University of Oxford, Denys Wilkinson Building, Keble Road, Oxford OX1 3RH, UK*

⁶*School of Mathematics and Physics, University of Queensland, Brisbane, QLD 4072, Australia*

⁷*International Centre for Radio Astronomy Research (ICRAR), University of Western Australia, Crawley, WA 6009, Australia*

⁸*Department of Physics and Astronomy, Macquarie University, NSW 2109, Australia*

⁹*Astronomy, Astrophysics and Astrophotonics Research Centre, Macquarie University, Sydney, NSW 2109, Australia*

¹⁰*School of Physics, University of New South Wales, NSW 2052, Australia*

¹¹*Australian Astronomical Optics, Macquarie University, Sydney, NSW 2109, Australia*

¹²*SOFIA Science Center, USRA, NASA Ames Research Center, Building N232, M/S 232-12, P.O. Box 1, Moffett Field, CA 94035-0001, USA*

Accepted 2021 April 20. Received 2021 April 14; in original form 2021 March 4

ABSTRACT

We study the Fundamental Plane (FP) for a volume- and luminosity-limited sample of 560 early-type galaxies from the SAMI survey. Using r -band sizes and luminosities from new Multi-Gaussian Expansion (MGE) photometric measurements, and treating luminosity as the dependent variable, the FP has coefficients $a = 1.294 \pm 0.039$, $b = 0.912 \pm 0.025$, and zero-point $c = 7.067 \pm 0.078$. We leverage the high signal-to-noise of SAMI integral field spectroscopy, to determine how structural and stellar-population observables affect the scatter about the FP. The FP residuals correlate most strongly (8σ significance) with luminosity-weighted simple-stellar-population (SSP) age. In contrast, the structural observables surface mass density, rotation-to-dispersion ratio, Sérsic index and projected shape all show little or no significant correlation. We connect the FP residuals to the empirical relation between age (or stellar mass-to-light ratio Υ_*) and surface mass density, the best predictor of SSP age amongst parameters based on FP observables. We show that the FP residuals (anti-)correlate with the residuals of the relation between surface density and Υ_* . This correlation implies that part of the FP scatter is due to the broad age and Υ_* distribution at any given surface mass density. Using virial mass and Υ_* we construct a simulated FP and compare it to the observed FP. We find that, while the empirical relations between observed stellar population relations and FP observables are responsible for most (75%) of the FP scatter, on their own they do not explain the observed tilt of the FP away from the virial plane.

Key words: galaxies: elliptical and lenticular, cD – galaxies: spiral – galaxies: formation – galaxies: evolution – galaxies: stellar content

1 INTRODUCTION

The Fundamental Plane (FP) is a 2-dimensional empirical relation between three galaxy observables: physical size (R),

* E-mail: francesco.deugenio@gmail.com

root mean square velocity along the line of sight (σ) and surface brightness (I ; Djorgovski & Davis 1987; Dressler et al. 1987). By connecting distance-independent σ and I to distance-dependent R , the FP can be used as a distance indicator in cosmology (e.g. Hudson et al. 1999; Colless et al. 2001; Beutler et al. 2011; Johnson et al. 2014). Tension between different determinations of the cosmological parameters (Planck Collaboration et al. 2016; Riess et al. 2016), as well as its use to map peculiar velocities, mean that the FP remains a critical tool for cosmology (e.g. Springob et al. 2014; Scrimgeour et al. 2016; Said et al. 2020). In addition, there are several reasons why the FP remains a critical benchmark for galaxy evolution studies. The tightness of the FP (scatter of 20–25%, Jørgensen et al. 1996, Hyde & Bernardi 2009, Magoulas et al. 2012, hereafter: M12) provides a strong constraint to theory, limiting the rate and strength of physical processes that drive galaxies away from the plane (e.g. Kobayashi 2005). Moreover, the FP enables us to probe - albeit not directly - the scaling relations of dark matter and initial mass function (IMF; e.g. Prugniel & Simien 1997; Graves & Faber 2010), thus constraining the present-day structure of local galaxies. Finally, the advent of large-aperture (8-10m) telescopes opened a window to study how the FP changes over cosmic time (van Dokkum & Stanford 2003; van der Wel et al. 2004; Wuyts et al. 2004), a subject that continues to this day, with studies reporting either evolution (Saracco et al. 2020), weak evolution (Saglia et al. 2010, 2016; Oldham et al. 2017; Dalla Bontà et al. 2018) or no evolution (Holden et al. 2010; Prichard et al. 2017; de Graaff et al. 2020). For all these reasons, a better understanding of the FP will improve our understanding of galaxies and potentially increase its precision and accuracy as a tool for cosmology.

The FP is physically rooted in the virialised nature of galaxies: the scalar virial theorem links dynamical mass, size and specific kinetic energy, thus constraining these observables on the virial (or mass) plane (Djorgovski & Davis 1987, Dressler et al. 1987, Cappellari et al. 2006, hereafter: C06, Cappellari et al. 2013a, hereafter: C13). If we use projected half-light radius (R_e) to measure size and root mean square velocity along the line of sight inside an aperture of radius R_e (σ_e) to measure kinetic energy, the virial mass can be expressed by

$$\log M_{\text{vir}} = \log \kappa + 2 \log \sigma_e + \log R_e - \log G \quad (1)$$

where G is the gravitational constant and κ is a parameter which encodes the possibility of ‘non-homology’, that is of systematic differences in galaxy structure along and orthogonal to the FP (cf. Bender et al. 1992; Graham & Colless 1997; Prugniel & Simien 1997). Equation (1) defines a geometric plane in the logarithmic space of $(\sigma_e, R_e, M_{\text{vir}})$. To obtain the FP, we further introduce the stellar mass-to-light ratio (Υ_* , assuming a fiducial Chabrier initial mass function, IMF; Chabrier 2003), the stellar mass-to-light ratio assuming a non-standard IMF (Υ_{IMF}) and the stellar-to-total mass fraction within one effective radius (f_*). With these definitions, the FP can be expressed as

$$\log L = \log \kappa + 2 \log \sigma_e + \log R_e - \log G - \log \Upsilon_* + \log f_* - \log(\Upsilon_{\text{IMF}}/\Upsilon_*) \quad (2)$$

where κ , f_* , Υ_* and $\Upsilon_{\text{IMF}}/\Upsilon_*$ may be (possibly indirect)

functions of both σ_e and R_e . Empirically, the FP is commonly expressed as

$$\log R_e = a \log \sigma_e + b \log I_e + c \quad (3)$$

where I_e is the mean surface brightness inside one R_e (in this formulation, the virial prediction is $a = 2$ and $b = -1$). In this work however, following C13, we use the alternative expression

$$\log L = a \log \sigma_e + b \log R_e + c \quad (4)$$

because it reduces correlated noise between R_e and L and is easier to interpret. While the observed mass plane is consistent with the virial plane ($a = 2$ and $b = 1$, C13), the FP has systematically different coefficients (Djorgovski & Davis 1987; Dressler et al. 1987). Geometrically, this difference means that the FP is tilted (or rotated) with respect to the virial plane. By comparing equations (1) and (2), the FP tilt must arise from systematic variations of κ , Υ_* , f_* and/or $\Upsilon_{\text{IMF}}/\Upsilon_*$ with σ_e and R_e .

In addition to its tilt, the observed FP also differs from the mass plane in that the latter is consistent with no intrinsic scatter (C13), whereas the FP has finite scatter (Jørgensen et al. 1996). The FP intrinsic scatter is critical to cosmology, because it represents a hard limit to its precision as a distance estimator (M12). Therefore, understanding the origin of this scatter is important to understanding if it can be reduced, thereby improving the FP as a tool for cosmology. From equation (2), the FP scatter must originate from galaxy-to-galaxy variations in κ , Υ_* , f_* and/or $\Upsilon_{\text{IMF}}/\Upsilon_*$ at fixed σ_e and R_e . Therefore, the fact that the FP is ‘tight’ requires either that these galaxy observables have narrow distributions at fixed σ_e and R_e , or, alternatively, that these distributions are correlated in such a way as to decrease the FP scatter (FP ‘fine-tuning’, Ciotti et al. 1996 - but see Chiu et al. 2017 for a different view). This fine-tuning requirement provides an additional constraint to galaxy evolution theory.

A satisfactory understanding of the FP requires (i) determining κ , Υ_* , f_* and $\Upsilon_{\text{IMF}}/\Upsilon_*$ as functions of σ_e and R_e and (ii) using these functions in equation (2) to reproduce the observed FP. The FP intrinsic scatter must also be consistent with the combined (and possibly correlated) scatter of these input galaxy properties at fixed σ_e and R_e . Unfortunately, measuring f_* and $\Upsilon_{\text{IMF}}/\Upsilon_*$ is challenging, because dark matter (in the definition of f_*) cannot be observed directly and because low-mass stars (for $\Upsilon_{\text{IMF}}/\Upsilon_*$) require high quality observations (cf. Conroy & van Dokkum 2012). A more practicable approach is to combine measurements of κ and Υ_* with the observed FP and to infer, by subtraction, the missing contribution due to dark matter and IMF trends (e.g. Prugniel & Simien 1997; Graves & Faber 2010); these inferred trends are a useful benchmark for theory.

Single-fibre spectroscopy surveys enabled us to measure the relation between the FP observable σ and stellar population age and metallicity (which, together, determine Υ_*). The strong observed trends (Nelan et al. 2005; Gallazzi et al. 2006; Thomas et al. 2010) must be reflected in the FP, as confirmed by Graves et al. (2009) and Springob et al. (2012). The key role of stellar population properties on the FP is highlighted by the fact that both early-type as well as late-type galaxies lie on the same stellar-mass plane (e.g. Bezanon et al. 2015), and that, for non star-forming galaxies, the evolution of the FP is consistent with the passive evo-

lution of their stellar populations (e.g. van Dokkum & van der Marel 2007; van de Sande et al. 2014).

As for the origin of the FP scatter, a direct view is provided by the study of the FP residuals, defined as the difference between the left- and right-hand side of equation (4). FP residuals correlate with both stellar-population light-weighted age (a proxy for Υ_* , Forbes et al. 1998; Graves et al. 2009; Graves & Faber 2010; Springob et al. 2012) as well as with Sérsic index n (a measure of non-homology κ , Prugniel & Simien 1997). The strength and significance of these correlations can be used to compare the relative importance of stellar-population and structural differences to the FP scatter. These residual trends are also important because if age and n contain information about the FP scatter, it should be possible, in principle, to factor this information into the FP and to improve its precision as a distance indicator (M12). However, a consistent assessment of the relative importance of stellar populations and non-homology requires an unbiased determination of both these observables, as well as the FP residuals.

Non-homology is conveniently captured by Sérsic index n , which is measured from photometry (Bertin et al. 2002). Until recently, however, studies of the FP residuals with stellar-population properties had to rely on single-fibre spectra with relatively low signal-to-noise (Springob et al. 2012) or, alternatively, on stacking observations of different galaxies, which hides the intrinsic galaxy-to-galaxy variability (Graves et al. 2009; Graves & Faber 2010). Moreover, fibres of fixed apparent size, coupled with age and metallicity gradients within galaxies (e.g. Carollo et al. 1993; Mehlert et al. 2003; Sánchez-Blázquez et al. 2007; Zibetti et al. 2020), introduce a size-dependent bias. This ‘aperture bias’ is particularly problematic, because size R_e appears directly in the FP equation (4). Integral-field spectroscopy (IFS) enabled us to measure precise and accurate stellar population properties for individual galaxies. By adding the light inside an aperture that matches the size of each galaxy, we can derive a ‘synthetic’ spectrum with both high signal-to-noise ratio and negligible aperture bias (e.g. McDermid et al. 2015). However, the first generation of IFS surveys (SAURON, de Zeeuw et al. 2002 and ATLAS^{3D}, Cappellari et al. 2011) were limited to ≈ 250 galaxies.

The advent of large IFS surveys has delivered high signal-to-noise spectra for thousands of galaxies, without aperture bias (CALIFA, Sánchez et al. 2012, SAMI, Croom et al. 2012 and MaNGA, Bundy et al. 2015). These surveys helped clarify the link between galaxy structure and stellar population properties (Zibetti et al. 2020). Previous studies have focused on the link between stellar-population properties with either σ (Gallazzi et al. 2006; Ganda et al. 2007; McDermid et al. 2015) or stellar mass (Gallazzi et al. 2005). However, more recently, it became clear that at fixed σ , galaxy size also affects stellar population age. Barone et al. (2018, hereafter: B18) have shown that while the best predictor of light-weighted stellar-population metallicity is gravitational potential (proportional to σ^2), age is driven by surface mass density (proportional to σ^2/R_e). Given that age and metallicity jointly determine Υ_* , the systematic variations of age (and Υ_*) at fixed R_e must also be reflected in the FP tilt, or, alternatively, we need to explain the absence of such effect.

As for the FP residuals, their determination is also

prone to bias, because the FP parameters depend on a number of assumptions: sample selection, photometric band, measurement uncertainties and optimisation method (Jørgensen et al. 1996, Colless et al. 2001, Hyde & Bernardi 2009, M12). For these reasons, understanding the FP requires a careful consideration of the impact of these assumptions on the results.

In this work we leverage the consistent apertures and high signal-to-noise of the integral field SAMI Galaxy Survey and state-of-the-art probabilistic models (i) to conduct a comparative analysis of the FP residuals and (ii) to investigate how stellar population trends affect the tilt and scatter of the FP. In § 2 we present the photometric measurements that have recently been released as part of the SAMI third public data release (Croom et al. 2021) and describe the observables and sample selection criteria used specifically in this work. In § 3 we explain and justify the methods used in the analysis. § 4 illustrates the results: the residuals of the FP correlate most strongly (8σ significance) with stellar population age, whereas structural variables show little or no significant correlation. We connect this trend to the known relation between stellar population age and surface mass density, and show that stellar population relations, on their own, explain most ($\approx 75\%$) of the FP intrinsic scatter. After discussing the implications (§ 5), we conclude with a summary of our findings (§ 6).

Throughout this paper, we use a flat Λ CDM cosmology with $H_0 = 70 \text{ km s}^{-1} \text{ Mpc}^{-1}$ and $\Omega_m = 0.3$. This is the standard cosmology adopted by the SAMI Galaxy Survey (Bryant et al. 2015). Unless otherwise specified, all magnitudes are in the AB system (Oke & Gunn 1983) and stellar masses and mass-to-light ratios assume a Chabrier IMF (Chabrier 2003).

2 DATA AND SAMPLE

The aim of this section is twofold: (i) to describe in detail the photometric measurements of size, shape and flux made available in the third public data release of the SAMI Galaxy Survey and (ii) to describe the additional measurements and the sample selection criteria that are specific to the science goals of this paper. To avoid confusion, we stress that for goal (i) we use the SAMI *parent* sample of $\sim 10,000$ galaxies, whereas for goal (ii) we use the sample from the SAMI Galaxy Survey, i.e. the subset of ~ 3000 galaxies with available integral-field spectroscopy data.

This section is organised as follows. We provide a brief introduction to the SAMI Galaxy Survey (§ 2.1), then proceed to describe the photometric measurements performed on the SAMI parent sample (§ 2.2). Afterwards, we delve into the specifics of this paper: we present spectroscopic measurements based on SAMI observations (§ 2.3) and we estimate the correlation between the measurement uncertainties (§ 2.4). In § 2.5 we briefly introduce additional observables that are necessary to our analysis, but that have already been presented in previous works. The final section explains the selection criteria for the SAMI Fundamental Plane sample (§ 2.6).

2.1 The SAMI Galaxy Survey

Our sample is drawn from the SAMI Galaxy Survey, the integral field spectroscopy survey based on the Sydney-AAO Multi-object Integral field spectroscopy instrument (hereafter, the SAMI instrument; Croom et al. 2012). The SAMI Galaxy Survey (hereafter, simply SAMI) observed a mass-selected sample of ~ 3000 galaxies drawn from a larger parent sample of $\sim 10,000$ galaxies, spanning a wide range in both stellar mass and environment. The parent sample includes galaxies between $10^7 M_{\odot}$ and $10^{12} M_{\odot}$ (the lower mass limit increases with redshift; see Bryant et al. 2015). As for environment, SAMI consists of both field and group galaxies (Bryant et al. 2015) as well as cluster galaxies (Owers et al. 2017). Because of their heterogeneous selection, SAMI galaxies have different photometry. Field and group galaxies are from the Galaxy and Mass Assembly Survey (GAMA; Driver et al. 2011) and use Sloan Digital Sky Survey (SDSS) Data Release 7 optical imaging (Abazajian et al. 2009), reprocessed as described in Hill et al. (2011). Cluster galaxies have been selected from eight clusters; of these, the photometry for Abell 85, Abell 119, Abell 168 and Abell 2399 is from SDSS DR9 (Ahn et al. 2012), whereas photometry for APMCC0917, EDCC442, Abell 3880 and Abell 4038 is from the VLT Survey Telescope’s ATLAS Survey (VST; Shanks et al. 2013, 2015).

In this work, we use data from SAMI internal data release 0.12, consisting of 2153 field and group galaxies and 918 cluster members, for a total of 3071 galaxies. In addition to these galaxies, there are 311 repeat observations; in these cases, we always select the galaxy observed under the best atmospheric seeing. This data has been released to the community as part of SAMI’s public data release 3 (DR3, Croom et al. 2021).

2.2 SAMI photometry

In this section we describe in detail the procedure adopted to measure projected *circularised* half-light radii (R_e) and luminosities, using the Multi Gaussian Expansion algorithm (MGE; Emsellem et al. 1994). We then describe the calibration between different photometric surveys (§ 2.2.3), the estimation of the measurement uncertainties (§ 2.2.4) and the measurement of galaxy surface density (§ 2.2.5). Notice that all the *photometric* measurements are performed on the SAMI *parent* sample, because this larger dataset helps to characterise the quality of our photometric measurements with higher precision.

To facilitate comparison with the literature (e.g. C13, Scott et al. 2015), our Fundamental Plane analysis uses r -band photometry only. Nevertheless, we measure g -, r - and i -band R_e and total magnitudes (m) for each of the 9332 galaxies in the SAMI parent sample. Notice that 436 galaxies in cluster Abell 85 have both SDSS and VST photometry, so the parent sample contains up to 9768 images for each band (some bands have incomplete coverage). For brevity, we discuss in depth only r -band measurements, because the results are analogous and independent between the three bands.

2.2.1 Masking and PSF characterisation

For each galaxy, we retrieve a square cutout 400 arcsec on a side, centred on the galaxy. The size of these cutouts is chosen to guarantee the presence of a number of field stars sufficient to characterise the point-spread function (PSF).

We show two randomly selected FP galaxies in Fig. 1; these are galaxy 383585 from GAMA (using SDSS photometry, panel a) and galaxy 9239900277 from cluster Abell 2399 (again using SDSS photometry, panel b).

First, we use SExtractor (Bertin & Arnouts 1996) to retrieve all the sources in the image. SExtractor also provides a map of all detected sources; after removing the target galaxy, we use this map to create a mask of contaminating sources (masked sources are shaded in yellow in Fig. 1). Notice that interloping sources can be particularly large for cluster galaxies, as shown for galaxy 9403800025 from cluster Abell 4038 (Fig. 2a). Secondly, to characterise the PSF, we retrieve a square cutout around all the stars in the image, defined as sources having a SExtractor keyword CLASS_STAR > 0.9. We model each star as the superposition of 2–5 circular Gaussians, using MGEFIT (the MGE algorithm implemented by Cappellari 2002) and we find the reduced χ^2 for each fit. From this set of stars, we select the best compromise between magnitude, reduced χ^2 and distance from the target galaxy; the model PSF is then the best-fit MGE to the selected star. In Figs 1 and 2, the full-width half-maximum (FWHM) of the PSF is represented by the diameter of the grey circle in the bottom left corner of each panel. Over the whole SAMI parent sample, we find a median PSF FWHM of 1.18 arcsec with a standard deviation of 0.20 arcsec (for SDSS photometry) and of 0.97 arcsec with a standard deviation of 0.19 arcsec (for VST photometry); both these results are in qualitative agreement with the relevant literature (Kelvin et al. 2012; Shanks et al. 2015).

2.2.2 Multi Gaussian Expansion photometry

Once the image mask and model PSF have been determined, we fit the galaxy flux, again using MGEFIT. In order to minimise systematic errors due to substructures (e.g. bars, spiral arms) we use the regularisation feature of MGEFIT (described in Scott et al. 2009); this is the only difference between the photometry we use for the FP analysis and the photometry released as part of the SAMI DR3. The reason why SAMI DR3 uses unregularised fits is that these yield the lowest χ^2 and more realistic galaxy shapes. Regularised fits, on the other hand, while being biased to more circular shapes, can be used to build more robust dynamical models (Scott et al. 2009, their figures 2 and 3). Given the possibility to expand this work to include dynamical models, here we opted for regularised photometry.

Fig. 1 shows two successful fits: observed galaxy isophotes and best-fit model isophotes are traced by black and red solid lines, respectively (isophotes are spaced by $1 \text{ mag arcsec}^{-2}$); the content of the grey square in the left column is reproduced, enlarged, in the right column; the blue dashed circle has radius $1 R_e$. By contrast, Fig. 2 shows two problematic fits. Even though MGE may not describe accurately the substructures common in late-type galaxies (e.g. Fig. 2b), single-Sérsic models do not necessarily per-

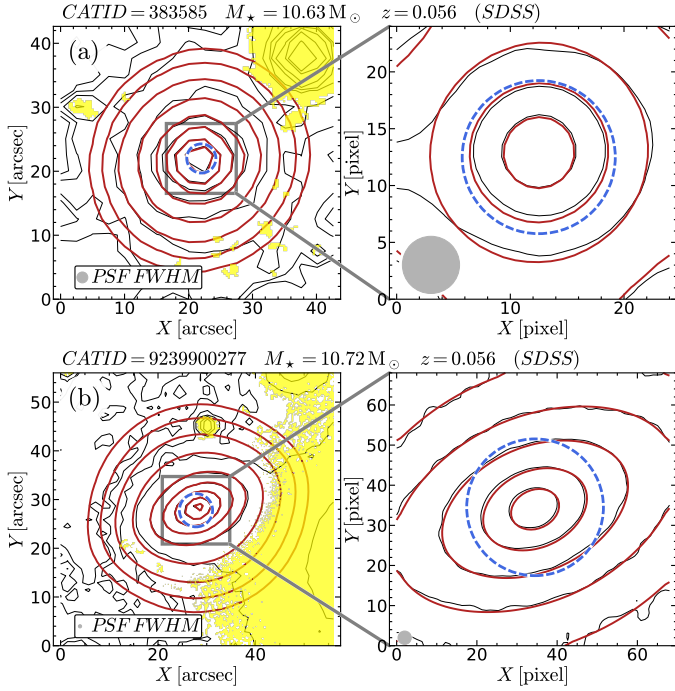


Figure 1. Example of two successful r -band MGE fits: galaxy 383585 from GAMA (with SDSS photometry, panel a) and galaxy 9239900277 from cluster Abell 2399 (again with SDSS photometry, panel b). The left column shows the full extent of the galaxy, the right column shows an enlarged version of the grey square ($4R_e$ on a side). The black/red contours are observed/model isophotes spaced by $1 \text{ mag arcsec}^{-2}$ and the blue dashed circle has radius R_e . Masked regions are highlighted in yellow, the diameter of the grey circle in the bottom-left corner is equal to the PSF FWHM. These two galaxies were randomly selected from the Fundamental Plane sample.

form better, as highlighted by the fact that the two measurements are generally in good agreement (§ 2.2.4).

From the best-fit MGE model we measure total magnitude m , galaxy ellipticity ϵ and galaxy size R_e . Total magnitude is given by the sum of the fluxes of each Gaussian component. The circularised half-light radius R_e is defined as the radius enclosing half the total flux of the circularised MGE model (i.e. the model where all the Gaussian components have the same flux as the best-fit model, but have isotropic dispersion equal to \sqrt{ab} , where a and b are the semi-major and semi-minor axes of the best-fit Gaussian component). Finally, ellipticities are measured with the method of moments as implemented in the algorithm `FIND_GALAXY`¹; we find the model isophote with area $A = \pi R_e^2$, and use its ellipticity as the galaxy ellipticity (C13).

Our magnitude measurements have been k-corrected to redshift $z = 0.05$, close to the median value for the FP sample ($z = 0.053$), using `KCORRECT` (Blanton & Roweis 2007). For galaxies drawn from GAMA, we find good agreement between our k-corrections K (re-computed to $z = 0$ for this test), and previously published values (Loveday et al. 2012); we find $K = (1.048 \pm 0.002)K_{\text{GAMA}} + (0.004 \pm 0.001)$ and

¹ Part of the MGEFIT package available on PyPI.

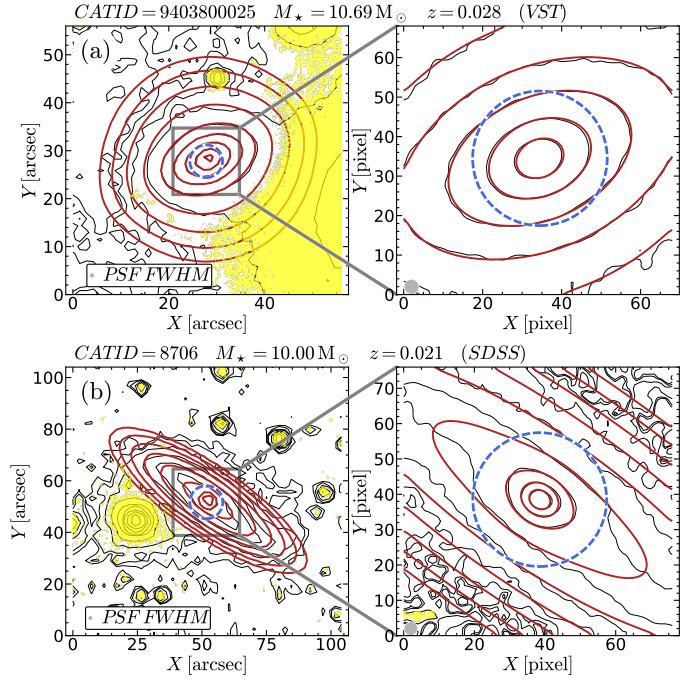


Figure 2. Example of two problematic r -band MGE fits. Galaxy 9403800025 from cluster Abell 4038, using VST photometry (panel a) has substantial contamination from a neighbour (shaded yellow region). Galaxy 8706 is a spiral galaxy from GAMA; the MGE model does not accurately describe its substructure (panel b). Lines and symbols are the same as in Fig. 1.

$rms = 0.014$. Neglecting the k-correction entirely does not change the fiducial parameters or the slope of the FP.

We convert apparent sizes and magnitudes to proper sizes and luminosities using the angular diameter and luminosity distance based on the adopted cosmology (§ 1) and on flow-corrected spectroscopic redshifts (Tonry et al. 2000, Baldry et al. 2012; for cluster galaxies, we use the redshift of the cluster). In order to convert r -band luminosities to units of solar luminosity ($L_{\odot,r}$), we adopt an absolute magnitude of the Sun of $M_{\odot,r} = 4.64 \text{ mag}$ (Blanton & Roweis 2007). The uncertainty on $\log L$ is therefore $\sigma_{\log L} = 0.4\sigma_m = 0.03 \text{ dex}$. For g - and i -band photometry we use $M_{\odot,g} = 5.12 \text{ mag}$ and $M_{\odot,i} = 4.53 \text{ mag}$ respectively (Blanton & Roweis 2007).

2.2.3 Calibration between SDSS and VST photometry

For a considerable fraction of our sample, photometry is available from VST only. In order to remove possible bias due to systematic differences between the VST- and SDSS-based measurements, we use a set of 436 galaxies from cluster Abell 85, for which we have both VST and SDSS data. To compare the two measurements we use the least-trimmed squares algorithm (LTS, Rousseeuw & Driessen 2006), in the free implementation `LTS_LINEFIT` of C13.

We set the data-point uncertainties to a uniform value of 0.045 dex (estimated in § 2.2.4), and the sigma-clipping keyword `CLIP` to a value of 3. The results for R_e and L are illustrated in Fig. 3, where we show the data as black contours enclosing the 50th, 75th and 90th percentiles; the shaded

red region shows the 95% confidence interval, whereas the dashed red lines enclose the 95% prediction interval. For R_e , we find a relation consistent with no systematic trend (i.e. best-fit slope consistent with 1)

$$\log R_{e,\text{SDSS}} = (1.013 \pm 0.013) \log R_{e,\text{VST}} + (0.014 \pm 0.004) \quad (5)$$

but there is a small offset, with SDSS sizes $10^{0.014} \approx 3\%$ larger than VST sizes (the typical uncertainty is 11%; see again § 2.2.4). For luminosity, we find

$$\log L_{\text{SDSS}} = (0.983 \pm 0.004) \log L_{\text{VST}} + (0.201 \pm 0.036) \quad (6)$$

which corresponds to an offset in the magnitude zero-point. This offset is applied on top of the correction already derived by [Owers et al. \(2017\)](#).

We use the two equations (5-6) to convert the VST-based measurements to their SDSS equivalent. Similar corrections are applied to the other photometric variables derived from MGE.

2.2.4 Measurement uncertainties

In order to assess the uncertainties on our measurements of R_e and m , we compare our results to the corresponding values from the GAMA survey, derived from single-Sérsic fits measured using SIGMA ([Kelvin et al. 2012](#)), a pipeline feeding GALFIT ([Peng et al. 2002](#)). We describe only the procedure adopted for R_e , because the procedure for m is analogous.

We cross-match the SAMI parent sample with version 7 of the GAMA Sérsic catalogue, finding 5496 galaxies in common. Of these, 211 have no size measurements in GAMA, 23 have no MGE measurements and 26 have neither (the pipeline did not converge). The effective overlap is therefore 5236 galaxies. To fit the GAMA sizes ($R_{e,\text{GALFIT}}$) as a function of the MGE sizes ($R_{e,\text{MGE}}$) we use the same method adopted to calibrate the VST and SDSS results (§ 2.2.3). We set the data-point uncertainties to a negligible value of 10^{-5} , thereby assuming uniform observational uncertainties². The best-fit relation is

$$\log R_{e,\text{GALFIT}} = (1.011 \pm 0.003) \log R_{e,\text{MGE}} + (0.032 \pm 0.001) \quad (7)$$

with an observed root-mean square $rms = 0.063$. The data is shown in Fig. 4a, where the meaning of the lines is the same as in Fig. 3. We assume that the uncertainties are equal between the GALFIT and MGE measurements, so the adopted uncertainty on $\log R_e$ is equal to $\sigma_{\log R_e} = rms/\sqrt{2} \approx 0.045$ dex. This value is comparable to the uncertainties reported by other authors (e.g. C13). There is a systematic scaling factor between the two measurements, as highlighted by the fact that the best-fit linear coefficient of equation (7) is not unity.

² We find no evidence of a systematic dependence of the R_e uncertainty on either m or R_e itself. We model the distribution of R_e as a bivariate Gaussian, with standard deviation equal to $\sigma(m) = \alpha m + \beta$. The best-fit values of α are always consistent with 0, and entail a maximum difference in the uncertainty σ of 0.004, negligible compared to the average uncertainty of 0.045 dex.

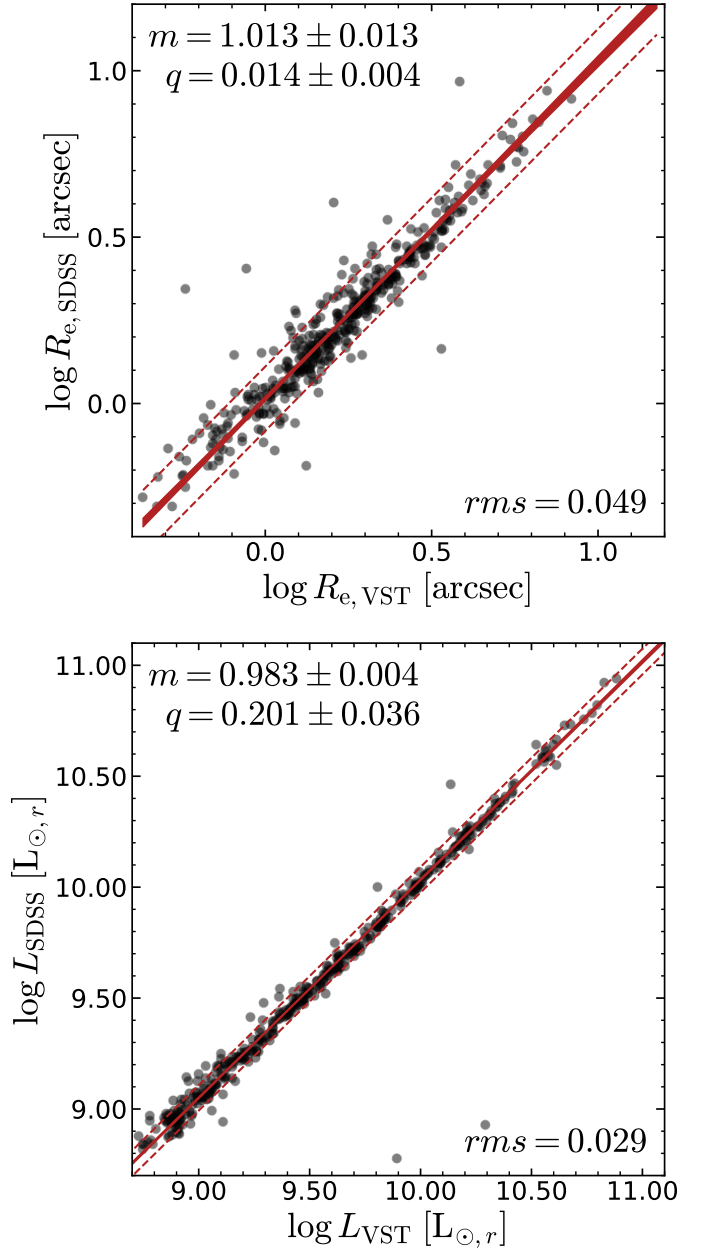


Figure 3. Comparison between SDSS-based and VST-based photometry. We correct the VST measurements to the SDSS standard using the best-fit relation. Circles represent individual SAMI galaxies, the shaded red region shows the 95% confidence interval and the dashed red lines show the 95% prediction interval.

In order to understand the origin of this trend, we explore how the ratio $R_{e,\text{MGE}}/R_{e,\text{GALFIT}}$ correlates with a number of galaxy observables. The first three by statistical significance are stellar mass, projected axis ratio q and Sérsic index n . The most significant correlation is between $R_{e,\text{MGE}}/R_{e,\text{GALFIT}}$ and n (Spearman $\rho = -0.62$; the second most-significant correlation is with q and has $\rho = -0.29$). We can remove the correlation between $R_{e,\text{MGE}}/R_{e,\text{GALFIT}}$ and n with an empirical correction based on the moving median of $R_{e,\text{MGE}}/R_{e,\text{GALFIT}}$ as a function of n . This correction also reduces the scatter about the best-fit relation equation (7) from 0.063 to 0.048 dex, and further removes

the correlations with mass and shape (if we use a correction based on q , the correlation with n is also removed, but the scatter stays constant at 0.063).

Based on these tests, we believe that the most fundamental correlation is with Sérsic index. The systematic trend between the two size measurements is most likely due to the different nature of the MGE and Sérsic fit: the first measures only detected light, whereas the second attempts to extrapolate the total light based on the shape of the detected profile (in practice, in GAMA, the model is integrated only within $R \leq 5 R_e$, Kelvin et al. 2012). For a Sérsic profile, the fraction of light at large radii increases with n , so the decreasing trend of $R_{e,\text{MGE}}/R_{e,\text{GALFIT}}$ is qualitatively consistent with the fact that, with increasing n , MGE misses more light and/or Sérsic models overestimate missing light.

As for the scatter, it does not change between the full overlap sample considered above and the subset of overlapping ETGs from the FP sample (111 galaxies), suggesting that the systematic difference between GAMA and SAMI photometry is not due to the inclusion of late-type galaxies (LTG) in the comparison sample. Moreover, we find the same results between the full overlap sample and the subset with $R_e > 1.5$ arcsec (1111 galaxies), suggesting the systematic slope is not caused by PSF modelling. This hypothesis is confirmed by repeating the MGE measurements using the same PSF reconstruction method as GAMA (using the software PSFEX, Bertin 2011).

For magnitudes, we use the same procedure and find

$$m_{\text{GALFIT}} = (1.014 \pm 0.001)m_{\text{MGE}} - (0.304 \pm 0.021) \quad (8)$$

with an observed root-mean square scatter $rms = 0.108$ (Fig. 4b). The uncertainty on m is therefore $\sigma_m \approx 0.076$.

In summary, this comparison shows that circularised effective radii are consistent between our MGE measurements and the values published in GAMA, but there is a systematic factor such that $R_{e,\text{GALFIT}}$ is 5–7% larger than $R_{e,\text{MGE}}$ (the interval of the rescaling factor is the 16th–84th percentile of the distribution of $R_{e,\text{MGE}}$ for the FP sample, defined in § 2.6). Magnitudes, on the other hand, are consistent within 0.08 mag; the zero-point $b = -0.304 \pm 0.021$ of the best-fit relation in equation (8) does not imply an equally large offset in magnitude zero-point, because the best-fit slope is larger than unity. Over the magnitude range of the FP sample, m_{GALFIT} is 0.09–0.06 mag brighter than m_{MGE} . For magnitudes, if we swap the measurements from Kelvin et al. (2012) with the SDSS ‘model’ values from SDSS Data Release 14 (Abolfathi et al. 2018) or with the GAMA photometry from LAMBDA (Wright et al. 2016), we find comparable (but better) agreement with our MGE measurements.

As a final remark, the adopted value of the sigma-clipping threshold in LTS.LINEFIT (parameter CLIP) does affect the derived uncertainties. For example, by using a value of 4 the resulting uncertainties on R_e are 30% larger. We tested the effect of adopting 50% smaller or larger uncertainties on our FP fit, and, although the best-fit FP parameters depend on the value of the uncertainty, the key results of this work are qualitatively unchanged (see § 4.1.5 and Table 3, rows 11–15).

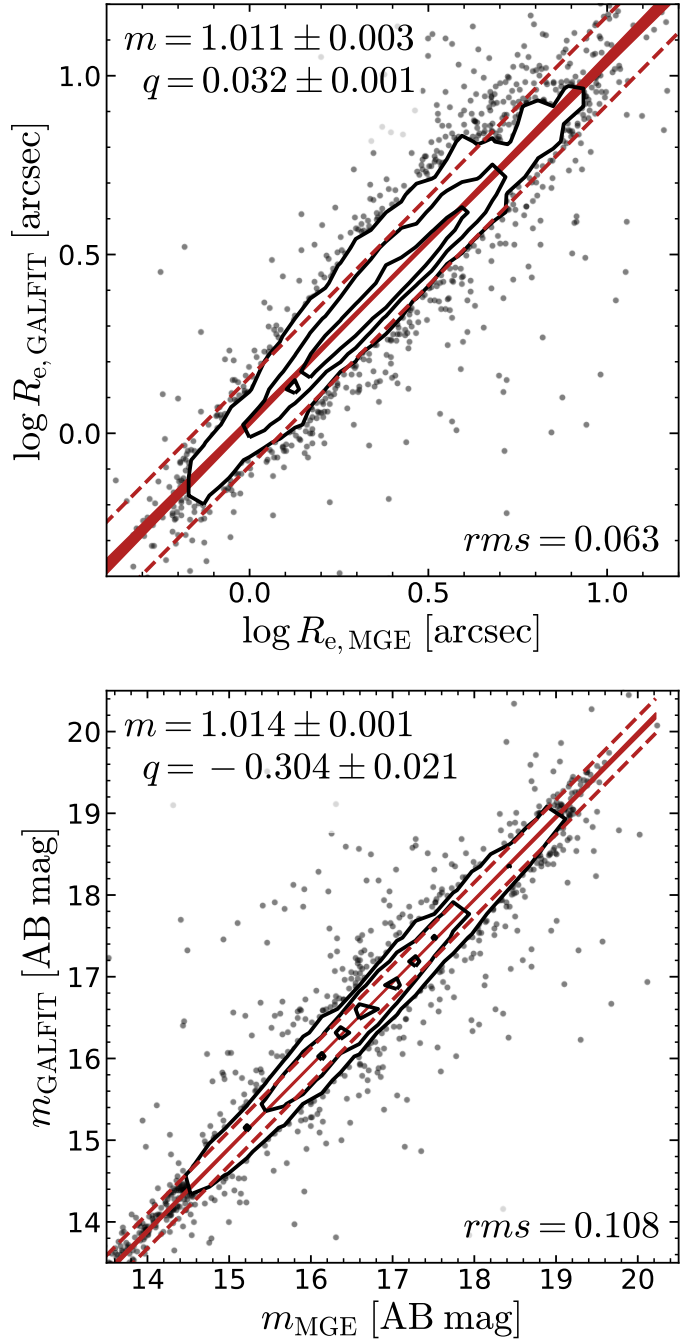


Figure 4. Comparison between our MGE measurements and the corresponding values from the GAMA survey, for both effective radius R_e (panel a) and apparent magnitude m (panel b). The solid black contour lines enclose the 90th, 75th and 50th percentiles of the data, the shaded red region shows the 95% confidence interval, and the dashed red lines show the 95% prediction interval. We estimate the observational uncertainties on both R_e and m using the observed root-mean square scatter about the best-fit relation (reported in the bottom right corner of each panel). The values m , q and x_0 are the best-fit slope and zero-point of the linear relation (equations (7) and (8)).

2.2.5 Surface mass density

We estimate the surface mass density in two elliptical apertures: an aperture of fixed physical size, having circularised radius 1 kpc, and a galaxy-dependent aperture having circularised radius $1 R_e$; in practice, the apertures we use are the model isophotes with area closest to πkpc^2 and πR_e^2 , respectively. We measure g - and i -band magnitudes inside these apertures, then estimate the enclosed stellar masses from absolute i -band magnitude and $g - i$ colour (Taylor et al. 2011). In practice, we implement the k-correction by defining

$$\begin{aligned} \log M_*(< R) / M_\odot \equiv & -0.4 M_i(< R) - \log(1 + z) \\ & + (1.2117 - 0.5893z) \\ & + (0.7106 - 0.1467z)(g - i)(< R) \end{aligned} \quad (9)$$

where $M_i(< R)$ is the enclosed absolute magnitude prior to the k-correction (Bryant et al. 2015). We then define

$$\begin{aligned} \Sigma_*(R < 1 \text{kpc}) & \equiv M_*(R < 1 \text{kpc}) / (\pi 1 \text{kpc}^2) \\ \Sigma_*(R < R_e) & \equiv M_*(R < R_e) / (\pi R_e^2) \end{aligned} \quad (10)$$

2.3 SAMI spectroscopy

The main SAMI data consists of integral field spectra taken with the SAMI instrument at the prime focus of the 3.9 m Anglo-Australian Telescope. The SAMI instrument uses 13 integral field units (IFUs), deployable anywhere within a 1 degree diameter field of view. Each IFU is a fused fibre bundle (hexabundle; Bland-Hawthorn et al. 2011; Bryant et al. 2014), containing 61 fibres of 1.6 arcsec diameter, for a total IFU diameter of 15 arcsec; the distinctive advantage of the SAMI instrument is that the hexabundles have a higher fill factor than conventional fibre bundles (0.75 instead of ~ 0.5 , Croom et al. 2012).

The IFUs, as well as 26 single fibres used for sky measurements, are plugged into pre-drilled plates using magnetic connectors. The fibres are fed to the double-beam AAOmega spectrograph, which allows a range of different resolutions and wavelength ranges (Sharp et al. 2006). For SAMI we use the 570V grating at 3750–5750 Å (blue arm) and the R1000 grating at 6300–7400 Å (red arm). The spectral resolutions for the blue and red arms are respectively $R=1812$ ($\sigma = 70.3 \text{ km s}^{-1}$) and $R=4263$ ($\sigma = 29.9 \text{ km s}^{-1}$); the reference wavelengths are $\lambda_{\text{blue}} = 4800 \text{ Å}$ and $\lambda_{\text{red}} = 6850 \text{ Å}$ (van de Sande et al. 2017b, their Table 1). Each galaxy was exposed for approximately 3.5 hours, following a hexagonal dither pattern of seven equal-length integrations (Sharp et al. 2015). The median full-width-at-half-maximum seeing was 2.06 ± 0.40 arcsec. The basic data reduction process is described in Sharp et al. (2015) and Allen et al. (2015); the data quality is illustrated in the public data release papers, alongside a number of improvements in the data reduction (Green et al. 2018; Scott et al. 2018; Croom et al. 2021).

2.3.1 Spectroscopic measurements

For each galaxy, we constructed a synthetic elliptical aperture of equivalent radius $1 R_e$, i.e. the r -band elliptical isophote with area $A = \pi R_e^2$ (see § 2.2.2). This aperture size, like all adaptive apertures, is problematic for both large

galaxies (where the aperture is larger than the IFU) and small galaxies (where the aperture is smaller than the SAMI PSF); we discuss this issue in relation to the sample selection (§ 2.6) as well as in relation to the FP determination (§ 4.1.1). We derive the aperture spectra as a weighted sum of the IFU spectra, where the spectrum in each spatial pixel (spaxel) is weighted by the fraction of its area falling inside the ellipse. In order to mimic as closely as possible the behaviour of an elliptical aperture, we do not use statistical weights in the sum; because the SAMI spectra are flux calibrated (Green et al. 2018); applying, e.g., inverse-variance weighting would create spectra that are more weighted towards the central spaxels than in a large, physical aperture. Three example apertures are illustrated by the white dashed ellipses in the right column of Fig. 5. Because SAMI has different spectral resolutions in the blue and red arm, we convolve the red spectrum to the same spectral resolution as the blue spectrum (as described in van de Sande et al. 2017b). The resulting spectrum covers the full spectral range of SAMI, with a $\sim 5500 \text{ Å}$ gap between 5750 Å and 6300 Å.

We used these spectra to measure aperture kinematics. We obtained the second moment of the velocity distribution (σ_e) using the penalised pixel fitting algorithm PPXF (Cappellari & Emsellem 2004; Cappellari 2017) and the MILES stellar template library (Sánchez-Blázquez et al. 2006; Falcón-Barroso et al. 2011). The process is identical to that used to measure the kinematics in each spaxel (van de Sande et al. 2017b) and to measure the DR3 aperture kinematics (Croom et al. 2021). In brief, we fit a Gaussian line-of-sight velocity distribution as well as an additive 12th order Legendre polynomial. The fit is iterated three times. In the first iteration, we estimate (if necessary) a scaling for the noise spectrum. In the second iteration we reject bad pixels using an iterative sigma-clipping algorithm, (the CLEAN keyword in PPXF). The third iteration yields the measurement of σ_e . We estimate the uncertainties using a Monte Carlo approach: we create an ensemble of σ_e measurements from one hundred random-noise realisations of the best-fit spectrum, and define the uncertainty to be the standard deviation of the ensemble. The random noise was obtained by shuffling the noise in 15 equal-width spectral intervals. We show three example fits in Fig. 5: these galaxies were chosen to have σ_e closest to the 5th, 50th and 95th percentiles of the σ_e distribution for our final sample (§ 2.6). Compared to DR3 aperture kinematics, the values used in this work present two differences: first, our apertures use regularised MGE fits (whereas DR3 uses unregularised fits). Second, our apertures are elliptical, whereas DR3 apertures are circular. Nevertheless, we find excellent agreement between the two measurements

$$\log \sigma_{\text{DR3}} = (0.975 \pm 0.003) \log \sigma_e + (0.054 \pm 0.007) \quad (11)$$

with a scatter of 0.04 dex. Although σ_e is systematically larger than σ_{DR3} , the difference is small (1% at $\sigma_e = 200 \text{ km s}^{-1}$) and can be intuitively explained as follows. Compared to the circular aperture of the same area, an elliptical aperture along the galaxy major axis includes more spaxels along the major axis and fewer spaxels along the minor axis. Most ($\sim 85\%$) ETGs are ‘fast rotators’ (Krajnović et al. 2011; Emsellem et al. 2011), i.e. galaxies with considerable rotation support (the exact definition of fast rotator varies, but they are identified as galaxies that are intrinsic

sically flat $\epsilon > 0.4$ and/or having $(V/\sigma)_e \gtrsim 0.1$; Emsellem et al. 2011; Cappellari 2016; van de Sande et al. 2017a, 2020) Therefore, for most galaxies in our ETG sample, major-axis spaxels have larger line-of-sight velocity offsets than minor-axis spaxels, and contribute more to the aperture dispersion. Measurement uncertainties are estimated by comparing repeat observations. We use a uniform value of 0.022 dex for all galaxies.

The stellar-population parameters age, $[Z/H]$ and $[\alpha/Fe]$ were determined as part of the SAMI survey. Scott et al. (2017) measured a set of twenty Lick absorption indices (Worthey et al. 1994; Trager et al. 1998) and used simple-stellar-population (SSP) models to convert the empirical index values to luminosity-weighted SSP-equivalent stellar-population parameters (Schiavon 2007; Thomas et al. 2010); here $[Z/H]$ is the (logarithmic) metal-to-hydrogen mass fraction relative to the solar value

$$[Z/H] \equiv \log Z/X - \log(Z/X)_\odot \quad (12)$$

where Z and X are the metal and hydrogen mass fractions, respectively. For an in-depth discussion of the SAMI stellar-population parameters, see Scott et al. (2017). Here we stress that for any given galaxy, each SSP parameter captures only one aspect (the light-weighted mean) of what is in fact a distribution of stellar population properties. We then infer r -band stellar mass-to-light ratios from the best-fit age and metallicity measurements, interpolating on the models of Maraston (2005) and using the same grid as Scott et al. (2017). Our mass-to-light ratios (Υ_*) assume a Chabrier IMF (Chabrier 2003), whereas the models of Maraston (2005) assume a Kroupa IMF (Kroupa 2001). We therefore divided the Kroupa mass-to-light ratios by a factor of 1.12 to obtain Υ_* (Speagle et al. 2014).

2.4 Correlated noise

Apart from the measurement uncertainties on $\log \sigma_e$, $\log R_e$ and $\log L$, the covariance matrix also contains three off-diagonal elements. The largest of these (by absolute value) is the covariance between the measurement uncertainties on $\log L$ and $\log R_e$. We estimate this entry by comparing the SDSS luminosity and size measurements to the corresponding VST measurements, in all the three bands. In order to obtain the measurement errors, as well as to remove the physical correlation between size and luminosity (Pearson correlation coefficient $\rho \approx 0.6$), we subtract from each set of size and luminosity measurements, the median over all six measurements (three bands for SDSS photometry and three bands for VST photometry). Furthermore, to eliminate the effect of systematic changes between the three bands, we subtract the median from each set of measurements in any given photometry and band. After rejecting outliers (defined as lying outside the contour enclosing the 95th percentile of the data) we find that the correlation coefficient is $\rho = 0.235$ (the covariance is 2.8×10^{-4}). Using a stricter rejection threshold yields even lower correlation ($\rho = 0.202$ if we reject data outside the 80th percentile). If we repeat the test to measure the correlation between effective radius and the average surface brightness within R_e , we find $\rho = -0.770$, a number considerably smaller (in absolute value) than reported in the literature ($\rho = -0.95$; M12). It is reasonable to assume that the difference is due to the flexibility of MGE

photometry compared to the rigid functional form of Sérsic photometry. As a validation test, we repeat the MGE fits after rotating all galaxy images in steps of 5 degrees, thus building a set of size and luminosity measurements for each galaxy. With this method, we derive a correlation coefficient $\rho = 0.650$. Although this is much larger than our measured value of $\rho = 0.235$, these measurements are not independent and so a larger correlation coefficient is expected.

The second largest entry in the covariance matrix is the covariance between the measurement uncertainties on $\log \sigma_e$ and $\log R_e$. This correlation arises because we use R_e to create the aperture spectra (from which we measure σ_e) and because the second moment of the velocity distribution depends on the radius of the aperture inside which it is measured (Jørgensen et al. 1996). We estimate this covariance as $\alpha \sigma_{\log R_e}^2 = -0.00015$ (following Cappellari et al. 2006, we assumed $\sigma_e \propto R_e^{-0.066}$). Finally, we neglected the last component of the covariance matrix and assumed that measurement uncertainties in $\log \sigma_e$ and $\log L$ are uncorrelated.

2.5 Ancillary data

For each galaxy, we use g -, r - and i -band photometry, derived either from SDSS (if available) or from VST (for the clusters APMCC0917, EDCC442, Abell 3880 and Abell 4038; Owers et al. 2017).

Magnitudes in the i -band and $g-i$ colours were measured consistently across SAMI (Owers et al. 2017). Apparent magnitudes were converted to absolute magnitudes M_i using the luminosity distance in the adopted cosmology. The input redshifts for the luminosity distance are individual spectroscopic redshifts from GAMA for the field and group galaxies (Bryant et al. 2015) or cluster redshifts for the cluster galaxies (Owers et al. 2017).

We use photometric stellar masses (M_*) from the SAMI catalogue (Bryant et al. 2015; Owers et al. 2017). These masses (and mass densities) were derived by combining absolute i -band magnitude and $g-i$ colour (Taylor et al. 2011; § 2.2.5).

When available, we use r -band Sérsic indices n (from Kelvin et al. 2012 or Owers et al. 2019 for GAMA and cluster galaxies, respectively). To estimate the uncertainties on n , we compare r - and i -band indices for ETG galaxies, finding a scatter of 0.03 dex or 6% (after dividing by $\sqrt{2}$). This value is a compromise between low- to intermediate-index galaxies, where the scatter is smaller, and large-index galaxies ($n \gtrsim 5$), where it is larger.

Optical morphologies were assigned by twelve SAMI team members, using RGB cutouts and following the classification scheme adopted by GAMA (Kelvin et al. 2014). Firstly, galaxies are divided into late- and early-types by the presence or absence of spiral arms. Late-types are subdivided into early- and late-spirals by the presence or absence of a bulge, whereas early-types are subdivided into lenticulars and ellipticals by the presence or absence of a stellar disc. Whenever the image quality was deemed insufficient, or no consensus ($> 67\%$) was reached between the classifications, galaxies were classified as uncertain. The SAMI morphological classification was presented in Cortese et al. (2016): ellipticals have mtype=0, lenticulars (S0) have mtype=1 and intermediate types have mtype=0.5. In this paper, we define early-type galaxies (ETGs) as hav-

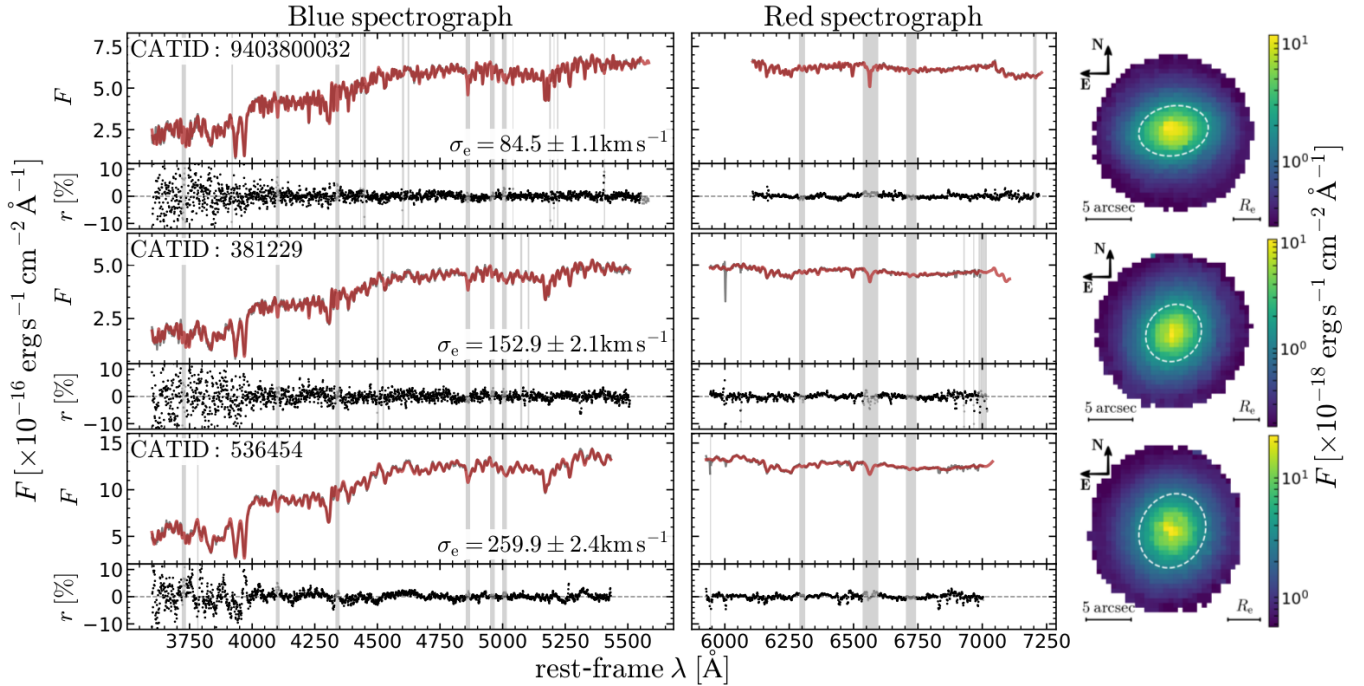


Figure 5. Three example pPXF fits. From top to bottom, the three galaxies have σ_e closest to the 5th, 50th and 95th percentiles of the σ_e distribution. The grey lines show the SAMI blue-arm (left column) and red-arm spectra (central column); the red lines are the best-fit spectra. These aperture spectra are unweighted sums of the flux inside the MGE model isophote of area πR_e^2 (right column). Gray vertical regions in spectra were not fit, either because they may contain possible (weak) emission lines or because they were sigma-clipped. Below each fit, we show the relative residuals. The right column shows the SAMI view of the three galaxies, with superimposed the elliptical aperture of area πR_e^2 .

ing $m_{\text{type}} \leq 1$; this conservative definition ensures minimal contamination from late-type galaxies (LTGs), even though adding galaxies with $m_{\text{type}}=1.5$ does not change our results.

In addition, we use $(V/\sigma)_e$ ratios measured on the SAMI kinematic maps. These values have been corrected to an aperture of $1 R_e$ using a statistical correction based on galaxies with sufficient radial coverage (van de Sande et al. 2017a). Numerical simulations have shown that $(V/\sigma)_e$ is in good agreement with more sophisticated measures of the relative importance of streaming and random motions (e.g. Thob et al. 2019).

2.6 Sample selection

We use a volume-limited subset of the SAMI sample consisting of 1461 galaxies with $M_* \geq 10^{10} M_\odot$ and $z \leq 0.065$ (cf. Bryant et al. 2015, their Fig. 4; for cluster members we used the redshift of the cluster instead of the redshifts of individual galaxies; the mass cut effectively removes only three galaxies, which do not affect our analysis). From this initial selection, 1460 have optical morphologies, and we further select 642 ETGs by requiring $0 \leq m_{\text{type}} \leq 1$ (we prioritised sample purity over sample size, see § 2.5). Note that if we limited the selection to elliptical galaxies only ($m_{\text{type}} = 0$) the results presented here would be qualitatively unchanged, but the smaller sample size (216 galaxies) means that the significance of some results would be lower (top right histogram in Fig. 6). We further introduce censoring in $\log L$ by requiring $L \geq 10^{9.7} L_{\odot,r}$; this cut removes the asymmetric tail of 26 low-luminosity galaxies in Fig. 6 and allows

an accurate yet relatively simple probabilistic model. From this sample of 616 galaxies, we further remove 24 galaxies that are too large relative to the SAMI IFU and so have no measurement of σ_e . Even though removing these 24 galaxies introduces a bias against large galaxies, their inclusion does not affect the results of the subsequent analysis (§ 4.1.1). After visual inspection of the aperture spectra, we also remove 31 galaxies with Balmer emission lines, thus bringing the sample down to 561 galaxies.

In general an accurate determination of the FP requires removing low-quality measurements, e.g. galaxies with large measurement uncertainties in σ_e or with σ_e below the instrument spectral resolution. However, this additional quality selection is not necessary, because the mass and redshift cuts already remove low-quality data. Comparing the Sérsic and MGE photometry, we find just 14 galaxies that have measurement discrepancies larger than three standard deviations. We chose not to remove these galaxies either, but use instead the robust fitting algorithm to identify the most likely outliers. In fact, even though some of these 14 galaxies have neighbours that could have affected the photometry, others appear regular galaxies where either the Sérsic or MGE fit performed poorly. Moreover, that approach does not reject unreliable measurements where systematic errors bias both the Sérsic and MGE fits in the same direction; we manually remove 9016800416, as it is too close to the edge of the image frame to measure R_e , even though there is good agreement between the two fitting methods.

We are left with a final sample of 560 ETGs. Within the mass and volume limits of our selection, this sample has the

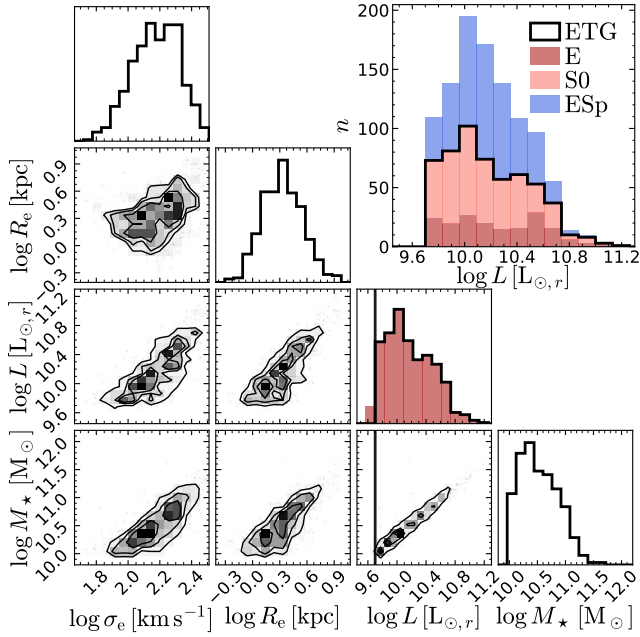


Figure 6. The properties of our volume- and mass-limited ETG sample. Notice the non-Gaussian nature of the $\log L$ distribution (filled red histogram); the cut in $\log L$ (solid black vertical line) enables us to remove the tail of $L < 10^{9.7} L_{\odot,r}$ galaxies and to use a simpler probability model for the FP (§ 3.1); alternative optimisation methods also assume (implicitly) some distribution. The top-right histogram shows the relative contribution of ellipticals (E; red) and lenticulars (S0; salmon) to our sample of ETGs (solid line). Blue bars show the luminosity distribution of early spirals (ESp; notice the bars are stacked).

same completeness as the original SAMI ETG sample. The FP sample is not representative of the SAMI survey volume, however, because cluster galaxies are over-represented (van de Sande et al. 2020).

3 DATA ANALYSIS

The value of the best-fit FP parameters depends on the model adopted to describe the data. For this reason, the model choice is of central importance in comparing and interpreting the results. In this section we describe the FP model adopted throughout this paper (§ 3.1) and motivate our choice using a comparison to an alternative optimisation approach popular in the literature (§ 3.2 and § 3.3). We finally illustrate the expected residual correlations for our model (§ 3.4).

3.1 3dG: a 3-d Gaussian algorithm

We adopt a Bayesian approach, and model the FP as a three-dimensional (3-d) Gaussian with a cut in $\log L$ (censoring). This choice is motivated by a visual inspection of the distribution of the SAMI observables (histograms of $\log \sigma_e$, $\log R_e$ and $\log L$ in Fig. 6), as well as from previous experience fitting the 6dFGS FP (M12). Even though the assumption of a Gaussian distribution might appear crude, it is far more accurate than the assumption of a uniform distribution that implicitly underlies algorithms minimising the distance to

the plane. Censoring (equation 18 below) is introduced to account for truncation of the distribution in $\log L$, which is a consequence of our sample selection criteria (see the vertical line in Fig. 6).

The most general 3-d Gaussian has nine parameters: three for the centroid and six for the symmetric covariance matrix. Another parameter is needed to implement censoring, so the model has ten parameters in total.

In order to preserve a straightforward geometric interpretation, we factorise the generic covariance matrix into a diagonal and an orthogonal factor: the former (Σ) represents the uncorrelated covariance of the FP in the eigenvector basis, while the latter (R) represents the rotation transforming the observable basis to the eigenvector basis.

To write down this model in a concise manner, we first introduce some definitions: $\mathbf{x} \equiv (\log \sigma_e, \log R_e, \log L)$ are the coordinates in the observable space whereas \mathbf{v} are the coordinates in the reference frame of the 3-d Gaussian. The most generic multivariate Gaussian is given by

$$\mathcal{N}_{\mathbf{m},\mathbf{A}}(\mathbf{x}) \equiv \frac{1}{\sqrt{\det(2\pi\mathbf{A})}} \exp\left\{-\frac{1}{2}(\mathbf{x} - \mathbf{m})^T \mathbf{A}^{-1}(\mathbf{x} - \mathbf{m})\right\} \quad (13)$$

where \mathbf{A} is the covariance matrix and \mathbf{m} is the centroid. In the reference frame of \mathbf{v} , the model probability is given by

$$p(\mathbf{v}) = \mathcal{N}_{\mathbf{0},\Sigma}(\mathbf{v}) \quad (14)$$

where Σ is the diagonal correlation matrix. We further assume that the \mathbf{v} coordinates are sorted according to the scatter of the 3-d Gaussian (from largest to smallest) and that the \mathbf{v} reference frame has the same chirality as the \mathbf{x} reference frame. With these assumptions, there exists a rotation R by an angle θ about an axis $\hat{\mathbf{u}}$, such that $\mathbf{v} = R(\mathbf{x})$. In the base of \mathbf{x} , R can be represented by an orthogonal matrix \mathbf{R} , such that $\forall \mathbf{x}, R(\mathbf{x}) = \mathbf{R}\mathbf{x}$. If we call the mean of the observables $\boldsymbol{\mu}$, we can write the probability in the \mathbf{x} reference frame as

$$p(\mathbf{x}|\text{model}) = \mathcal{N}_{\boldsymbol{\mu},\mathbf{R}^T\Sigma\mathbf{R}}(\mathbf{x}) \quad (15)$$

which expresses the probability of the observables given the model. So far, the model has nine free parameters: three Gaussian centroids ($\boldsymbol{\mu}$), three standard deviations (the diagonal matrix Σ) and three parameters to identify the rotation R . It is useful to recall that, because \mathbf{R} is orthogonal, the inverse of the covariance matrix $\mathbf{R}^T\Sigma\mathbf{R}$ is equal to $\mathbf{R}^T\Sigma^{-1}\mathbf{R}$ and $\det(2\pi\mathbf{R}^T\Sigma\mathbf{R})$ is equal to $\det(2\pi\Sigma)$.

We then assume Gaussian noise for each of the N measurements \mathbf{x}_i , with covariance matrix \mathbf{E}_i , so that given a true value of \mathbf{x} , a measurement \mathbf{x}_i has probability

$$p(\mathbf{x}_i|\mathbf{x}) = \mathcal{N}_{\mathbf{x},\mathbf{E}_i}(\mathbf{x}_i) \quad (16)$$

and the probability of \mathbf{x}_i given the model is given by the definite integral

$$p(\mathbf{x}_i|\text{model}) = \iiint d\mathbf{x} p(\mathbf{x}_i|\mathbf{x}) p(\mathbf{x}|\text{model}) = \mathcal{N}_{\boldsymbol{\mu},\mathbf{R}^T\Sigma\mathbf{R}+\mathbf{E}_i}(\mathbf{x}_i) \quad (17)$$

where we have integrated the convolution of two Gaussians by completing the squares. We introduce a cut in $\log L$, so

that the new probability $p(\mathbf{x}_i|\text{model})$ is given by

$$p(\mathbf{x}_i|\text{model}) = \begin{cases} f_i(L_{\min})\mathcal{N}_{\boldsymbol{\mu}, \mathbf{R}^T \boldsymbol{\Sigma} \mathbf{R} + \mathbf{E}_i}(\mathbf{x}_i), & \text{if } L \geq L_{\min} \\ 0, & \text{otherwise} \end{cases} \quad (18)$$

where for each i , $f_i(L_{\min})$ is a constant such that

$$\int_{-\infty}^{\infty} dx_1 \int_{-\infty}^{\infty} dx_2 \int_{\log L_{\min}}^{\infty} dx_3 f_i(L_{\min}) \mathcal{N}_{\boldsymbol{\mu}, \mathbf{R}^T \boldsymbol{\Sigma} \mathbf{R} + \mathbf{E}_i}(\mathbf{x}) = 1 \quad (19)$$

An expression for $f_i(L_{\min})$ is given in Appendix A.

Using Bayes' theorem, the probability of the model given all the data is then

$$p(\text{model}|\text{data}) = \frac{\prod_{i=1}^N p(\mathbf{x}_i|\text{model})p(\text{model})}{p(\text{data})} \quad (20)$$

where $p(\text{model})$ is the prior. Unfortunately, integrating this expression is complicated by the cut in $\log L$, so that, even assuming conjugated priors, the evidence would *not* be Gaussian-inverse-Wishart (e.g. DeGroot 1970). For this reason, we assume flat, uninformative priors for all the parameters and, to determine their value, we integrate equation (20) with EMCEE (Foreman-Mackey et al. 2013), an implementation of the Markov Chain Monte Carlo algorithm (MCMC, Metropolis et al. 1953) proposed by (Goodman & Weare 2010). The implementation of the 3-d Gaussian model (3dG) is a generalisation of the algorithm already presented in B18 and Barone et al. (2020), with the addition of censoring in $\log L$. To verify that the method is correct, we also use a nested sampler and find the same results as with the MCMC integrator (we used the python package DYNesty, Skilling 2004, 2006; Feroz et al. 2009; Higson et al. 2019; Speagle 2020).

3.2 Model bias

In order to assess our model, we use the well-established LTS_PLANEFIT algorithm as a comparison. LTS_PLANEFIT (C13), is a 3-d extension of the LTS_LINEFIT algorithm which we have briefly introduced in § 2.2.4. The core of LTS_PLANEFIT is a least-squares minimisation, where the quantity being minimised is the sum of the squares of the distance of each data point to the plane. The distance is calculated along the z axis (C13, equation 7 and Press et al. 2007, section 15.3). Because the quantity minimised by these methods is directly related to the observed rms , the best-fit LTS_PLANEFIT models have, by construction, lower rms compared to the best-fit 3dG models. Notice, however, that lower rms is *not* necessarily an indication of a more likely model: as we will see (§ 3.4, Table 1 and Fig. 7), depending on the underlying model, the price for this lower rms may be a bias on the value of the inferred model parameters. The probability distribution underlying direct-fit methods like LTS_PLANEFIT assumes an infinite plane with Gaussian scatter along the z axis

$$p(x, y, z) \propto \frac{1}{\sqrt{2\pi\sigma_{\text{int}}^2}} \exp\left\{-\frac{(z - ax - by - c)^2}{2\sigma_{\text{int}}^2}\right\} \quad (21)$$

where, in order for the probability to be integrable, some truncation is required in both x and y . The limits of this truncation determine the missing multiplicative factor. In

equation (21) the probability distribution of the independent variables is not constrained. Formally, this model can be thought of as the limit for an infinitely extended plane (see Appendix B and Kelly 2007), which clearly does not apply to our sample. In fact, by inspecting Fig. 6, we can see that the range of the FP observables is larger, but not much larger, than the FP thickness (the narrowest histogram has a FWHM of 0.36 dex, roughly four times larger than the typical FP scatter of ≈ 0.05 –0.1 dex). This is a critical aspect of our model choice. In fact, for an infinitely extended underlying distribution, the direction of scatter does not matter, as the normal and axial scatters are just projections of each other. However, because our data is not infinitely extended and uniform (Fig. 6), then the varying underlying distribution combined with the direction of the scatter modifies the observed distribution (e.g. consider the ends of a *finite* uniform distribution with normal and axial scatter, as in panels c and d of Fig. 7). In the realm of finite distributions, we find that the precise shape of the 1-d distribution of the observables does not appear to bias the FP coefficients (as long as the distribution stays symmetric, Fig. 7a-c). What matters most for these finite distributions is the direction of the intrinsic scatter, whether it is orthogonal to the FP (as assumed by our algorithm) or along the z axis (as assumed by direct-fit methods). To quantify the effect of model mismatch, we conduct two sets of tests. In the first set, we test the 3dG and LTS_PLANEFIT algorithms on a mock dataset based on the 3-d Gaussian generative model. For the second set, we use mock datasets based on a probability distribution close to the generative model of LTS_PLANEFIT.

For the first set of tests, we create a range of mock datasets based on the fiducial SAMI FP (§ 4) and attempt to recover the input FP parameters with LTS_PLANEFIT and with 3dG. For a 3-d Gaussian generative model, we generate one hundred mock samples from the multivariate Gaussian with covariance matrix

$$\mathbf{R}^T \boldsymbol{\Sigma} \mathbf{R} + \mathbf{E} = \begin{bmatrix} 0.0316 & 0.0263 & 0.0614 \\ 0.0263 & 0.0704 & 0.0946 \\ 0.0614 & 0.0946 & 0.1686 \end{bmatrix} \quad (22)$$

obtained from the fiducial FP (§ 4.1, this matrix includes both the intrinsic covariance matrix and homoscedastic measurement uncertainties). Each mock consists of 560 triplets ($\log \sigma_e, \log R_e, \log L$), where the number 560 is chosen to match the size of the FP sample (see § 2.6). We run the fit one hundred times, and determine the bias on each model parameter as the mean of the inferred values; the significance is given by the uncertainty on the mean. For the LTS_PLANEFIT algorithm, the bias is -8% , $+5\%$ and $+3\%$ in a , b and c (all offsets are statistically significant). If we introduce censoring in $\log L$, the bias is -12% , -2% and $+5\%$, consistent with the findings of M12. In contrast, the same tests show that the 3dG algorithm recovers a , b and c without measurable bias. For the 3-d Gaussian generative model, the bias in a , b and c is $+0.5\%$, $+0.02\%$ and -0.2% , respectively; for the censored 3-d Gaussian, the bias is -0.06% , $+0.1\%$ and $+0.1\%$. None of these values are statistically significant.

For the second set of tests, we aim to assess the bias of the 3dG algorithm when fitting mock data drawn from the model underlying direct-fit methods. However, because this probability distribution is not integrable (equation 21), and

because SAMI data is not uniformly distributed in $\log \sigma_e$ and $\log R_e$, we adopt the following approach. First, we take the median and standard deviation of the measured $\log \sigma_e$ and $\log R_e$; we correct the standard deviations for observational uncertainties by subtracting in quadrature the median measurement uncertainty in $\log \sigma_e$ and $\log R_e$. We then sample 560 values of $\log \sigma_e$ and $\log R_e$ from the Gaussian distributions with mean equal to the observed mean and standard deviation equal to the corrected standard deviation. $\log L$ is obtained drawing randomly from the Gaussian distribution with mean $a \log \sigma_e + b \log R_e + c$ and standard deviation $\sigma_{\log L} = 0.082$ dex. Notice this Gaussian scatter is added along the direction of $\log L$ only. We further add uniform Gaussian scatter to the mock values of $\log \sigma_e$, $\log R_e$ and $\log L$, to represent (uncorrelated) observational uncertainties. The process is repeated one hundred times, to create one hundred independent realisations of the mock sample. The values of the FP coefficients a , b and c and the FP intrinsic scatter $\sigma_{\log L}$ are taken from fitting LTS_PLANEFIT to the SAMI FP data (Appendix C). As expected, for this test LTS_PLANEFIT recovers the input parameters with no detectable bias (the bias in a , b and c is -0.2% , $+0.8\%$ and $+0.3\%$, respectively; none of these is statistically significant). In contrast, for 3dG the bias in a , b and c is $+11\%$, $+5\%$ and -4% , with significance of 3, 2 and 4 standard deviations, respectively.

These tests show that each of the two algorithms suffers from considerable bias when fitting data taken from a different model (i.e. bias results from using an incorrect model). For this reason, the choice of algorithm is dictated by other considerations. We prefer the 3dG algorithm because a Gaussian model appears to be closer to the distribution of the real data - at least for the SAMI sample (Fig. 6). Whether the scatter should be orthogonal to the plane or along $\log L$ could be explored with a dedicated model, but we defer this analysis to future work. In this work, we address this model uncertainty by marginalising over it, i.e. repeating the analysis with the LTS_PLANEFIT algorithm (Appendix C) and showing that we find a different FP, but the same qualitative results as the 3dG method.

3.3 Outlier rejection

An additional source of bias is represented by outliers. LTS_PLANEFIT is designed to deal with outliers through the eponymous inside-out sigma clipping (Rousseeuw & Driessen 2006, C13). The number of standard deviations beyond which the sample is clipped is set by the value of the keyword CLIP. The optimal value of CLIP depends on the probability distributions of both the sample and of the outliers, which are not known *a priori*. If we assume Gaussian scatter and no outliers (CLIP=0), given our sample size we expect two valid galaxies to lie beyond three standard deviations from the best-fit plane and no galaxy to lie beyond four standard deviations; in fact we find eight and two respectively, and so need to apply sigma-clipping. As the best-fit parameters are statistically consistent between these two choices, we use the more conservative value CLIP=3.

For the 3dG algorithm, we proceed as follows. Even though outliers can in principle be modelled, in practice this is not required because of our good data quality. In fact, we find the same FP by either rejecting the points outside of the

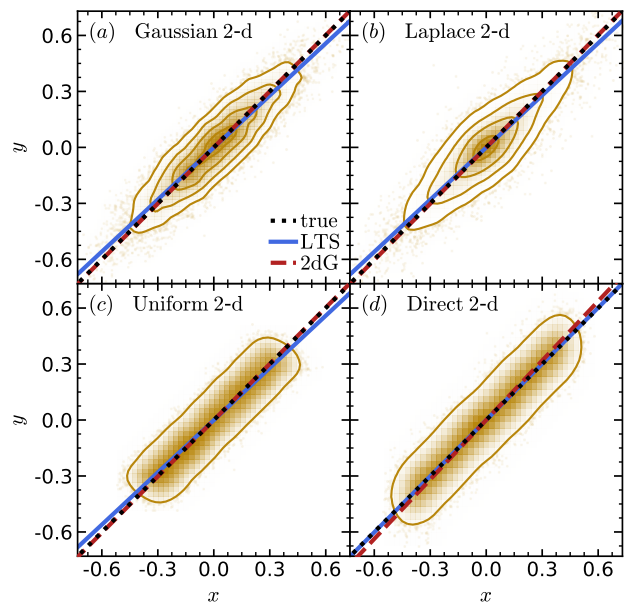


Figure 7. Two-dimensional mock datasets illustrating the bias inherent to different models. The panels compare the results from the LTS_PLANEFIT (solid blue line) and 2dG (dashed red line) algorithms to the true model $y = x$ (dotted black line). The algorithms have been tested with four different generative models: a 2-d Gaussian (panel a), a 2-d Laplace distribution (panel b), a uniform distribution with intrinsic orthogonal scatter (panel c) and a uniform distribution with intrinsic scatter along the y axis (panel d). Each point also includes Gaussian measurement uncertainties. For panels a and b, the contours trace the 12th, 40th, 68th and 86th percentiles of the data (roughly corresponding to 0.5, 1, 1.5 and 2 σ); for panels c and d, the single contour line traces the 90th percentile of the data. For the models with orthogonal scatter (panels a-c), LTS_PLANEFIT infers a systematically smaller rms , at the price of flatter slope m (see Table 7). The opposite is true for the model with scatter along y (panel d): here it is 2dG that infers a systematically steeper slope. This model bias greatly affects the strength of the correlation between the fit residuals Δ and the variables x and y (see Table 1).

contours enclosing the 95th percentile of the data (see e.g. B18) or by using the posterior probability to reject the 1st percentile of the data and repeating the optimisation on the pruned sample (M12). These two post-optimisation methods find largely the same outliers as the robust LTS_PLANEFIT with CLIP=3 (§ 4.1.2). Even though outliers do not affect the FP parameters a , b and c (see Table 3, rows 3–4, columns 3–5) the strictness of the outlier rejection threshold does directly affect the observed rms and intrinsic scatter (columns 6–8).

To test whether our results depend on the model or algorithm used, we repeated the FP analysis using the LTS_PLANEFIT algorithm (Appendix C). Even though the FP parameters differ between the two algorithms (Table 3, rows 1 and 18–19), the main results of this paper are the same for the 3dG and LTS_PLANEFIT algorithms, in that the ranking by significance of the residual correlations is the same.

3.4 Residual correlations

The main scientific goal of this work is to compare various structural and stellar-population parameters to the FP

Table 1. True and inferred model parameters for 2-dimensional mock datasets, illustrating the bias inherent to different models and algorithms (see also Fig. 7). For models with orthogonal intrinsic scatter, direct-fit least-squares minimisation methods (column 5), obtain consistently flatter slopes and smaller *rms* compared to both 2dG (column 4) and to the input model value (column 3). Conversely, for models with intrinsic scatter along y (labelled ‘Direct 2-d’), direct-fit methods recover the input parameters with no bias whereas 2dG infers systematically steeper slope m . The bias in the slope m propagates to the correlation between the residuals Δ and the data (measured here using both covariance Cov and the Spearman rank correlation coefficient ρ). The bias on the residual correlations is both large (50–100%) and statistically significant ($> 10\sigma$).

model	true	2dG	LTS	
(1)	(2)	(3)	(4)	(5)
Gaussian 2-d	m	1	1.003 ± 0.005	0.930 ± 0.004
	rms	0.102	0.103 ± 0.001	0.100
	$10^3 \times \text{Cov}(\Delta, x)$	-6.01	-6.17 ± 0.26	-2.42
	$10^3 \times \text{Cov}(\Delta, y)$	4.49	4.34 ± 0.23	7.66
	$\rho(\Delta, x)$	-0.247	-0.253 ± 0.010	-0.102
	$\rho(\Delta, y)$	0.191	0.185 ± 0.010	0.334
Laplace 2-d	m	1	1.005 ± 0.005	0.932 ± 0.004
	rms	0.103	0.103 ± 0.001	0.100
	$10^3 \times \text{Cov}(\Delta, x)$	-5.99	-6.25 ± 0.26	-2.42
	$10^3 \times \text{Cov}(\Delta, y)$	4.65	4.41 ± 0.23	7.80
	$\rho(\Delta, x)$	-0.285	-0.295 ± 0.010	-0.143
	$\rho(\Delta, y)$	0.209	0.198 ± 0.010	0.349
Uniform 2-d	m	1	1.005 ± 0.005	0.933 ± 0.004
	rms	0.102	0.102 ± 0.001	0.099
	$10^3 \times \text{Cov}(\Delta, x)$	-5.82	-6.10 ± 0.25	-2.43
	$10^3 \times \text{Cov}(\Delta, y)$	4.49	4.24 ± 0.22	7.49
	$\rho(\Delta, x)$	-0.239	-0.250 ± 0.010	-0.101
	$\rho(\Delta, y)$	0.187	0.176 ± 0.010	0.322
Direct 2-d	m	1	1.062 ± 0.004	1.003 ± 0.004
	rms	0.104	0.107 ± 0.001	0.104
	$10^3 \times \text{Cov}(\Delta, x)$	-2.41	-6.59 ± 0.29	-2.61
	$10^3 \times \text{Cov}(\Delta, y)$	8.41	4.39 ± 0.28	8.23
	$\rho(\Delta, x)$	-0.084	-0.229 ± 0.010	-0.091
	$\rho(\Delta, y)$	0.273	0.128 ± 0.010	0.266

Columns: (1) probabilistic model used to generate the data; (2) parameter; (3) input value of parameter; (4) parameter values from the 2dG; (5) parameter value from LTS_LINEFIT algorithm. The mock data and models are illustrated in Fig. 7

scatter, by studying how these observables correlate with the FP residuals: the presence and strength of correlations *may* point to underlying physical trends. For this reason, we discuss here the expected residual correlations between the plane-fit residuals and the data. In § 4 we quantify the strength and significance of residual trends using the Spearman rank correlation coefficient ρ , because it does not penalise non-linear correlations. However, ρ is difficult to relate analytically to the assumed probability distribution; for this reason, in this section we focus on covariance, which is directly related to the *Pearson* correlation coefficient by

$$\rho_{\text{Pearson}} \equiv \frac{\text{Cov}(x, y)}{\sqrt{\text{Cov}(x, x)\text{Cov}(y, y)}} \quad (23)$$

As we shall see, it is in the residual trends with respect to the FP observables that the 3dG and LTS_PLANEFIT algorithms differ the most. This difference is due to the different prob-

ability distribution between the two models. For the infinite plane model, the residuals with respect to the *true* solution correlate with z , but not with x and y . This can readily be ascertained by calculating the covariance explicitly. We define the residuals as

$$\Delta \equiv z - ax - by - c \quad (24)$$

and we integrate the moments of the probability model underlying LTS_PLANEFIT, equation (21), obtaining

$$\begin{aligned} \text{Cov}(\Delta, x) &= 0 \\ \text{Cov}(\Delta, y) &= 0 \\ \text{Cov}(\Delta, z) &= \text{Cov}(z, z) - a\text{Cov}(x, z) - b\text{Cov}(y, z) = \sigma_{\text{int}}^2 \end{aligned} \quad (25)$$

where we have assumed that the integrals

$$\int dx x, \int dx x^2, \int dy y, \int dy y^2 \quad (26)$$

are all finite (i.e. that the probabilities of x and y are uniform over a finite interval that is ‘large’ compared to the thickness of the plane, σ_{int}). For the uncensored 3dG model, we consider the probability distribution equation (15) and find

$$\begin{aligned} \text{Cov}(\Delta, x) &= \left[\mathbf{R}^T \Sigma \mathbf{R} \right]_{xz} - a \left[\mathbf{R}^T \Sigma \mathbf{R} \right]_{xx} - b \left[\mathbf{R}^T \Sigma \mathbf{R} \right]_{xy} \\ \text{Cov}(\Delta, y) &= \left[\mathbf{R}^T \Sigma \mathbf{R} \right]_{yz} - a \left[\mathbf{R}^T \Sigma \mathbf{R} \right]_{xy} - b \left[\mathbf{R}^T \Sigma \mathbf{R} \right]_{yy} \\ \text{Cov}(\Delta, z) &= \left[\mathbf{R}^T \Sigma \mathbf{R} \right]_{zz} - a \left[\mathbf{R}^T \Sigma \mathbf{R} \right]_{xz} - b \left[\mathbf{R}^T \Sigma \mathbf{R} \right]_{yz} \end{aligned} \quad (27)$$

none of which is, in general, zero (censoring further complicates these expressions). Direct fit methods such as LTS_PLANEFIT tend to bias the optimisation towards the assumed model, artificially lowering $|\text{Cov}(\Delta, x)|$ and $|\text{Cov}(\Delta, y)|$ and increasing $|\text{Cov}(\Delta, z)|$. The conclusion is that, whenever residual correlations are important, direct-fit methods are not a good solution.

To better illustrate the implications, we use a two-dimensional example. In Fig. 7 we present three mock datasets, consisting of 10,000 points generated from a probability distribution with mean $\mathbf{0}$ and symmetry axes $x = y$ and $x = -y$. Along these axes, the standard deviations were chosen to match the values of the fiducial FP (Fig. 9). The generative probability distributions are a 2-d Gaussian (panel a), a 2-d Laplacian distribution (panel b), a uniform distribution with orthogonal scatter (labelled ‘Uniform 2-d’, panel c), and a uniform distribution with scatter along the y axis (labelled ‘Direct 2-d’, panel d). Each point was convolved with a 2-d Gaussian reproducing the measurement uncertainties on the FP observables. The dotted black line has equation $y = x$ and represents the true model, with slope $m = 1$ and zero-point $q = 0$. The dashed red and solid blue lines are the models inferred with the 2dG and LTS_LINEFIT algorithms, respectively. For the models with orthogonal scatter (panels a-c), the LTS algorithm has consistently shallower slope m and lower *rms* (Table 1, column 5) compared to both the 2dG model (column 4) and, revealingly, even the true value (column 3). Within the realm of plausible FP models, the bias does not depend on the functional form of the true model, because it is identical between the three mock datasets. Conversely, the 2dG algorithm consistently finds the true solution and the true *rms* (Table 1, column 4). Crucially, the bias of the LTS solution propagates

to the correlations between the residuals $\Delta \equiv y - (mx + q)$ and the variables x and y . As predicted for the 3-d case, the correlation with the independent variable decreases (in absolute value) and the correlation with the dependent variable increases. Unsurprisingly, this bias becomes more/less severe with decreasing/increasing aspect ratio of the data: the more the data tends to the infinite line, the more accurate direct-fit solutions become. In contrast, the 2dG algorithm recovers the underlying model and the correct residual correlations even for ‘thick’ (high-scatter) correlations and for non-Gaussian scatter (Table 1, column 4). On the other hand, for the model with scatter along the y axis, it is the LTS algorithm that recovers the true model parameters and residual correlations, with 3dG finding steeper slope m and stronger (weaker) correlations between the residuals Δ and x (y). The fact that the 3dG and `LTS_PLANEFIT` algorithms have different correlations between the FP residuals and the FP variables L , R_e and σ_e (cf. § 4.2), means that our results depend on the model (and hence method) that we adopt. This undesirable dependency also extends to the correlations between the FP residuals and the other structural and stellar-population observables, because these observables correlate in turn with the FP variables (e.g. *age* correlates with L and σ_e). For the reasons discussed above (§ 3.2), we adopt the 3-d Gaussian as the model of choice and the 3dG algorithm as the default method. Therefore, in the following, we adopt the 3dG FP as the fiducial FP. Nevertheless, it is important to test our results against other model/algorithms, with `LTS_PLANEFIT` representing the most different alternative. We find that for most of the residual correlations (including those with the highest significance) there is no qualitative difference between the results of the 3dG and `LTS_PLANEFIT` algorithms. Consequently, the interpretation of our results does not, in this case, depend on the adopted model.

4 RESULTS

We present the fiducial FP for SAMI (§ 4.1), including its dependence on a number of assumptions (§§ 4.1.1–4.1.6). We then study the residuals of the FP and compare them: (i) to the FP variables (§ 4.2); (ii) to a set of structural parameters (§ 4.3); and (iii) to a set of stellar-population properties (§ 4.4). The most significant correlation is with stellar-population age. We show that this correlation arises from the large scatter in the relation between stellar mass-to-light ratio and surface mass density at any given position on the FP (§ 4.5). We then use mock data to isolate the effect of stellar-population trends with velocity dispersion and size on the tilt and scatter of the FP (§ 4.7).

4.1 The fiducial SAMI Fundamental Plane

Based on the considerations in § 3, we use the 3dG algorithm to find the fiducial FP. We stress again that the fiducial plane is not the plane with the least *rms*, but the plane with the *least bias*. The fiducial FP for SAMI ETGs has equation

$$\log\left(\frac{L}{L_{\odot,r}}\right) = a \log\left(\frac{\sigma_e}{\text{km s}^{-1}}\right) + b \log\left(\frac{R_e}{\text{kpc}}\right) + c \quad (28)$$

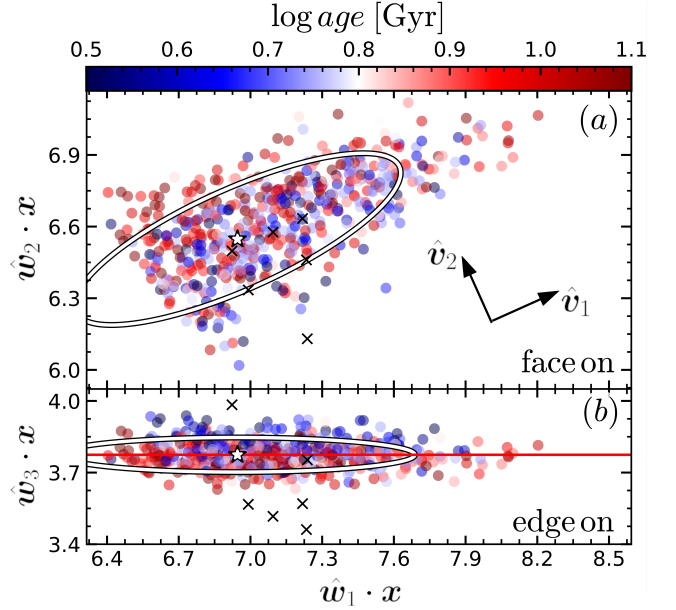


Figure 8. The fiducial FP for the SAMI ETGs, shown face on (panel a) and edge on (panel b). Each circle represents a SAMI galaxy, colour-coded by light-weighted SSP age (the six crosses are outlier galaxies). For ETGs, there is a clear age trend across the FP. The white ellipses centred on the white star show the projection of the fiducial model. The solid red line in panel b represents the edge-on FP. The axes of the ellipse are equal to three times the *intrinsic* dispersion of the 3-d Gaussian. The adopted vector base $\{\hat{w}_1, \hat{w}_2, \hat{w}_3\}$ is expressed in terms of a and b only (equation 29); this base is closely related to the eigenvectors of the 3-d Gaussian model $\{\hat{v}_1, \hat{v}_2, \hat{v}_3\}$: $\hat{w}_3 \equiv \hat{v}_3$, whilst \hat{v}_1 and \hat{v}_2 are illustrated by the arrows in panel a (downscaled by a factor three for illustration purposes). The transformation matrix between the \hat{v}_i ’s and \hat{w}_i ’s is reported in Table 2.

where $a = 1.294 \pm 0.039$, $b = 0.912 \pm 0.025$, and $c = 7.067 \pm 0.078$. Along the direction of $\log L$, the FP has $rms = 0.104 \pm 0.001$ and intrinsic scatter $\sigma_{\log L} = 0.090 \pm 0.004$ dex (the intrinsic orthogonal scatter is $\sigma_{\perp} = 0.048 \pm 0.002$ dex, see Table 3). Notice that we report the *rms* along $\log L$ because this value is easier to compare between different studies, which may find different FP coefficients. For each model parameter we quote as the fiducial value the 50th percentile of the marginalised posterior probability distribution, while the uncertainties are the semi-difference between the 84th and 16th percentiles. These uncertainties are of the order of 2–3% and set the significance threshold to assess the effect of the assumptions that we test below. With the fiducial values of a and b , the resulting tilt of the FP relative to the virial plane is 0.706 and 0.088 in the directions of $\log \sigma_e$ and $\log R_e$ respectively³.

The face-on and edge-on projections of the fiducial plane are shown in in Fig. 8. Rather than using the eigenvectors $\{\hat{v}_1, \hat{v}_2, \hat{v}_3\}$ of the fiducial 3-d Gaussian, we use

³ With the Gaussian assumption we adopt, the usual practice of subtracting the FP coefficients a and b from their virial equivalent introduces a bias; the correct approach is to consider the difference between the random variables L and $M_{\text{vir}}(\sigma_e, R_e)$ and combine their covariance matrices.

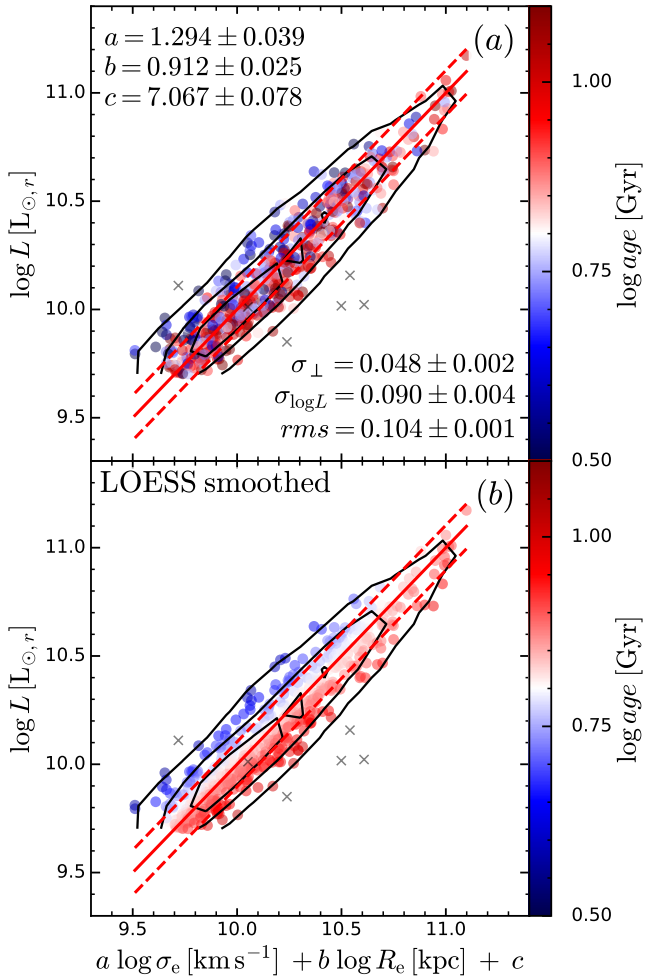


Figure 9. The fiducial FP for the SAMI ETGs, showing a clear age gradient across the plane. Each circle represents a SAMI galaxy, colour-coded by SSP age (panel a) or by LOESS-smoothed SSP age (panel b). Black crosses mark galaxies excluded from the fit; after an initial fit, they lie in the 1st percentile of the posterior probability distribution (the cross that lies near the plane is excluded because it lies far from the galaxy locus within the plane). The best-fit FP is traced by the solid red line, whereas the dashed red lines encompass $\pm rms$. The solid black contours enclose the 40th, 68th, and 96th percentiles of the data distribution. There is a clear age gradient across the FP: at fixed σ_e and R_e , old galaxies (red hues) are under-luminous and lie preferentially below the best-fit plane, and conversely for young galaxies (blue hues).

the base $\{\hat{w}_1, \hat{w}_2, \hat{w}_3\}$ because, unlike the eigenvectors, all the \hat{w}_i 's can be expressed in the base of the observables $\log \sigma_e, \log R_e, \log L$, using only the FP coefficients a and b

$$\begin{aligned} \mathbf{w}_1 &\equiv \begin{pmatrix} 0 & 1/b & 1 \end{pmatrix} \\ \mathbf{w}_2 &\equiv \begin{pmatrix} (1+b^2)/(ab) & -1 & 1/b \end{pmatrix} \\ \mathbf{w}_3 &\equiv \begin{pmatrix} -a & -b & 1 \end{pmatrix} \end{aligned} \quad (29)$$

where the unit vectors are given by $\hat{w}_i \equiv \mathbf{w}_i / \|\mathbf{w}_i\|$. Notice that $\hat{v}_3 = \hat{w}_3$, so this choice of base preserves the edge-on view of the FP (Fig. 8b) and is equivalent to a coordinate rotation within the FP. The relation between (\hat{v}_1, \hat{v}_2) and (\hat{w}_1, \hat{w}_2) is illustrated by the arrows in panel b: \hat{w}_1 is very close to \hat{v}_1 , but combines only photometric observables.

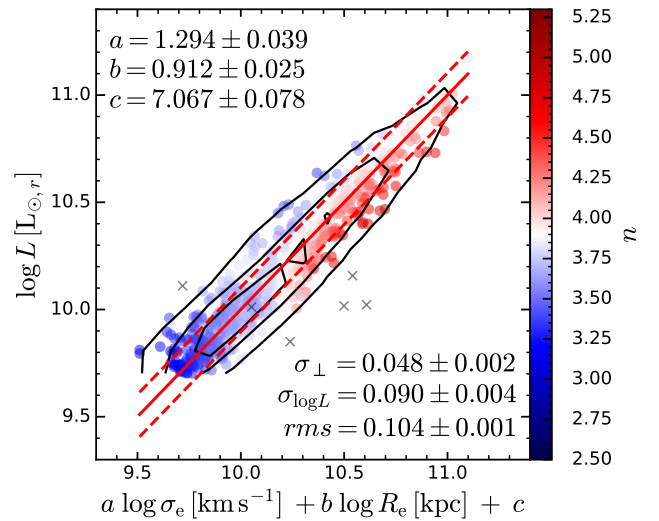


Figure 10. The fiducial FP, colour-coded with the LOESS-smoothed Sérsic index n ; symbols are otherwise the same as in Fig. 9. Compared to SSP age, n shows a trend both along the FP and across the FP.

The transformation between our base \hat{w}_i and the eigenvector base \hat{v}_i is given in columns 1–3 of Table 2.

In Fig. 8, the white stars and ellipses trace the centroid and the 2-d projections of the fiducial 3-d Gaussian; the axes of the ellipses are equal to three times the *intrinsic* dispersion. Because of observational uncertainties, our data extends further than the ellipses (which should otherwise enclose 99% of the data). Each circle represents a galaxy (black crosses are outliers), colour-coded by its light-weighted SSP age: there is a clear age trend across the plane (panel b); this trend is also visible in Fig. 9, where we show predicted vs measured $\log L$. Here the solid red line is the 1:1 relation and the red dashed lines are offset by the observed rms . The solid black contours enclose respectively the 40th, 68th, and 96th percentiles of the data distribution (corresponding roughly to 1, 1.5 and 2.5 standard deviations of the 2-d data distribution). In panel b, the age distribution has been smoothed using the LOESS algorithm (Cappellari et al. 2013b), highlighting the strong age gradient across the plane: at fixed σ_e and R_e , the oldest galaxies (red hues in Figs 8 and 9) are under-luminous compared to the FP prediction, and lie preferentially below the fiducial plane; the opposite is true for the youngest galaxies (blue hues). In contrast, when colouring the FP with Sérsic index n , the colour trend is both *across* and *along* the FP (Fig. 10).

In §§ 4.2–4.4, we quantify the correlation between the FP residuals and a number of galaxy observables, finding SSP age to be the best predictor of the FP residuals. However, before delving into the study of the residuals, we review below how our assumptions affect the FP determination. We do so by changing one assumption at a time and by comparing the resulting FP to the fiducial FP. A summary of the results is reported in Table 3.

4.1.1 Sample uncertainties

We estimate the sample random uncertainty by bootstrapping the FP sample one thousand times and find the un-

Table 2. Transformation between the eigenvectors of the fiducial 3-d Gaussian $\{\hat{\boldsymbol{v}}_1, \hat{\boldsymbol{v}}_2, \hat{\boldsymbol{v}}_3\}$ and the vector base $\{\hat{\boldsymbol{w}}_1, \hat{\boldsymbol{w}}_2, \hat{\boldsymbol{w}}_3\}$ from Fig. 8 and equation (29). $\hat{\boldsymbol{l}}_3$ is the normal to the LTS best-fit model (for this model, the distribution within the FP is not constrained, therefore there is only a single vector).

	$\hat{\boldsymbol{v}}_i \cdot \frac{\hat{\boldsymbol{w}}_1}{\ \hat{\boldsymbol{w}}_1\ }$	$\hat{\boldsymbol{v}}_i \cdot \frac{\hat{\boldsymbol{w}}_2}{\ \hat{\boldsymbol{w}}_2\ }$	$\hat{\boldsymbol{v}}_i \cdot \frac{\hat{\boldsymbol{w}}_3}{\ \hat{\boldsymbol{w}}_3\ }$	$\hat{\boldsymbol{v}}_i \cdot \frac{\hat{\boldsymbol{l}}_3}{\ \hat{\boldsymbol{l}}_3\ }$	$\hat{\boldsymbol{v}}_i \cdot \hat{\boldsymbol{l}}_3$
	(1)	(2)	(3)	(4)	(5)
	dex	dex	dex	dex	°
$\hat{\boldsymbol{v}}_1$	0.912	0.410	0	0.029	88.3±0.6
$\hat{\boldsymbol{v}}_2$	-0.410	0.912	0	0.048	87.2±1.0
$\hat{\boldsymbol{v}}_3$	0	0	1	0.998	3.2±1.0

Columns: (1–3) scalar product between each eigenvector $\hat{\boldsymbol{v}}_i$ and $\hat{\boldsymbol{w}}_j$; (4) scalar product between each eigenvector $\hat{\boldsymbol{v}}_i$ and the normal to the LTS best-fit plane $\hat{\boldsymbol{l}}_3$; (5) angle between each eigenvector $\hat{\boldsymbol{v}}_i$ and the normal to the LTS best-fit plane.

certainties about a , b , c , rms , $\sigma_{\log L}$ and σ_{\perp} to be respectively 0.036, 0.024, 0.077, 0.004, 0.005 and 0.003 (Table 3, row 2). Except for the rms , these values are consistent with the uncertainties estimated by the 3dG algorithm for the parameters of the fiducial plane. The bootstrapping uncertainty about the rms is larger than the uncertainty calculated from the posterior distribution because the rms is sensitive to the presence and number of outliers. On the other hand, the similarity between the posterior and bootstrapping uncertainties for the other parameters implies that, for these parameters, the total uncertainty is primarily due to measurement uncertainty, rather than sample variance. For studies with significantly smaller sample size than considered here, the relative contribution of sample uncertainty is likely to be higher.

As for systematic errors due to the sample, we run two tests. In § 2.6, we rejected 24 galaxies that, due to their large apparent radius, are not fully covered by the SAMI IFU. This selection is worth considering because these galaxies have larger than average physical radius, so their inclusion/exclusion might bias the FP. We tested their effect in two ways, using $\sigma_{e/4}$ (the aperture velocity dispersion measured inside the isophote of area $\pi(R_e/4)^2$). First, we approximated the 24 missing σ_e values with their aperture-corrected version, based on $\sigma_{e/4}$ ($\sigma_e = \sigma_{e/4} 4^{-0.04}$, Jørgensen et al. 1996). Secondly, we replaced σ_e with $\sigma_{e/4}$ for all galaxies. Both tests return the same FP parameters within the uncertainties, so we conclude that including/removing these galaxies does not affect our conclusions (Table 3, row 3). Likewise, we find that including or excluding the 22 galaxies that have $R_e < \sigma_{\text{PSF}}$ and the 51 galaxies that have $R_e < 0.5 \text{FWHM}_{\text{PSF}}$ (which in principle could systematically affect σ_e) also does not change the FP parameters (Table 3, row 4).

4.1.2 Outliers

We removed six galaxies that have low likelihood according to the fiducial model (probability lower than the 1st percentile of the probability distribution, 3.3). Performing the optimisation while including these six galaxies, the FP parameters a , b and c are unchanged: their variation is at most

2% (Table 3, row 5). The same is true if we use a stricter rejection threshold and trim the 5th percentile of the posterior distribution (Table 3, row 6).

However, relaxing or tightening the rejection criterion has a disproportionate effect on the rms and intrinsic scatter, which increase/decrease by 7–10% (Table 3, columns 6–8). Thus, even though the FP parameters are stable against outliers, we have to consider an additional systematic uncertainty of 10% on the tightness of the plane. While this degeneracy between the strictness of the outlier rejection and the rms is undesirable, it does not affect the main conclusions of this work. Furthermore, the intrinsic scatter of the FP is also degenerate with the measurement uncertainties, which are difficult to quantify absolutely (see § 4.1.5). For this reason, the systematic uncertainty of 10% on the FP intrinsic scatter is to be considered a lower limit and is unlikely to decrease with increasing sample size. We inspected the six outliers (crosses in Fig. 9), and found that: one galaxy has a prominent neighbour and the measured R_e is overestimated by a factor of 2; one galaxy is a post-starburst galaxy and lies at the edge of the colour-mass diagram; one galaxy has low surface brightness and, even though it lies on the plane, it lies far from the FP 3-d Gaussian within the plane (Fig. 9); one galaxy has σ_e over-estimated by a factor of two (as determined by comparing to observations in worse seeing conditions); and, finally, there are two galaxies where the origin of the discrepancy is unclear.

Except for the outlier that has low surface brightness, all the other outliers are rejected also by the LTS algorithm (§ 4.1.6; for the LTS algorithm, there is no preference for where galaxies lie *within* the plane, hence the outlier with low surface brightness is not penalised). We conclude by stressing that the precise nature of these six outliers is not germane to our discussion because, in our study of the FP residuals, we are interested primarily in the FP parameters, which we demonstrated to be insensitive to the rejection threshold adopted. We exclude these six outliers from the study of the FP residuals.

4.1.3 Adopted aperture

Any conventional choice of velocity dispersion does not seem to affect the FP. Our default σ_e is measured inside an elliptical aperture of area πR_e^2 (§ 2.3.1), but the FP parameters and scatter are unchanged whether we use a smaller elliptical aperture of area $\pi(R_e/4)^2$ (Table 3, row 7), a circular instead of elliptical aperture of area πR_e^2 (Table 3, row 8), or a circular aperture of fixed apparent radius (1.5 arcsec radius; Table 3, row 9). Notice that in these tests we used exactly the same sample as the fiducial plane, even though using smaller apertures in principle enables us to include more galaxies (i.e. the 24 large galaxies with incomplete IFU coverage, see § 4.1.1). Given the radial behaviour of aperture σ (Jørgensen et al. 1996), we expect an average increase of 0.024 dex between our fiducial value of σ_e and $\sigma_{e/4}$. To first order, this increase translates into a decrease in a of a factor $0.024/(\log \sigma_e) \approx 0.014$, below our significance threshold (note that we used $\langle \log \sigma_e \rangle = 2.18$ dex, the median $\log \sigma_e$ value over the sample). The measured change in a is in line with our expectations (the largest difference is only 0.7 standard deviations away from the fiducial value). In agreement with Scott et al. (2015), we find that measuring σ inside

Table 3. The parameters of the fiducial Fundamental Plane defined by equation 28 (first row) and their dependence on assumptions about the model and data (rows 2–21). Photometry (MGE or Sérsic), uncertainties on $\log R_e$, and the algorithm used have the largest effect on the FP parameters (rows 11–12, 14 & 17, and 20–21 respectively). The last two rows give the parameters of the mock FPs.

§ (1)	description (2)	a (3)	b (4)	c (5)	rms (6)	$\sigma_{\log L}$ (7)	σ_{\perp} (8)
1* 4.1	fiducial	1.294 ± 0.039	0.912 ± 0.025	7.067 ± 0.078	0.104 ± 0.001	0.090 ± 0.004	0.048 ± 0.002
2 4.1.1	1000 bootstrap.	± 0.036	± 0.024	± 0.077	± 0.004	± 0.005	± 0.003
3 4.1.1	Incl. large targets	1.282 ± 0.037	0.880 ± 0.023	7.089 ± 0.075	0.105 ± 0.001	0.093 ± 0.004	0.050 ± 0.002
4 4.1.1	Excl. small targets	1.297 ± 0.042	0.932 ± 0.032	7.050 ± 0.085	0.106 ± 0.002	0.092 ± 0.004	0.049 ± 0.002
5 4.1.2	No rejection	1.317 ± 0.042	0.900 ± 0.027	7.018 ± 0.085	0.112 ± 0.002	0.100 ± 0.004	0.053 ± 0.002
6 4.1.2	5 th %-ile	1.321 ± 0.039	0.904 ± 0.026	7.007 ± 0.080	0.098 ± 0.001	0.083 ± 0.004	0.044 ± 0.002
7 4.1.3	$\sigma_e \rightarrow \sigma_{e/4}$	1.282 ± 0.040	0.892 ± 0.026	7.085 ± 0.079	0.106 ± 0.001	0.093 ± 0.004	0.050 ± 0.002
8 4.1.3	$\sigma_e \rightarrow \sigma_e^{\text{circ}}$	1.292 ± 0.039	0.917 ± 0.025	7.072 ± 0.076	0.104 ± 0.001	0.091 ± 0.004	0.048 ± 0.002
9 4.1.3	$\sigma_e \rightarrow \sigma_{1.5''}$	1.296 ± 0.039	0.877 ± 0.026	7.069 ± 0.080	0.105 ± 0.001	0.092 ± 0.004	0.049 ± 0.002
10 4.1.4	$R_e \rightarrow R_e^{\text{maj}}$	1.311 ± 0.040	0.874 ± 0.025	6.998 ± 0.081	0.106 ± 0.002	0.094 ± 0.004	0.050 ± 0.002
11† 4.1.4	MGE phot.	1.294 ± 0.040	0.922 ± 0.028	7.071 ± 0.081	0.103 ± 0.002	0.090 ± 0.004	0.048 ± 0.002
12† 4.1.4	Sérsic phot.	1.376 ± 0.044	0.825 ± 0.025	6.912 ± 0.090	0.113 ± 0.002	0.101 ± 0.004	0.054 ± 0.002
13 4.1.5	$0.5 \times u_{\log \sigma_e}$	1.274 ± 0.038	0.923 ± 0.025	7.107 ± 0.077	0.103 ± 0.001	0.093 ± 0.004	0.050 ± 0.002
14 4.1.5	$0.5 \times u_{\log R_e}$	1.336 ± 0.039	0.880 ± 0.024	6.985 ± 0.078	0.104 ± 0.002	0.096 ± 0.004	0.051 ± 0.002
15 4.1.5	$0.5 \times u_{\log L}$	1.294 ± 0.038	0.916 ± 0.025	7.066 ± 0.078	0.104 ± 0.001	0.092 ± 0.004	0.049 ± 0.002
16 4.1.5	$1.5 \times u_{\log \sigma_e}$	1.322 ± 0.039	0.896 ± 0.025	7.010 ± 0.079	0.104 ± 0.002	0.086 ± 0.004	0.045 ± 0.002
17 4.1.5	$1.5 \times u_{\log R_e}$	1.210 ± 0.038	0.975 ± 0.027	7.230 ± 0.078	0.104 ± 0.002	0.077 ± 0.004	0.041 ± 0.002
18 4.1.5	$1.5 \times u_{\log L}$	1.286 ± 0.038	0.911 ± 0.024	7.085 ± 0.077	0.103 ± 0.001	0.086 ± 0.004	0.046 ± 0.002
19 4.1.5	Uncorr. noise	1.277 ± 0.037	0.922 ± 0.025	7.100 ± 0.077	0.104 ± 0.001	0.086 ± 0.004	0.046 ± 0.002
20 4.1.6	No censoring	1.277 ± 0.039	0.899 ± 0.026	7.109 ± 0.077	0.104 ± 0.001	0.091 ± 0.004	0.049 ± 0.002
21 4.1.6	LTS, CLIP=3	1.149 ± 0.033	0.896 ± 0.025	7.389 ± 0.073	0.100 ± 0.004	0.082 ± 0.005	0.047 ± 0.003
22‡ 4.7.1	$L \equiv M_{\text{vir}}/\Upsilon_{\star}$	1.720 ± 0.051	1.198 ± 0.033	6.282 ± 0.103	0.137 ± 0.002	0.097 ± 0.006	0.042 ± 0.003
23‡ 4.7.1	$L \equiv M_{\text{vir}}/\Upsilon_{\star}(\Sigma_{\text{vir}})$	1.756 ± 0.050	1.196 ± 0.033	6.201 ± 0.101	0.138 ± 0.002	0.098 ± 0.006	0.042 ± 0.003

Columns: (1) row identifier and reference in main text; (2) brief description of the FP, with full details at reference in main text; (3–5) best-fit FP coefficients and zero-point; (6–8) FP scatter: the observed (rms) and intrinsic ($\sigma_{\log L}$) scatter in the direction of $\log L$ and the intrinsic orthogonal scatter (σ_{\perp}); in addition the FP scatter has 10% systematic uncertainty, estimated by comparing different levels of outlier rejection.

* The fiducial FP uses a censored 3-d Gaussian model, assuming correlated noise between σ_e and R_e and between R_e and L ; to reject outliers we mask the galaxies belonging to the 1st percentile of the posterior probability distribution and repeat the optimisation.

† These two tests use a restricted sample of 516 galaxies with both Sérsic and MGE photometry, selected with identical quality cuts.

‡ These two planes use mock luminosities derived from the virial mass estimator and from the stellar mass-to-light ratio Υ_{\star} .

circular apertures yields a slightly lower rms , but with our sample size and systematic uncertainties this result is not statistically significant.

4.1.4 Adopted photometry

Replacing MGE circularised effective radii with major-axis effective radii changes the FP parameters by 2% (Table 3, row 10), below the significance threshold of 3%. Even though major-axis effective radii are systematically larger than circularised effective radii, for our ETG sample we find that the average difference is modest ($\approx 10\%$ or 0.04 dex). This is likely to change for a sample with a significantly different fraction of fast rotators (Bernardi et al. 2020).

If we swap MGE for Sérsic photometry (including re-measuring σ_e inside the Sérsic half-light radius), we find significantly different FP parameters. For a fair comparison, we ensured that the two FPs have exactly the same galaxies: we repeat the MGE FP optimisation on the subset of galaxies that have both Sérsic and MGE photometry (516 galaxies).

For this restricted MGE-based FP, we find the same parameters as for the fiducial FP (the largest difference is 3%; Table 3, row 11). Compared to the restricted MGE FP, the Sérsic-photometry FP has 7% larger a and smaller b but the same value of c (Table 3, row 12). The observed rms is 9% larger, which suggests we should increase the measurement uncertainties on the Sérsic parameters; furthermore, for the Sérsic FP we assumed the same correlated noise as for the MGE FP, whereas in reality Sérsic-based luminosity and effective radii have stronger correlated noise than the MGE equivalents (e.g. M12). Increasing the Sérsic measurement uncertainties and their correlations does not change the rms , but reduces the intrinsic scatter, which otherwise is 13% larger than the MGE equivalent. These results suggests that, for the data available here, the precision of the MGE photometry is superior. Notice, however, that Sérsic photometry was derived independently for field and cluster galaxies, and given that there is no overlap between these two sets, it is not possible to calibrate the two measurements. Repeating the comparison with a much larger sample, de Vaucouleurs and

MGE photometry yield comparable results (F. D'Eugenio, in prep.). In conclusion, even though our tests are not definitive in assessing whether MGE or Sérsic profiles yield the tightest FP, we infer that the adopted photometry introduces a 7% systematic uncertainty on the FP parameters. Nonetheless, the main results of this paper are unchanged if we adopt Sérsic photometry, including the ranking of residual correlations.

4.1.5 Noise estimates and correlated noise

In the fiducial model, we determine the measurement uncertainties by comparing MGE and Sérsic measurements, with the assumptions that (i) the observed rms is mostly due to observational uncertainties and (ii) the MGE and Sérsic measurements have comparable uncertainties so each contributes $1/\sqrt{2}$ to the observed rms . For σ_e , we compare the scatter between repeat observations. How does under/over-estimating the uncertainties affect the FP parameters?

Increasing or decreasing the measurement uncertainties on $\log \sigma_e$ by 50% does not change the FP parameters or scatter (changes are about one standard deviation; Table 3, rows 13 and 16). The same is true if we change the uncertainties on $\log L$ (Table 3, rows 15 and 18). In contrast, changing the uncertainty on $\log R_e$ has a measurable impact on the FP parameters: halving the uncertainty has no measurable effect, but increasing the uncertainties by 50% changes the values of a , b and c by up to three standard deviations (Table 3, rows 14 and 17). Because the uncertainty on the difference is $\sim \sqrt{2}$ larger than the standard deviation on the fiducial parameters, these differences are not statistically significant. However, further increasing the measurement uncertainties to $2\times$ larger than the fiducial value continues the trend and breaks the significance threshold of three standard deviations. The different behaviour of $\log R_e$ compared to $\log \sigma_e$ and $\log L$ is due to the fact that $\log R_e$ has the largest measurement uncertainties.

This test also illustrates the degeneracy between measurement uncertainties and the FP intrinsic scatter: increasing/decreasing the value of the uncertainties does not change the observed rms , but decreases/increases both $\sigma_{\log L}$ and σ_{\perp} (Columns 6–8 in Table 3).

In our fiducial model, we assume correlated measurement errors between R_e and σ_e , and between R_e and L . Neglecting both correlations, considering only one at a time, or doubling the value of the correlation does not change the value of the best-fit parameters. The largest discrepancy with respect to the fiducial FP occurs when neglecting all correlations: in this case the largest differences are at the level of 1%, below both statistical and sample uncertainties. The effect of correlated noise is apparent however in the intrinsic FP scatter; while the rms is the same as reported for the fiducial FP (Table 3, row 19), the orthogonal scatter is lower (4%), because neglecting correlated noise confounds the artificial tightening due to correlated noise with the intrinsic tightness of the FP.

In conclusion, even though the absolute size and correlation of the measurement uncertainties can affect the FP parameters and does affect the FP scatter, we explicitly demonstrate that the analysis of the residual trends is unchanged within the range of uncertainties explored here.

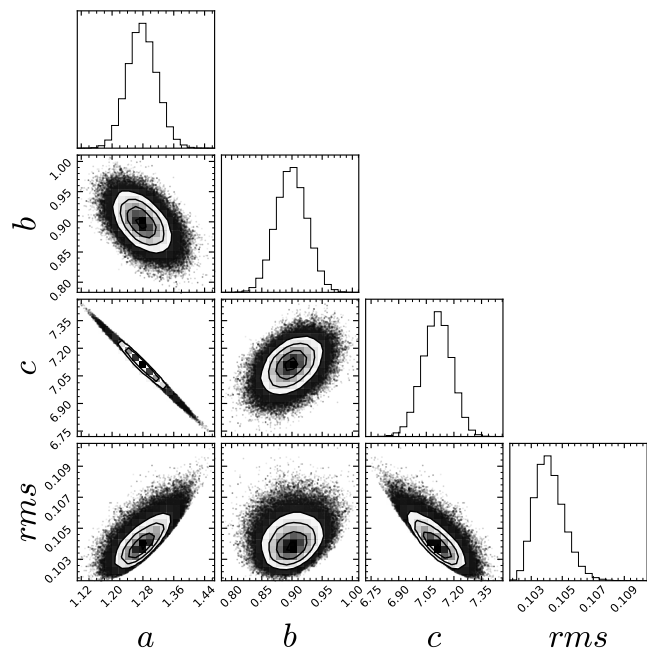


Figure 11. The posterior distribution for the fiducial FP, showing the 1-d and 2-d distributions over a , b , c and rms . This figure explains why the LTS algorithm has lower rms and a but larger c compared to the fiducial FP (cf. rows 1 and 21 of Table 3). The LTS algorithm minimises the rms but, because of the strong correlation between rms and a ($\rho = 0.71$), the minimum possible rms causes a to be under-estimated. This bias, in turn, causes c to be over-estimated, because of the strong anti-correlation between a and c ($\rho = -0.99$). Notice that these considerations apply to a model with orthogonal scatter; assuming a probabilistic model with intrinsic scatter along $\log L$, the 3dG algorithm would be biased to steeper a (§ 3.2).

4.1.6 Model choice

For a fair comparison between the 3dG and LTS algorithms, we repeat the 3dG fit without censoring (Table 3, row 20). We compare this FP to the LTS FP, and find the same value of b , but smaller a and larger c (four standard deviations; these results are qualitatively consistent with the findings of Bernardi et al. 2003). As we have seen in § 3.4, this large difference in a and c is explained as follows. First, there is a strong correlation between a and the observed rms ; because direct fits minimise the rms , they also tends to bias a to lower values. Second, given that a and c are strongly anti-correlated, the decrease in a must be compensated by an increase in c (Fig. 11). In three dimensions, the normal to the LTS FP \hat{l}_3 is only $3.2 \pm 1.0^\circ$ from the normal to the fiducial FP; we report the components of \hat{l}_3 along the eigenvectors of the 3-d Gaussian model, as well as the enclosed angles (Table 2, columns 4 & 5).

We also find that the LTS FP, which ignores correlated noise, has intrinsic scatter $\sigma_{\log L}$ 10% smaller than the fiducial FP, but only 4% smaller than the intrinsic scatter inferred with the 3dG algorithm when ignoring correlated noise (Table 3, row 19).

4.1.7 Summary of method, model and sample uncertainties

In summary, we find that the two changes that have the largest impact on the FP parameters are the model choice (Table 3, row 21) and the method used to measure the photometry (Table 3, row 12). Ignoring correlated noise has a measurable impact on the inferred intrinsic scatter (Table 3, row 19). With our sample size, all the other tests did not significantly change the FP parameters. However, it is reasonable to assume that some of the reported changes are not random, even though they are not statistically significant. The reason is that some changes go in the direction expected from physical considerations (e.g. using a smaller aperture to measure the kinematics yields on average higher dispersion, and the resulting FP coefficient a is therefore lower). For this reason, (i) changing more than one aspect at a time may well cause significant changes to the FP parameters and (ii) using a larger sample may reveal that some of the highlighted changes are statistically significant. Crucially, none of these tests affect, at least in a qualitative way, the main results of our analysis: the relative significance of the residual correlations is unchanged.

4.2 Residuals with respect to the primary FP variables

In the following, in order to uncover the origin of the FP scatter and the age trend across the FP (Fig. 9), we study the residuals about the FP as a function of various galaxy observables. The residuals are defined as the difference $\Delta \log L$ between the observed $\log L$ and the value of $\log L$ inferred from the fiducial FP

$$\Delta \log L \equiv \log L - (a \log \sigma_e + b \log R_e + c) \quad (30)$$

Our results are qualitatively unchanged if we use orthogonal residuals, but we prefer the residuals in $\log L$ for ease of comparison with other works.

In Fig. 12 we show the residuals about the fiducial FP ($\Delta \log L$) as a function of the FP variables $\log \sigma_e$, $\log R_e$ and $\log L$. Circles represent individual galaxies and the solid white contour lines enclose the 40th, 68th and 96th percentile of the galaxy distribution. Naively, one would expect all three panels to show no correlation, because the existence of a trend between $\Delta \log L$ and any of the three FP variables suggests that the variable in question contains additional information that could be used to further reduce the $\Delta \log L$ residuals (the target of many optimisation algorithms). However, this expectation is in general incorrect, because the 3dG algorithm does not infer the model with the *least scatter*, but the model that is *most likely* (or, more precisely, infers the region of parameter space enclosing a given fraction of the posterior probability; see § 3.4). The fact that the true model can have (and in general does have) non-zero correlation between the residuals and the independent variable is explicitly shown in Table 1, column 3. Notice that in the three examples with orthogonal intrinsic scatter, the 2dG algorithm recovers the true correlations $\rho(\Delta, x)$ and $\rho(\Delta, y)$, whereas the best-fit LTS model has $\rho(\Delta, x)$ closer to 0 than to the true value, which then pushes $\rho(\Delta, y)$ too away from its true value. For this reason, the presence or ab-

sence of residual correlations is not, by itself, a valid method to assess the goodness of fit.

In order to quantify the correlations, we use `LTS.LINEFIT` to fit a line to the data in each panel of Fig. 12: the filled red regions are the 95% confidence intervals and the dashed red lines are the 95% prediction intervals. The best-fit linear slope m is reported in the top left corner of each panel: in the absence of correlation, we expect m to be statistically consistent with zero. As expected from 3dG and its underlying probability model, we find that the residuals correlate with both $\log \sigma_e$ and $\log R_e$: both the best-fit slopes m and the Spearman rank correlation coefficients ρ are different from zero (for $\log \sigma_e$, $m = -0.181 \pm 0.029$ and $\rho = -0.249 \pm 0.038$, Fig. 12a; for $\log R_e$, $m = -0.096 \pm 0.020$ and $\rho = -0.177 \pm 0.037$, Fig. 12b; see Table 4). In contrast, we find no correlation between $\Delta \log L$ and $\log L$: both the best-fit slope $m = 0.020 \pm 0.015$ and the correlation coefficient $\rho = 0.053 \pm 0.045$ are statistically consistent with zero (Fig. 12c). Given that even the *true* model induces residual correlations between the FP and its variables, the observed residual correlations are not, alone, an indication of model mismatch. In addition, it has been suggested that the FP may deviate from a log-linear relation (e.g. Zaritsky et al. 2006; Wolf et al. 2010), which would also induce residual correlations. However, if non-linearity was the cause of the observed residual trends, we would expect these residuals to also show non-linearity, contrary to what we find in Figs 12a–c.

The presence and significance of residual trends with the FP observables is critical to our analysis, because we set out to investigate the trends between the FP residuals and galaxy observables. Given that most galaxy observables correlate (or anti-correlate) with one or more of the FP variables, we have to consider that the observed (anti)correlations might reflect, at least in part, the correlations we have found so far. For example, velocity dispersion correlates with stellar population age (e.g. Gallazzi et al. 2005), so that (at least in principle) a negative correlation between $\Delta \log L$ and stellar population age could be due entirely to the observed negative correlation between $\Delta \log L$ and $\log \sigma_e$. In the following, we will always discuss whether an observed correlation would be enhanced or weakened by the reported correlations between $\Delta \log L$, $\log \sigma_e$ and $\log R_e$.

4.3 Structural trends

In order to assess the effect of different dynamical properties on the FP we study the presence and significance of trends between the FP residuals and four structural variables: dynamical surface mass density ($\Sigma_{\text{vir}} \propto \sigma_e^2/R_e$, Fig. 13a), the ratio between streaming and random motions ($(V/\sigma)_e$, Fig. 13b), Sérsic index (n , Fig. 13c) and ellipticity (ϵ_e , Fig. 13d).

We find a statistically-significant (>3 standard deviations) residual trend for only one observable: Sérsic index n , where the best-fit slope is -0.156 ± 0.035 and the correlation coefficient is $\rho = -0.180 \pm 0.047$, with a nominal significance of 4.4 standard deviations. The strength of this trend could be over-estimated, because n correlates with $\log \sigma_e$, which in turn anticorrelates with $\Delta \log L$. Neither the dynamical density tracer Σ_{vir} nor the kinematic ratio $(V/\sigma)_e$ shows a significant correlation, although we note the latter

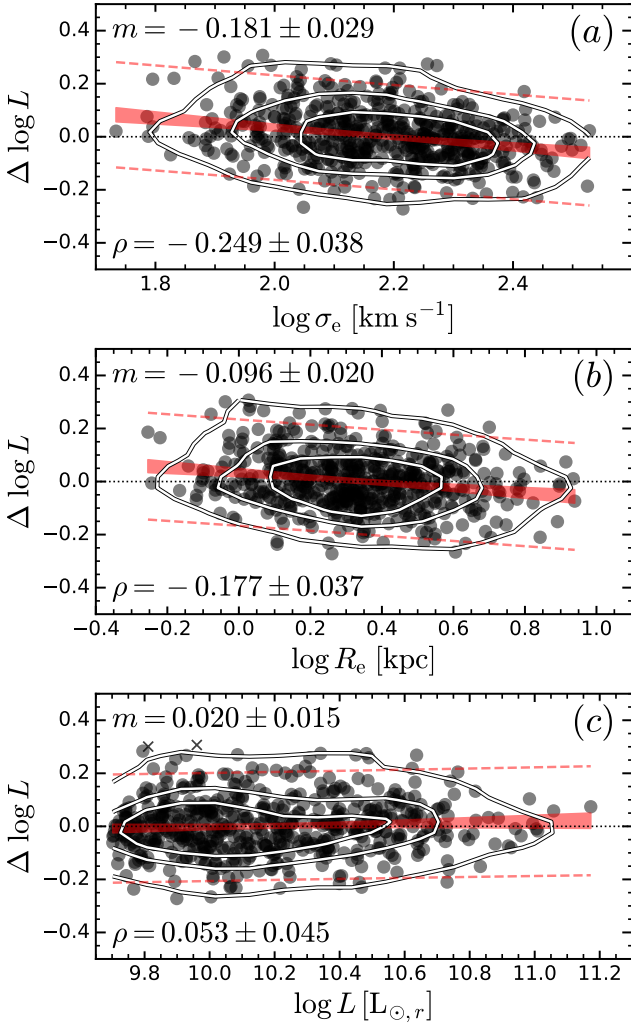


Figure 12. The residuals of the fiducial FP exhibit the expected correlations with the FP observables: $\log \sigma_e$ (top row), $\log R_e$ (middle row) and $\log L$ (bottom row). Each circle represents a SAMI galaxy, the white contour lines enclose the 40th, 68th and 96th percentile of the data distribution. The red line traces the best-fit linear relation, the red regions are the 95% confidence intervals, and the dashed red lines are the 95% prediction intervals. The best-fit linear slope m and the Spearman rank correlation coefficient are reported in the top left and bottom left corner of each panel.

is a projected quantity and the intrinsic (deprojected) value could have stronger correlation. For surface mass density we find no correlation with the FP residuals even if we swap Σ_{vir} with the stellar surface mass densities $\Sigma_*(R < R_e)$ and $\Sigma_*(R < 1\text{kpc})$. This lack of correlation may seem surprising, given the strong link between $\Sigma_*(R < 1\text{kpc})$ and quiescence (Cheung et al. 2012; Fang et al. 2013; Woo et al. 2015), but this apparent discrepancy has a clear explanation (see § 4.6).

We also find no correlation with ϵ_e (best-fit slope 0.068 ± 0.026 and $\rho = 0.101 \pm 0.037$, 2.7 standard deviations significance). However, the strength and significance of this residual trend is likely under-estimated because ϵ_e anticorrelates with $\log \sigma_e$ (Vincent & Ryden 2005). Moreover, among the FP variations shown in Table 3, the fiducial FP (row 1)

is the only one where the significance of the residual correlation between $\Delta \log L$ and ϵ_e is below 3 standard deviations, and the typical significance is ~ 4 standard deviations. Replacing R_e with R_e^{maj} changes the *sign* of the correlation ($\rho = -0.145$; cf. Bernardi et al. 2020).

Because n is the structural parameter showing the most significant residual correlation across the FP, we performed two additional tests. First, we calculated the correlation between $\Delta \log L$ and n for all the FP variations in Table 3. We find the highest significance when using the Sérsic FP (row 12, $\rho = -0.278$) and the least significance for the R_e^{maj} and LTS FPs (rows 10 and 21, $\rho = -0.061$ and $\rho = -0.124$, respectively). In contrast, for stellar population age (the stellar population observable with the most significant correlation), we find a minimum (in absolute value) of $\rho = -0.335$ (for R_e^{maj}) and a maximum of $\rho = -0.430$ (for the Sérsic FP). Second, we study the correlation for two subsets in $\log \sigma_e$. For 330 galaxies with $\sigma_e < 170\text{ km s}^{-1}$ we find no correlation ($\rho = -0.08$, $P = 0.1$; $n = 3.6 \pm 1.1$). In contrast, for as few as 71 galaxies with $200 < \sigma_e < 235\text{ km s}^{-1}$ ($n = 4.3^{+1.7}_{-1.0}$), we find a statistically significant correlation ($\rho = -0.265$, $P < 0.01$).

Taken together, these results suggest that: while the correlation between the FP residuals and n also exists for some limited ranges in σ_e , it is driven by galaxies with large Sérsic index ($n \gtrsim 4$). Given the distribution of n for our representative sample of ETG galaxies, structural differences (non-homology) play a smaller role in the *scatter* of the FP compared to stellar population age (see § 4.4). Alternatively, measurement uncertainties on n are so large that they damp the underlying physical trend. Notice that there is no implication for the role of non-homology on the *tilt* of the FP: as the colour map in Fig. 10 shows, n varies more along the plane than across it. We study the effect of n on the FP tilt in § 4.7.2.

4.4 Stellar population trends

The residuals of the fiducial FP with respect to stellar-population observables are illustrated in Fig. 14. The symbols are the same as in Fig. 12; the only difference is the x axis of each panel. We show $\Delta \log L$ as a function of four observables related to the simple stellar population (SSP) properties of our galaxies: (a) SSP age; (b) SSP metallicity, $[Z/H]$; (c) SSP α -element enrichment, $[\alpha/Fe]$; and (d) r -band mass-to-light ratio, Υ_* .

All the SSP observables show significant correlation. In order of increasing significance, $\Delta \log L$ correlates with $[Z/H]$ ($m = 0.160 \pm 0.040$ and $\rho = 0.175 \pm 0.042$) and anti-correlates with $[\alpha/Fe]$ ($m = -0.593 \pm 0.077$ and $\rho = -0.365 \pm 0.038$), with Υ_* ($m = -0.281 \pm 0.034$ and $\rho = -0.356 \pm 0.042$) and with age ($m = -0.320 \pm 0.038$ and $\rho = -0.380 \pm 0.040$).

SSP age from fixed apertures is already known to correlate with the FP residuals (Forbes et al. 1998; Graves & Faber 2010; Springob et al. 2012). As for n , we check that the correlation with SSP age is not a secondary correlation due to both $\Delta \log L$ and age (anti-)correlating with σ_e , finding that, even at fixed σ_e , there are statistically significant trends. The median ages for the 5th and 95th percentiles of the residual distribution are 4.3 and 9.6 Gyr, respectively.

However, removing young galaxies with $age \lesssim 8\text{ Gyr}$

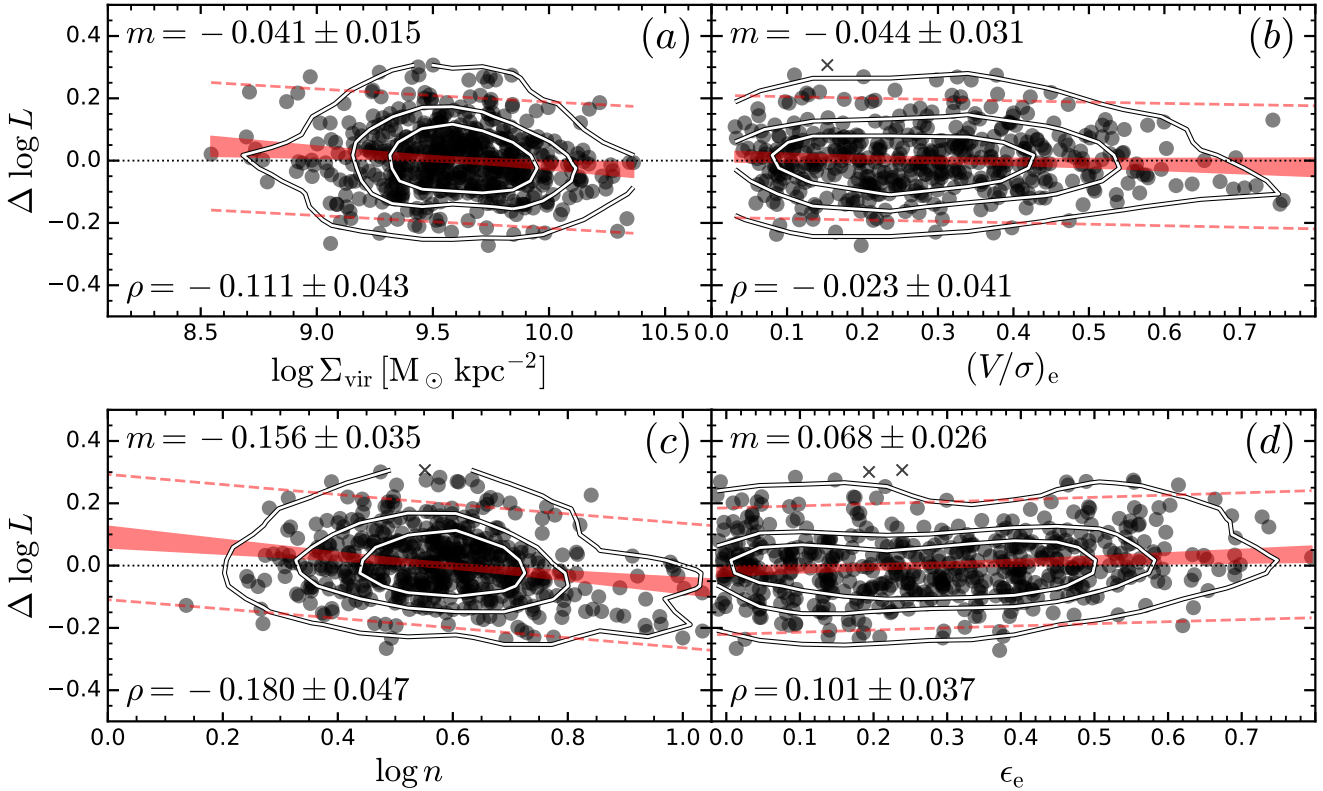


Figure 13. Residuals from the fiducial FP as a function of structural observables. There is a statistically-significant (>3 standard deviations) trend only with Sérsic index n (panel c). We find no evidence of significant correlation with dynamical surface mass density Σ_{vir} (panel a), kinematic ratio $(V/\sigma)_e$ (panel b), or galaxy shape ϵ_e (panel d). Symbols are the same as in Fig. 12.

also removes the trend between age and $\Delta \log L$. This means that we find no correlation for galaxies with $\sigma_e \gtrsim 200 \text{ km s}^{-1}$, because of the correlation between age and σ_e . We also tested that SSP age retains the most significant correlation with $\Delta \log L$ among all the alternative fits considered in Table 3.

Υ_* has the second-most significant correlation, followed by $[\alpha/\text{Fe}]$ and $[\text{Z}/\text{H}]$. Physically, we expect Υ_* to be linked more directly to the FP residuals than SSP age, but larger measurement uncertainties are likely to penalise Υ_* compared to age.

The origin of the strong correlation with $[\alpha/\text{Fe}]$ is unclear, because this observable is connected only weakly to Υ_* , and certainly less so than $[\text{Z}/\text{H}]$. To study the relation between $\Delta \log L$, $[\alpha/\text{Fe}]$ and age we proceed as follows. When we consider a subset of ETGs with fixed $[\alpha/\text{Fe}]$ ($0.2 < [\alpha/\text{Fe}] < 0.25$, 113 targets), we find no correlation between $[\alpha/\text{Fe}]$ and $\Delta \log L$ ($\rho = 0.11$, $P = 0.2$) yet the correlation with age is still highly significant ($\rho = -0.36$, $P = 0.0001$). This suggests that age is the primary driver of the correlation between $\Delta \log L$ and $[\alpha/\text{Fe}]$, because $[\alpha/\text{Fe}]$ and age are themselves strongly correlated ($\rho = 0.50$, $P \ll 10^{-5}$). However, when we take a slice of roughly constant age ($8 < \text{age} < 10$ Gyr, 117 targets), even though we find no correlation between $\Delta \log L$ and age, ($\rho = -0.11$, $P = 0.3$), $[\alpha/\text{Fe}]$ still shows a tentative correlation: $\rho = -0.21$, $P = 0.02$. Although weak, this correlation relies on a much smaller number of galaxies, and in the future it will be worth in-

vestigating this with a larger sample. In § 5.2 we suggest this trend might reflect age information that is captured by $[\alpha/\text{Fe}]$ but not by the absorption features used to estimate light-weighted SSP age (for instance, because of large age uncertainties for old stellar populations). Another possibility is that the observed correlation is due to the correlation between $[\alpha/\text{Fe}]$ and environment density (Liu et al. 2016), but our galaxies are more massive than those considered by Liu et al. (2016). Moreover, environment does not appear to drive the correlation between $\Delta \log L$ and SSP observables; the correlations of $[\alpha/\text{Fe}]$ and age with $\Delta \log L$ are almost unchanged if we split the sample by large-scale environment (i.e. cluster vs field/group) and, in addition, the strength and significance of the correlation between $\Delta \log L$ and environment density Σ_5 are lower than the correlations with both age and $[\alpha/\text{Fe}]$ ($\rho = -0.18$; Σ_5 is the surface density of galaxies inside the circle enclosing the five nearest $M_r < -18.5$ mag neighbours within $\Delta v < 500 \text{ km s}^{-1}$, Brough et al. 2017).

Finally, the correlation with $[\text{Z}/\text{H}]$ also appears to be significant, but there is no evidence of correlation at fixed age. Hence we deem the observed correlation as an artefact of the strong degeneracy between age and metallicity. This conclusion also agrees with the positive physical correlation between $[\text{Z}/\text{H}]$ and Υ_* at fixed age.

In conclusion, of the galaxy observables considered in Table 4, SSP age always has the most significant correlation with $\Delta \log L$. This is true for all the FP variations con-

Table 4. Correlations between the residuals of the fiducial FP and the FP observables (rows 1–3), four structural parameters (rows 4–7) and four SSP parameters (rows 8–11). SSP age and mass-to-light ratio have the most significant correlations.

X axis (1)	$m \pm \sigma_m$ (2)	m/σ_m (3)	ρ (4)	Fig. (5)
$\log \sigma_e$	-0.181 ± 0.029	-6.3	-0.249 ± 0.038	12a
$\log R_e$	-0.096 ± 0.020	-4.8	-0.177 ± 0.037	12b
$\log L$	0.020 ± 0.015	1.3	0.053 ± 0.045	12c
$\log \Sigma_{\text{vir}}$	-0.041 ± 0.015	-2.8	-0.111 ± 0.043	13a
$(V/\sigma)_e$	-0.044 ± 0.031	-1.4	-0.023 ± 0.041	13b
$\log n$	-0.156 ± 0.035	-4.4	-0.180 ± 0.047	13c
ϵ_e	0.068 ± 0.026	2.7	0.101 ± 0.037	13d
$\log \text{age}$	-0.320 ± 0.038	-8.4	-0.380 ± 0.040	14a
$[Z/H]$	0.160 ± 0.040	4.0	0.175 ± 0.042	14b
$[\alpha/\text{Fe}]$	-0.593 ± 0.077	-7.7	-0.365 ± 0.038	14c
$\log \Upsilon_*$	-0.281 ± 0.034	-8.3	-0.356 ± 0.042	14d

Columns: (1) name of the observables being compared to the $\Delta \log L$ FP residuals; (2) best-fit slope of the linear relation between the observable and $\Delta \log L$; (3) best-fit slope in units of the uncertainty; (4) Spearman rank correlation coefficient, with bootstrapping uncertainties; (5) figure showing $\Delta \log L$ vs observable.

considered in Table 3, so the fact that SSP age is the best predictor of the FP scatter is independent (within reason) of outlier rejection, under/over-estimation of uncertainties, adopted photometry, chosen aperture, and algorithm/model choice.

4.5 Structural trends of stellar mass-to-light ratio

Having found that the most significant correlations of $\Delta \log L$ are with SSP parameters, we investigate how these SSP parameters are related to the FP observables σ_e and R_e . We relate these combinations to the virial mass estimator M_{vir} . Following C06, we define M_{vir} by setting $\kappa = 5$ in equation (1). This assumption implies structural homology between galaxies, which C06 validate using dynamical modelling; we also find weak evidence of structural non-homology (§ 4.7.2). We prefer to use the expression with circularised R_e instead of major-axis effective radii (e.g. C13) because it yields less scatter both in the FP and when compared to JAM-derived dynamical masses (Scott et al. 2015). With this definition, we consider three combinations of σ_e and R_e : $M_{\text{vir}} \equiv 5\sigma_e^2 R_e / G \propto \sigma_e^2 R_e$, $\Phi_{\text{vir}} \equiv M_{\text{vir}} / R_e \propto \sigma_e^2$ and $\Sigma_{\text{vir}} \equiv M_{\text{vir}} / (\pi R_e^2) \propto \sigma_e^2 / R_e$. B18 and Barone et al. (2020) have shown that the best predictor⁴ of SSP age is surface mass density Σ_{vir} , whereas the best predictor of SSP $[Z/H]$ is gravitational potential Φ_{vir} . Here we focus on Υ_* , because it appears directly in the FP equation (4) through the expression of luminosity (equation 2). In Fig. 15, we compare Υ_* to virial mass (panel a), gravitational potential (panel b) and surface mass density (panel c). The best-fit linear relations are shown by the solid red lines, with the 95% confidence intervals marked by the red shaded region,

and the dashed red lines enclosing the 95% prediction intervals. The contours enclose the 40th, 68th and 96th percentile of the galaxy distribution. The points are colour-coded with LOESS-smoothed galaxy size, to highlight the presence or absence of residual trends. It is apparent that the relations of Υ_* with both M_{vir} and Φ_{vir} present some residual trends with size, because the colour hues are slanted with respect to the best-fit lines. In contrast, galaxy size appears well mixed in the Υ_* - Σ_{vir} plane, and the small leftover trend is along the relation⁵. This intuition is quantified in three ways. First, ρ increases going from the Υ_* - M_{vir} and Υ_* - Φ_{vir} relations to the Υ_* - Σ_{vir} relation ($\rho = 0.16, 0.30$ and 0.38 respectively; see the bottom left corner of Figs 15a–c). Secondly, the observed *rms* decreases or stays constant from panels a and b to panel c (*rms* = 0.15, 0.14 and 0.14 dex respectively; see the top left corner of Figs 15a–c). This decrease is small (<0.01 dex), but we have to consider that the measurement uncertainties on Σ_{vir} are equal to the measurement uncertainties on M_{vir} , but $\sim 50\%$ larger than the measurement uncertainties on Φ_{vir} (see the discussion in B18). Finally, we study the residuals $\Delta \log \Upsilon_*$ of the three best-fit relations as a function of galaxy size (inset panels of Fig. 15). We find that for the Υ_* - M_{vir} and Υ_* - Φ_{vir} relations the residuals $\Delta \log \Upsilon_*$ have a statistically significant correlation with $\log R_e$ (best-fit slopes $r = -0.36 \pm 0.06$ and $r = -0.31 \pm 0.06$ respectively) whereas for the residuals of the Υ_* - Σ_{vir} relation we find no such correlation ($r = 0.06 \pm 0.06$). These three results, taken together, suggest that the reason the Υ_* - Σ_{vir} relation has the lowest scatter and highest ρ is because it takes into account the mass-to-light ratio information encoded in the range of galaxy sizes at fixed mass M_{vir} and at fixed potential Φ_{vir} .

In principle, this result could be due to correlated noise between Υ_* , σ_e and R_e , but in practice this possibility is unlikely—the only difference between the three panels of Fig. 15 is R_e , which is measured from photometry and is therefore completely independent of both Υ_* and σ_e , which are derived from spectroscopy. For the residual trends shown in the inset panels, there is indeed a strong correlation between errors in $\Delta \log \Upsilon_*$ and R_e , because measurement errors in R_e propagate to σ_e (via the aperture relation; Jørgensen et al. 1996) or because R_e appears directly in the expression of M_{vir} and Σ_{vir} . The results displayed take this correlation into account, but even when setting the correlation to zero our results are qualitatively unchanged: only the residuals of the Υ_* - Σ_{vir} relation have no correlation with galaxy size. We further tested that our conclusions do not change if we repeat the above analysis limiting the sample to elliptical galaxies, or if we use photometric M_* instead of M_{vir} , or if we swap circularised effective radii for semi-major axis effective radii, or if we use GALFIT-based effective radii (either circularised or semi-major axis).

We conclude that, among the structural observables based on σ_e and R_e , the best descriptor of Υ_* is surface mass density. This result is consistent with: (i) Υ_* being primarily determined by age (Renzini 1977; Mould 2020) and (ii) age correlating more tightly with Σ_{vir} than either Φ_{vir} or M_{vir} (B18, Barone et al. 2020). The best-fit relation

⁴ They use ‘best’ in the same sense as we do in this paper: lowest *rms* and highest significance of the correlation.

⁵ Note that LOESS smoothing, by construction, hides the mixing in the scatter plot.

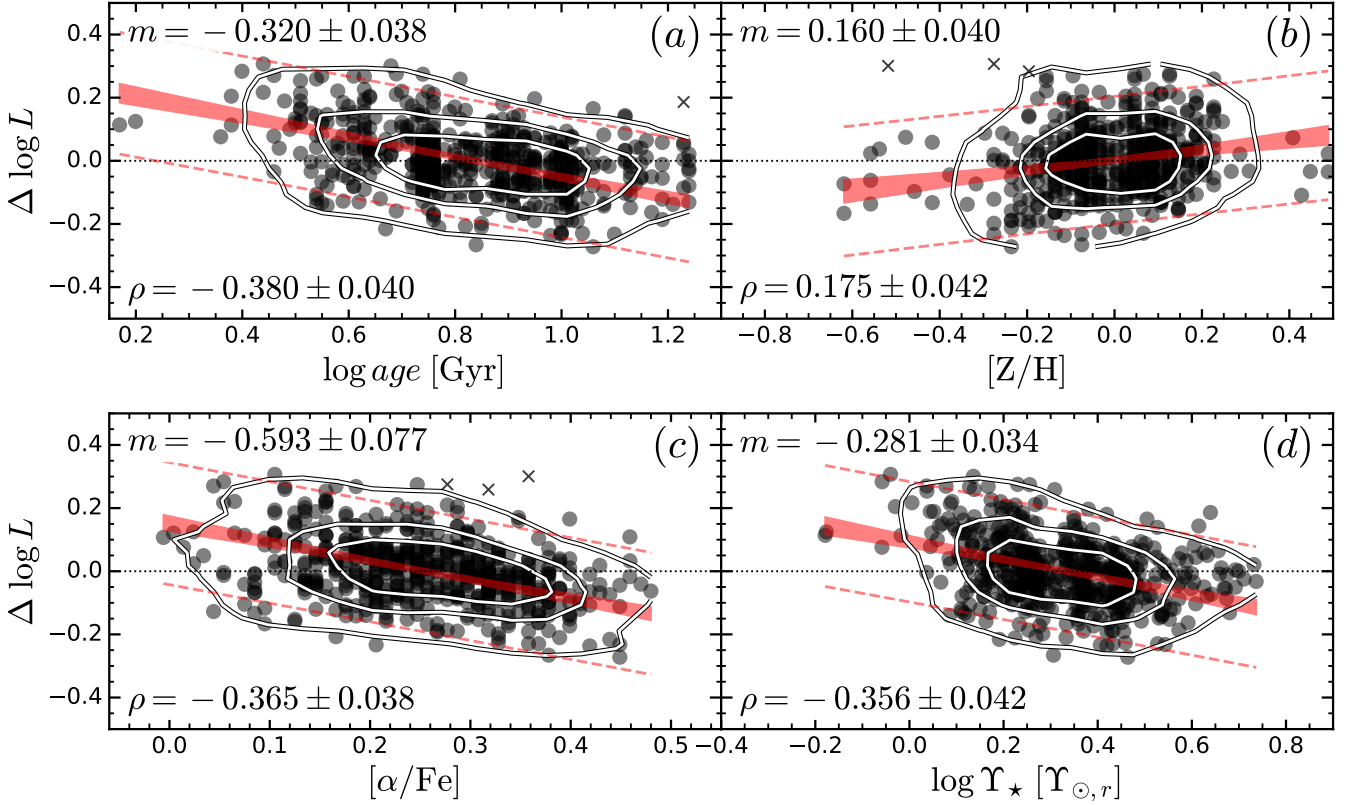


Figure 14. Correlations between the $\Delta \log L$ residuals of the fiducial FP and stellar-population parameters: (a) $\log \text{age}$; (b) $[Z/H]$; (c) $[\alpha/\text{Fe}]$; and (d) $\log \Upsilon_*$. The symbols are the same as in Fig. 12. We find (anti)correlations for $\log \text{age}$, $[\alpha/\text{Fe}]$ and $\log \Upsilon_*$; among these three, the anticorrelations with $\log \text{age}$ and $[\alpha/\text{Fe}]$ have the highest statistical significance (more than seven standard deviations) and the highest rank correlation coefficient (in absolute value).

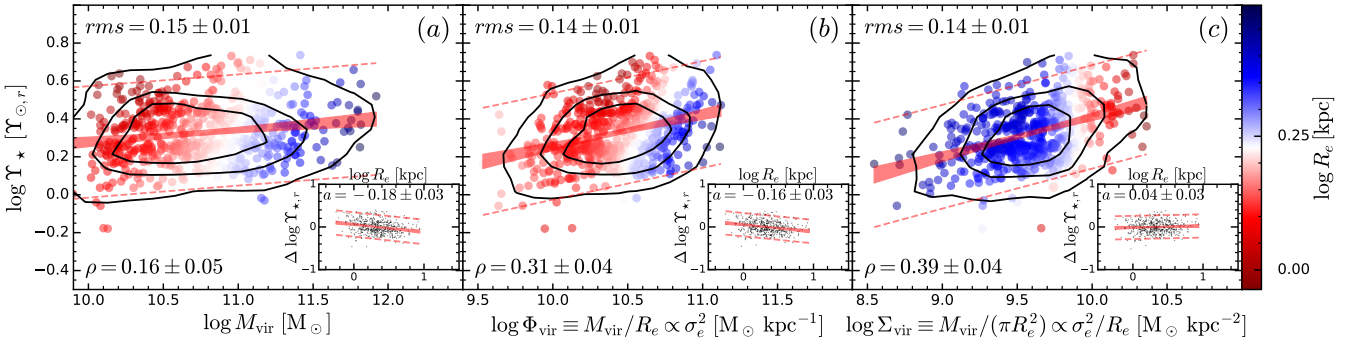


Figure 15. The stellar mass-to-light ratio $\log \Upsilon_*$ is most naturally described as a function of surface mass density Σ_{vir} (panel c). The relations of Υ_* with mass M_{vir} and gravitational potential Φ_{vir} (panels a and b) show more scatter and lower Spearman rank correlation coefficient ρ . The inset diagrams show the residuals of the best-fit relations as a function of effective radius; the relation between $\log \Upsilon_*$ and Σ_{vir} is consistent with no residuals, unlike the other two relations. Low- Σ_{vir} galaxies have a range of sizes; on average, they are larger than the highest- Σ_{vir} galaxies.

between Υ_* and Σ_{vir} is

$$\log \Upsilon_* = (0.207 \pm 0.022) \log \Sigma_{\text{vir}} - (1.654 \pm 0.210) \quad (31)$$

with an observed rms scatter of 0.14 ± 0.01 dex. We estimate the median measurement uncertainties on both $\log \Sigma_{\text{vir}}$ and $\log \Upsilon_*$ to be 0.05 dex, which yields a large intrinsic scatter along $\log \Upsilon_*$ of 0.13 ± 0.01 dex. Using the most conservative

estimates for the uncertainties yields an intrinsic scatter of 0.10 ± 0.01 dex (we used a median uncertainty of 0.11 dex and 0.10 dex for $\log \Sigma_{\text{vir}}$ and $\log \Upsilon_*$, respectively). If we model $\log \Upsilon_*$ as a function of both $\log \sigma_e$ and $\log R_e$, we find

$$\log \Upsilon_* = (0.445 \pm 0.041) \log \sigma_e - (0.187 \pm 0.032) \log R_e - (0.584 \pm 0.089) \quad (32)$$

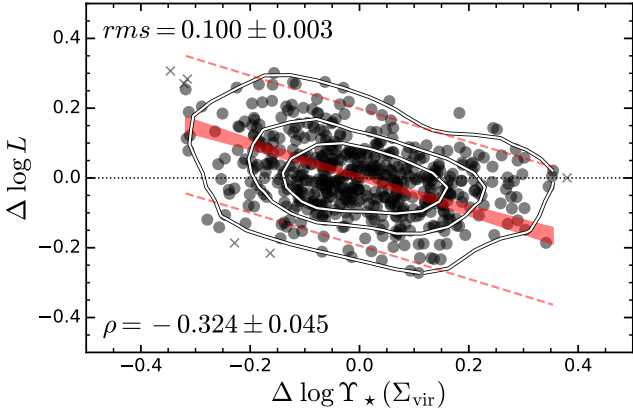


Figure 16. The residuals of the FP, $\Delta \log L$, anticorrelate with the residuals of the Υ_* – Σ_{vir} relation, $\Delta \log \Upsilon_*(\Sigma_{\text{vir}})$: at any fixed position on the FP, galaxies that lie above the Υ_* – Σ_{vir} (or age– Σ_{vir}) relation have higher stellar mass-to-light ratio, are therefore less luminous compared to the average galaxy at that position, and so lie below the FP. The FP residuals do not correlate with Σ_{vir} (Fig. 13a) because the FP already encapsulates the mean Υ_* variation along the Υ_* – Σ_{vir} relation (Fig. 15c).

in statistical agreement with the previous equation, once we express Σ_{vir} as a function of σ_e and R_e . In particular, we find that the ratio between the coefficients of $\log R_e$ and $\log \sigma_e$ is -0.42 ± 0.08 , statistically consistent with the value -0.5 appropriate if the correlation was with $\log \Sigma_{\text{vir}}$.

We thus arrive at an apparent paradox: the residuals of the FP correlate strongly with SSP Υ_* and the best predictor of Υ_* is surface mass density, yet surface mass density itself shows no correlation with the FP residuals (§4.4, Fig. 13a). As we will see, the solution to this apparent contradiction is that the intrinsic scatter of the FP is partly due to the intrinsic scatter of the Υ_* – Σ_{vir} relation, i.e. to the relatively broad range of Υ_* at fixed σ_e and R_e (0.14 dex), resulting in a broad distribution of Υ_* at any position on the FP.

4.6 The FP fully encapsulates the Υ_* – Σ_{vir} relation

To understand the origin of the correlation between the FP residuals $\Delta \log L$ and Υ_* , we study the relation between $\Delta \log L$ and the residuals of the Υ_* – Σ_{vir} relation, $\Delta \log \Upsilon_*(\Sigma_{\text{vir}})$, as shown in Fig. 16.

The negative correlation in Fig. 16 means that, at fixed σ_e and R_e (and so at any fixed position on the FP), galaxies lying above the Υ_* – Σ_{vir} relation ($\Delta \log \Upsilon_*(\Sigma_{\text{vir}}) > 0$) lie preferentially below the FP ($\Delta \log L < 0$). The same is true if replacing Υ_* with SSP age. This result has a straightforward interpretation: at any fixed position on the FP, galaxies lying above the Υ_* – Σ_{vir} (or age– Σ_{vir}) relation have higher stellar mass-to-light ratio and are thus less luminous compared to the average galaxy at that position. The fact that the FP residuals do not correlate with Σ_{vir} is because the FP already encapsulates the mean Υ_* variation along the Υ_* – Σ_{vir} relation, so Σ_{vir} does not contain any additional information that can reduce the FP scatter. The Υ_* – Σ_{vir} relation is embedded in the FP through (part of) the FP tilt (the deviation of the best-fit FP parameters from the virial values to the observed values). It remains to be de-

termined how much of the observed tilt is explained by the Υ_* – Σ_{vir} relation.

Contrary to expectations, repeating the test of Fig. 16 with the residuals of the best-fit Υ_* – M_{vir} and Υ_* – Φ_{vir} relations gives results that are statistically consistent with Fig. 16. This lack of difference could be due to the large uncertainty in both $\Delta \log \Upsilon_*(\Sigma_{\text{vir}})$ and $\Delta \log L$, but to test this hypothesis we need a larger ETG sample. Here we assume that, in accordance with the results of § 4.5, the Υ_* – Σ_{vir} is the most fundamental of the three relations.

4.7 Mock Fundamental Planes

Having determined the dependence of Υ_* on the structural parameters σ_e and R_e , we now investigate the effect of the Υ_* – Σ_{vir} relation on the FP tilt and scatter. We do so by studying two mock FPs, to test (i) if using Υ_* inferred from the Υ_* – Σ_{vir} relation affects the mock FP in the same way as using the measured Υ_* and (ii) to quantify the impact of systematic trends of Υ_* with σ_e and R_e on the FP tilt and scatter.

We create two mock datasets by taking for each FP galaxy its measured σ_e and R_e but replacing observed L with a synthetic luminosity, calculated as $L_{\text{synth}} \equiv M_{\text{vir}}/\Upsilon_*$. The two mock datasets differ only in how Υ_* , and so synthetic luminosity, is obtained. With our definition of M_{vir} , setting $\Upsilon_* = 1$ yields the virial plane ($a = 2.000 \pm 0.017$ and $b = 1.000 \pm 0.012$). Because we use the measured (or inferred) value of Υ_* , the mock planes measure how much of the FP tilt relative to the virial plane is due to systematic variations of Υ_* with σ_e and R_e , and how much of the FP scatter is due to the scatter in Υ_* .

For the first mock (Fig. 17a), we take for each galaxy, alongside σ_e and R_e , the measured Υ_* . We then derive the synthetic luminosity $L_{\text{synth}}^{\Upsilon_*(\text{measured})}$ by substituting these values in the expression for $\log L$ (equation 2); i.e. $L_{\text{synth}}^{\Upsilon_*(\text{measured})} \equiv M_{\text{vir}}(\sigma_e, R_e)/\Upsilon_*$. Because we focus on how stellar-population properties affect the FP, we set the structural factor $\kappa = 5$ (following C06), the stellar mass fraction $f_* = 1$, and assume a Chabrier IMF for every galaxy ($\Upsilon_{\text{IMF}}/\Upsilon_* = 1$); the impact of these assumptions will be discussed in § 4.7.2. With these definitions, the ratio $L_{\text{synth}}^{\Upsilon_*(\text{measured})}/L$ leaves out the non-homology, dark-matter, and IMF terms of the FP (cf. equations 2 and 33).

For the second mock (Fig. 17b), we take for each galaxy only two measurements: σ_e and R_e . From these values, we calculate the dynamical surface mass density Σ_{vir} , then use the empirical relation (31) to infer the value of $\log \Upsilon_*$; we also add Gaussian random noise with standard deviation of 0.14, equal to the *rms* about the best-fit Υ_* – Σ_{vir} relation.⁶ For this second mock, the synthetic luminosity is then defined as $L_{\text{synth}}^{\Upsilon_*(\Sigma_{\text{vir}})} \equiv M_{\text{vir}}(\sigma_e, R_e)/\Upsilon_*[\Sigma_{\text{vir}}(\sigma_e, R_e)]$, where the mass-to-light ratio is given by the empirical relation equation (31).

Thus $L_{\text{synth}}^{\Upsilon_*(\text{measured})}$ is a function of three observables: σ_e , R_e and Υ_* , whereas $L_{\text{synth}}^{\Upsilon_*(\Sigma_{\text{vir}})}$ depends solely on σ_e and R_e .

⁶ For completeness, we also infer a mock age, by using the empirical relation between the measured $\log \text{age}$ and Σ_{vir} . This inferred age is used to colour-code Fig. 17b but has no role in the analysis.

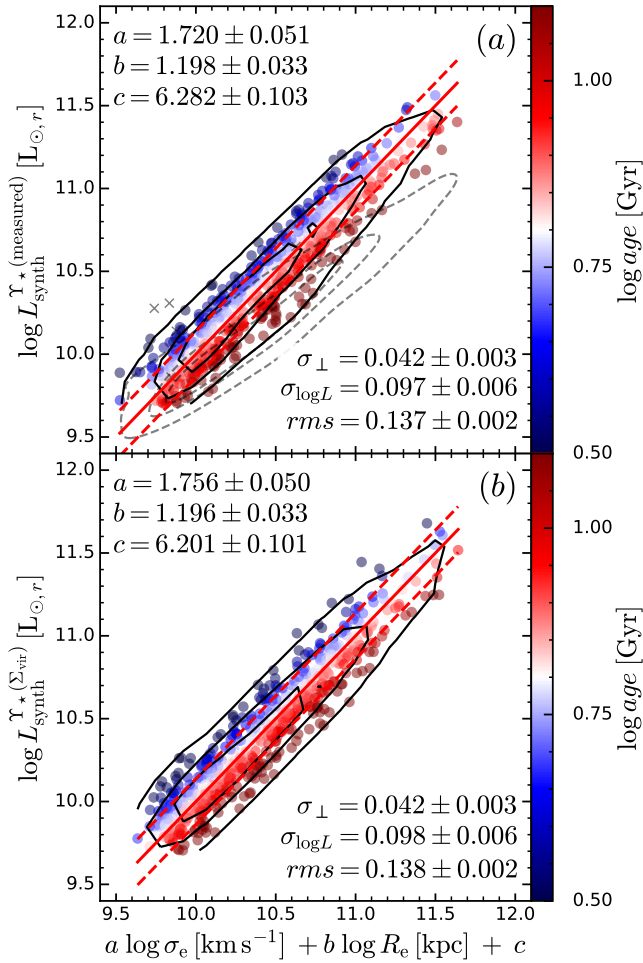


Figure 17. The mock FPs, showing that the systematic trends of SSP mass-to-light ratio across and through the plane are insufficient to explain all the tilt of the observed FP (compare the best-fit coefficients of the mock FPs with the FP coefficients in Fig. 9; the dashed contours show the projection of the fiducial FP, other symbols are the same as in Fig. 9). The synthetic luminosity is the virial mass divided by the SSP mass-to-light ratio, derived in turn either from the SSP age and metallicity measurements (panel a) or from Σ_{vir} (panel b) using equation (31). In both panels the best-fit FP coefficients differ from both the virial prediction and the fiducial FP, highlighting that the stellar-population relations are responsible for part, but not all, of the observed tilt.

4.7.1 Mock FP fit

The mock FPs are shown in Fig. 17, with the same symbols and colours as the fiducial FP (Fig. 9). For $L_{\text{synth}}^{\Upsilon_*(\Sigma_{\text{vir}})}$ we do not use any outlier rejection, because the data was generated from a Gaussian distribution with no outliers. The best-fit parameters of the two mock FPs are in excellent agreement with each other, implying that the empirical relation between Υ_* and Σ_{vir} (Fig. 17b) traces satisfactorily the systematic variations of measured Υ_* with σ_e and R_e (Fig. 17a). However, the mock FPs have different scatter and tilt from the fiducial FP, and therefore trends in Υ_* do not on their own explain the tilt and scatter of the FP.

For the observed scatter, we find that the mock FPs have $rms = 0.137 \pm 0.002$ dex (panel a) and 0.138 ± 0.002

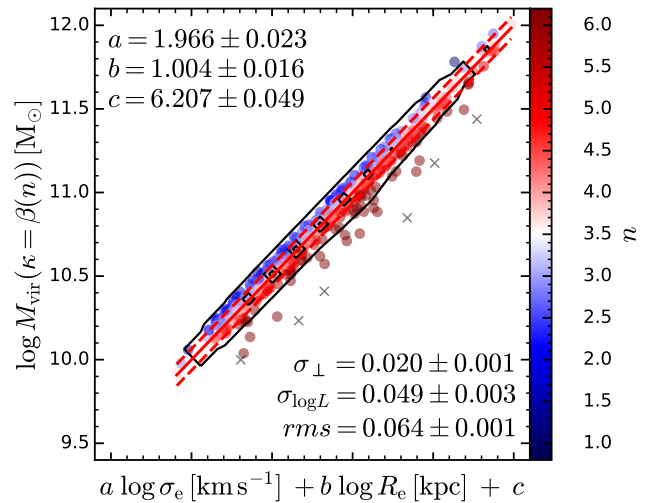


Figure 18. Edge-on view of the virial mass plane, showing the tilt and scatter due to the range of Sérsic index n at fixed σ_e and R_e . Both the tilt and scatter are less than that caused by stellar-population variations (cf. Fig 17a).

dex (panel b), whereas the fiducial FP has $rms = 0.104 \pm 0.001$ dex (Fig. 9). Despite appearances, these values are consistent. First, the mock plane has significantly steeper slope, which amplifies the ratio between the orthogonal scatter σ_{\perp} and the scatter along $\log L$; secondly, the measurement uncertainty in $\log L$ is significantly smaller than the uncertainty in L_{synth} , which contains a large contribution from the uncertainty in $\log \Upsilon_*$ (typically 0.05–0.1 dex; Gallazzi & Bell 2009). In fact, looking at the *intrinsic orthogonal scatter* (which does not suffer from amplification due to different tilts between the fiducial FP and the mock plane), we find $\sigma_{\perp} = 0.042 \pm 0.003$ dex, smaller than, but comparable to, the scatter of the fiducial FP ($\sigma_{\perp} = 0.048 \pm 0.002$ dex). Subtracting these numbers in quadrature, the ‘missing’ scatter between the observed and mock FP is 0.023 ± 0.004 dex. This implies that, provided our measurement uncertainties are correctly estimated, *most ($\approx 75\%$) of the FP scatter is explained by stellar mass-to-light variations at fixed σ_e and R_e .*

For the FP tilt, we find opposite results in the directions of $\log \sigma_e$ and $\log R_e$. We recall that the tilt of the fiducial FP with respect to the virial plane is 0.706 along the direction of $\log \sigma_e$ and 0.088 along the direction of $\log R_e$ (§ 4.1). For $\log \sigma_e$, the best coefficients of the mock FPs are $a = 1.720 \pm 0.051$ and $a = 1.756 \pm 0.050$, intermediate between the virial coefficient $a = 2$ and the fiducial coefficient $a = 1.294 \pm 0.039$. Along $\log \sigma_e$, the systematic variation of Υ_* with σ_e and R_e tilts the virial plane by 0.280 (panel a) or 0.244 (panel b); even though stellar Υ_* rotates the virial plane in the right direction (i.e. closer to the observed FP), the magnitude of this effect is insufficient to account for the observed tilt ($\approx 35\text{--}40\%$). In contrast, in the direction of $\log R_e$, we find $b = 1.198 \pm 0.033$ and $b = 1.196 \pm 0.033$, larger than both the fiducial coefficient $b = 0.912 \pm 0.025$ and the virial prediction $b = 1$; thus the SSP relations on their own tilt the mock FP *away* from the observed FP.

4.7.2 ‘Missing’ tilt and scatter

We now address the question about the ‘missing’ tilt and scatter, i.e. the difference between the fiducial and mock FPs. To do so, we consider the ratio of the dynamical mass to the mass derived from the product of the luminosity and the mass-to-light ratio

$$\frac{M_{\text{vir}}(\kappa = 5)}{L \Upsilon_{\star}} = \frac{5}{\kappa} \cdot \frac{\Upsilon_{\text{IMF}}}{\Upsilon_{\star}} \cdot \frac{1}{f_{\star}} = \frac{L_{\text{synth}}^{\Upsilon_{\star}(\text{measured})}}{L} \quad (33)$$

where the equality is derived from equations 1 & 2 and $L_{\text{synth}}^{\Upsilon_{\star}(\text{measured})}$ is the quantity used in the mock FP, Fig. 17a. Note that this mass ratio can also be viewed as the ratio of two mass-to-light ratios, one obtained from the observed virial mass and the observed luminosity and the other from the stellar population model; dividing M_{vir}/L by Υ_{\star} removes the effect of measured SSP trends.

The expression on the right of equation (33) can be calculated from the observed values of σ_e , R_e , L and Υ_{\star} . Modelling this quantity as a 3-d Gaussian as a function of σ_e and R_e , we find the coefficients to be

$$\log \frac{\Upsilon_{\text{IMF}}/\Upsilon_{\star}}{\kappa f_{\star}} = (0.561 \pm 0.076) \log \sigma_e \\ + (0.310 \pm 0.041) \log R_e - (1.082 \pm 0.150) \quad (34)$$

The ratio between the coefficients of $\log R_e$ and $\log \sigma_e$ is $b/a = 0.55 \pm 0.14$, consistent with the value expected from a correlation with dynamical mass (in agreement with the findings of Graves & Faber 2010). A correlation with σ_e only is unlikely ($P < 10^{-4}$, with b/a almost 4 standard deviations from 0). Equation 34 also highlights that *both* σ_e and R_e play a role in the structural and/or IMF trends *along* the FP. Note, however, that the stellar mass fraction varies significantly with radius, so an additional structural difference could be due to the overall stellar mass fraction.

To isolate the contribution of structural non-homology to the FP tilt and scatter, we study $M_{\text{vir}}(\kappa = \beta(n))$, where

$$\beta(n) = 8.87 - 0.831 n + 0.0241 n^2 \quad (35)$$

(C06, their equation 20). We use MGE R_e with Sérsic-based $\kappa = \beta(n)$ precisely to isolate the effect of non-homology, as captured by Sérsic index n : for Sérsic mass (and light) profiles, using $\beta(n)$ yields accurate dynamical masses based on the Sérsic virial estimator, so using Sérsic R_e in the definition of $M_{\text{vir}}(\kappa = \beta(n))$ would remove the effect of non-homology from the FP tilt.

This model of the mass plane gives

$$\log M_{\text{vir}}(\kappa = \beta(n)) = (1.966 \pm 0.023) \log \sigma_e \\ + (1.004 \pm 0.016) \log R_e + (6.207 \pm 0.049) \quad (36)$$

with a scatter $rms = 0.064 \pm 0.001$ dex (see Fig. 18). At face value, the intrinsic scatter due to n -based non-homology is only $\sigma_{\perp} = 0.020 \pm 0.001$ dex, much smaller than we inferred for the SSP-induced scatter ($\sigma_{\perp} = 0.042$ dex, Fig. 17a), and contributing only 17% of the fiducial FP scatter ($\sigma_{\perp} = 0.048 \pm 0.002$ dex, Fig. 17a). Intriguingly, this scatter is of the order of the ‘missing’ scatter after considering the contribution of stellar populations ($\sigma = 0.023 \pm 0.004$ dex, § 4.7.1). Clearly, this scatter is degenerate with the measurement uncertainties on $\beta(n)$: if we over-estimated these uncertainties, the contribution of n to the FP scatter would be under-estimated. The issue, however, is that even the

observed rms is not very large to begin with; for the true intrinsic scatter in Fig. 18 to be the same as we infer for SSP variations, the observed rms in Fig. 18 must be ≈ 0.1 dex. To make matters worse, we assumed uncertainties of order 6% on n , but this value is likely under-estimated for high-index galaxies (§ 2.5), i.e. for precisely the same galaxies that dominate the scatter in Fig. 36. Therefore we conclude that non-homology, as measured by Sérsic index, does not contribute significantly to the FP scatter, with a conservative estimate of $\approx 20\%$. Simply put: the variation of n at fixed σ_e and R_e is too little to cause significant scatter in the FP.

As for the tilt, we also find a very small deviation between the fit to the model in Fig. 18 and the virial plane. Alternatively, if the measurement uncertainties on n were severely underestimated, the effect of systematic trends of n with σ_e and R_e could be damped, thereby masking the effect of non-homology in Fig. 18. In this case, however, the rms and the induced scatter on the FP would be over-estimated. Note that there is a degeneracy between the tilt and scatter: if our uncertainties were severely under-estimated, then the effect of n on the FP tilt would also be under-estimated, but the effect on the FP scatter would be over-estimated. One way to reconcile large scatter in both non-homology and Υ_{\star} is for n and Υ_{\star} to be correlated at fixed σ_e and, possibly, R_e . Our data, however, offers no evidence of such a correlation.

Finally, we remark that, after considering both SSP variations and non-homology, there is no space left for *independent* scatter in f_{\star} and $\Upsilon_{\text{IMF}}/\Upsilon_{\star}$, thus requiring that these two properties (anti)correlate with Υ_{\star} and/or n and/or each other.

5 DISCUSSION

5.1 The SAMI fiducial Fundamental Plane

In § 4.1 we presented the fiducial FP for a volume- and luminosity-limited sample ($z \leq 0.065$ and $L_r \geq 10^{9.7} L_{r,\odot}$) of early-type galaxies drawn from the SAMI Survey. The best-fit values of the FP coefficients ($a = 1.294 \pm 0.039$ and $b = 0.912 \pm 0.025$) are only in marginal agreement with the results from ATLAS^{3D} ($b = 1.249 \pm 0.044$ and $c = 0.964 \pm 0.03$ C13, top panel of their fig.12; notice their different definition of the FP coefficients: our (a, b, c) correspond to their (b, c, a)). We repeat our analysis with a volume- and mass-limited sample with $M_{\star} \geq 6 \times 10^9 M_{\odot}$ and $z < 0.05$ (roughly equivalent to the ATLAS^{3D} selection criterion $M_K < -21$ mag; Cappellari et al. 2011). With this sample, and using the same algorithm as C13, we find $a = 1.260 \pm 0.048$ and $b = 0.931 \pm 0.032$, and an observed rms of 0.098 ± 0.005 dex (ATLAS^{3D} has 0.1 dex). Our fiducial FP is thus in excellent agreement with the ATLAS^{3D} FP once we account for the different algorithm and sample selection.

When using σ_e , the SAMI Pilot Survey found $\alpha = 0.79 \pm 0.07$ and $\beta = 0.96 \pm 0.05$ (Scott et al. 2015, their Table 2, where they define $\alpha \equiv a$ and $\beta \equiv b$). These best-fit values differ from ours, but the sample selection criteria also differ. We repeat our FP fit using the same algorithm as Scott et al. (2015) and with an equivalent sample selection (i.e. $\log L > 10^{10.2} L_{\odot,r}$, only considering galaxies in the clusters

Abell 85, Abell 168 and Abell 2399), and find $a = 0.85 \pm 0.11$ and $b = 0.92 \pm 0.08$, in agreement with [Scott et al. \(2015\)](#); our larger uncertainties are estimated from bootstrapping the sample one hundred times.

From these comparisons, we conclude that the best-fit FP coefficients depend not only on the model used (cf. § 4.1.2), but also on the properties of the sample considered. These dependencies likely arise from inadequate models. For example, it is well-known that the galaxy luminosity function is well-fit by a Schechter function, and that the FP intrinsic scatter decreases with luminosity ([Hyde & Bernardi 2009](#)). In addition, the plane model itself might only be an approximation: there is evidence that the logarithm of the dynamical mass-to-light ratio is a quadratic function of $\log \sigma_e$ ([Zaritsky et al. 2006](#); [Wolf et al. 2010](#)). By inserting this quadratic relation in the virial equation, [Zaritsky et al. \(2006\)](#) obtain a slanted parabolic cylinder (the ‘fundamental manifold of spheroids’). This surface is well approximated by a plane, given our range in σ_e and our measurement uncertainties ([Scott et al. 2015](#)). However, different samples give different weights to their region on the manifold, and thus may yield different plane approximations. Moreover, if we consider the FP as the projection of a higher dimensional hyperplane involving age, then it is not surprising that different samples, which have in general different age distributions, might give rise to different projections.

It is worth clarifying that the trends we report between the FP residuals and σ_e and R_e are not evidence for the non-linear nature of the galaxy manifold. First, the residuals between a non-linear manifold and a linear model would be non-linear, but we see no evidence of non-linearity in [Figs 12a–c](#). Secondly, the trend between $\Delta \log L$ and σ_e is opposite to expectations: if one recasts the expression of the galaxy manifold from [Zaritsky et al. \(2006\)](#) in terms of $\log L$, the result is a concave function of $\log \sigma_e$. Comparing this function to its linear approximation for the range of σ_e of our sample, we obtain a positive trend between the residuals and $\log \sigma_e$, contrary to our findings. In order to study the non-linearity of the FP, it would be best to extend the baseline in σ_e , including a significant fraction of quiescent dwarf galaxies ($\sigma \lesssim 30 \text{ km s}^{-1}$, which might prove challenging without using adequate spectral resolution, e.g. [Barat et al. 2019, 2020](#), [Scott et al. 2020](#), [Eftekhari in prep.](#)).

5.2 Residual trends with structural and stellar-population parameters

In § 4.3 and § 4.4 we have studied the relation between the residuals of the FP and various structural and stellar-population observables. We concluded that SSP age is the strongest driver of the intrinsic FP scatter, with a significance greater than eight standard deviations. This result is independent of sample selection criteria: it persists (and becomes stronger) if we drop our volume-limited requirement, if we include early-type spirals, and if we select red galaxies regardless of their visual morphology. It persists (and becomes weaker) if we select only elliptical galaxies, although the sample size is smaller than the ETG sample.

The trend between $\Delta \log L$ and age also exists at fixed σ_e , so it is not a consequence of the correlation between age and σ_e or the anticorrelation between σ_e and $\Delta \log L$. Moreover, the trend persists and remains the most signifi-

cant even if we swap the 3dG algorithm for the LTS algorithm, which gives no correlation between $\Delta \log L$ and σ_e ([Appendix C](#), [Figs C1 and C4](#)). The trend disappears only for the oldest galaxies, probably because of a combination of physical and practical reasons: for old SSP ages, the effect of age on Υ_* flattens out and the ages themselves have large uncertainties.

The existence of a trend between the residuals of the FP and SSP age has long been known ([Forbes et al. 1998](#)). Here we demonstrate that this trend is the most significant physical trend, regardless of a number of assumptions about the sample, outliers, aperture size, photometry, uncertainties and optimisation. In addition, we connect the trend between age and $\Delta \log L$ to the empirical relation between surface mass density and age: among the observables based on galaxy mass and size, surface mass density is known to be the best predictor of both SSP age ([B18](#)) and light-weighted, full-spectral-fitting age ([Barone et al. 2020](#)). Here we show the logical consequence, that surface mass density is also the best predictor of SSP mass-to-light ratio Υ_* (§4.5). Given that the FP residuals strongly correlate with SSP age (and Υ_*) but do not correlate with surface mass density, we conclude that: (i) the FP fully captures the mean age (and Υ_*) variation with Σ_{vir} and (ii) the scatter about the Σ_{vir} -age relation is propagated to the FP. In particular, we argue that most ($\approx 75\%$) of the FP scatter is due to the broad distribution in SSP age at fixed Σ_{vir} (we find an *rms* of 0.17 dex; for Υ_* , the *rms* is 0.14 dex; [Fig. 15c](#)). The large, size-dependent scatter of age as a function of stellar mass is already in place at $z \approx 1$, and is thought to arise from different evolutionary paths to quiescence leaving different structural signatures on the structure of galaxies ([Wu et al. 2018](#); [D'Eugenio et al. 2020](#)). Alternatively, the relation could be a consequence of surface mass density being related to the cosmic epoch when the galaxy became quiescent ([van der Wel et al., in prep.](#); [Barone et al, in prep.](#)).

If the trend across the plane is due to stellar age, where do still younger galaxies lie, relative to the fiducial FP? In [Fig. 19](#) we overlay 512 SAMI early spirals on the fiducial ETG FP. Each galaxy is colour-coded according to its LOESS-smoothed age; the colours are different from [Fig. 9](#), as here they are mapped to the interval $\mu(\text{age}) \pm \sigma(\text{age})$, where μ and σ are the median and standard deviation of the early-spiral age distribution). Notice that, despite their different properties (including ongoing star formation and, presumably, larger dark matter fractions), early spirals lie remarkably close to the fiducial FP. These galaxies have younger median ages compared to ETG sample (3.5 Gyr compared to 6.4 Gyr), yet their offset from the ETG FP is remarkably small (only 0.03 dex). This surprising result could be due to the competing effects of early spirals having lower median stellar mass-to-light ratios but higher dark matter and/or dust fractions than ETGs, and will be investigated in a future paper. However, it underscores the potential for expanding to broader morphological samples the use of the FP and other scaling relations as distance indicators (e.g. [Barat et al. 2019, 2020](#)).

We argued that the correlation between the FP residuals and SSP metallicity is not physical, but rather an outcome of the age-metallicity degeneracy. On the other hand, we found a significant correlation with SSP $[\alpha/\text{Fe}]$ ([Fig. 14c](#)), with evidence that this correlation also holds at fixed SSP

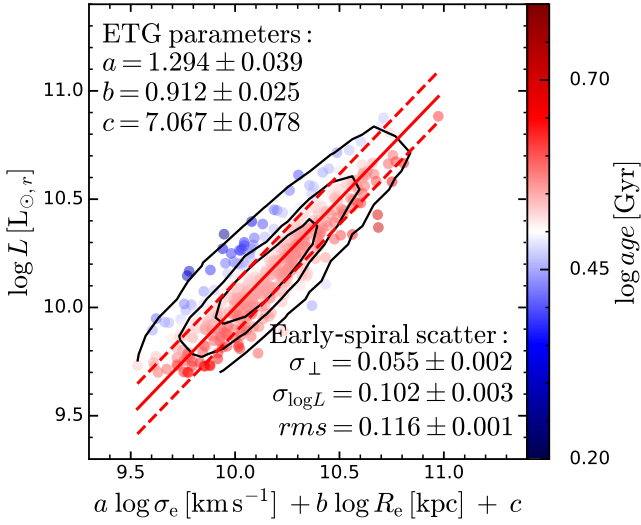


Figure 19. Location of the SAMI early spirals relative to the fiducial FP of ETGs. Circles represent early spirals ($1 < \text{mtype} \leq 2$, § 2.5), colour-coded with LOESS-smoothed stellar age (the colours are mapped to the interval enclosing $\approx 68\%$ of the stellar age histogram). The red lines represent the fiducial FP of ETGs, with the best-fit parameters reported in the top left corner. The distribution of ETGs is represented by the solid black contours, enclosing the 90th, 67th and 30th percentiles of the ETG sample. The scatter reported in the bottom-right corner is the scatter of early spirals with respect to the fiducial FP. Early spirals fall very close to the fiducial FP (the median offset is just 0.03 dex) and maintain the trend of increasing age across the FP.

age. We checked that this correlation does not depend either on global (cluster vs field/group) nor local environment (as measured by the density of nearby galaxies), and so it is unlikely to be related to the observed correlation between $[\alpha/\text{Fe}]$ and cluster-centric distance (which is observed for galaxies that are ~ 10 times less massive than considered here, Liu et al. 2016). A possible explanation is offered by downsizing, i.e. the oldest galaxies forming most rapidly (Cowie et al. 1996; Thomas et al. 2005; Graves et al. 2007). Downsizing implies a positive correlation between age and $[\alpha/\text{Fe}]$, as higher $[\alpha/\text{Fe}]$ corresponds to shorter duration of star formation. Because the age of the oldest stellar populations is difficult to measure, $[\alpha/\text{Fe}]$ may contain additional (or at least independent) age information that is not captured by the indicators used to measure SSP age itself. Another possibility is that $[\alpha/\text{Fe}]$ could be related to the distribution of matter inside $1R_e$.

An important caveat is that all our stellar-population properties are luminosity-weighted SSP equivalents, whereas real stellar populations have a finite distribution of ages, metallicities and abundances, reflecting complex star-formation histories.

Among the structural parameters, the FP residuals correlate most strongly with Sérsic index n and galaxy projected shape ϵ_e , but neither is as significant as the trends with SSP properties. For ϵ_e , the correlation probably results from the superposition of three effects. The first effect is that high- ϵ_e galaxies are oblate discs observed close to edge-on and are therefore expected to be rotation-supported and to have higher observed σ_e than their face-on analogues. The second effect is that if any dust was present, it would increase

the observed mass-to-light ratio. These two effects would make these galaxies under-luminous at their location on the FP, inducing a negative trend between the FP residuals and ϵ_e , the opposite of what is seen. On the other hand, a third effect is that these disc-like ETGs have younger SSP ages than spheroidal ETGs (e.g. van de Sande et al. 2018), but the latter cannot project to high ϵ_e , thus creating an anticorrelation between observed ϵ_e and age that makes flattened ETGs younger and therefore more luminous than average at their location on the FP. The net effect of these three effects in our sample is a weak positive correlation with apparent shape; however, different samples, with a different ratio of slow- to fast-rotators, may have different residual trends (e.g. Bernardi et al. 2020). This hypothesis can be tested using dynamical models to infer the intrinsic shape.

Our results suggest that structural trends due to non-homology are not an important driver of the FP scatter (Figs 10 and 13c), which is at variance with some other works (Prugniel & Simien 1997; Desmond & Wechsler 2017), but in agreement with the results from both dynamical modelling (C06) and strong lensing (Bolton et al. 2007, 2008; Koopmans et al. 2009), as well as from stability considerations (e.g. Nipoti et al. 2002). It is important to recall, however, that although it seems unlikely, it is still possible that large measurement uncertainties on the structural observables prevent us from observing stronger trends with the FP residuals. More importantly, given the strong dependence of the FP parameters on the properties of the sample, we cannot exclude that structural trends would be present with a different sample, for example by including a larger proportion of massive galaxies than in our volume-limited sample. The fact that non-homology has little impact on the FP scatter has no bearing to the FP tilt.

5.3 Fundamental Plane tilt

We have seen that the relation between the stellar-population Υ_* and Σ_{vir} (equations 31 and 32) accounts for approximately 50% of the FP tilt in $\log \sigma_e$. However, in $\log R_e$, stellar-population effects tilt the FP away from the observed plane. This result is a direct consequence of the fact that SSP age and Υ_* follow Σ_{vir} , which is a decreasing function of R_e ($\Sigma_{\text{vir}} \propto \sigma_e^2/R_e$). Given that non-homology (as captured by Sérsic index n) seems to have little effect on the FP tilt (§ 4.7.2), after accounting for stellar-population effects the remaining FP tilt in $\log \sigma_e$ (50%) and $\log R_e$ (250%) must be due to a combination of systematic variations in the stellar-to-total mass fraction (f_*) and/or the IMF shape relative to our Chabrier assumption (parameterised as $\Upsilon_{\text{IMF}}/\Upsilon_*$).

There is considerable evidence in the literature that SSP variations account for roughly half of the FP tilt (e.g. Pahre et al. 1995, 1998; Prugniel & Simien 1997; Gallazzi et al. 2005; Hyde & Bernardi 2009). Graves & Faber (2010) also reached this conclusion, and added that the FP tilt is due to two contributions: SSP trends tilt the FP only in the $\log \sigma_e$ direction, whereas dark matter/IMF trends tilt the FP along a direction that is proportional to $\log M_{\text{vir}}$. In contrast with their findings, we conclude that both the measured SSP trends and the ‘missing contribution’ tilt the FP along both $\log \sigma_e$ and $\log R_e$. The origin of this disagreement is difficult to disentangle, because their result is based on stacking in-

dividual single-fibre galaxy spectra and they use a different sample and optimisation, so a fair comparison is particularly challenging.

To further constrain the terms f_* and $\Upsilon_{\text{IMF}}/\Upsilon_*$ in the FP equation (2) requires dynamical models, a subject for future work.

5.4 Fundamental Plane scatter

The observed scatter about the fiducial FP is 0.104 ± 0.001 dex. With our estimate of the observational uncertainties, the intrinsic scatter is $\sigma_{\perp} = 0.048 \pm 0.002$ dex. Given the observed correlation between the FP residuals and stellar population age, we expect part of this scatter to contain information about the stellar population age, an expectation that is confirmed by the strong correlation between the FP residuals and the residuals of the $\Upsilon_* - \Sigma_{\text{vir}}$ relation.

In § 4.7.1 we used stellar population Υ_* to create a mock FP, and find an intrinsic scatter $\sigma_z = 0.042 \pm 0.003$ dex. Thus, with our estimate of the observational uncertainties, stellar population trends seem to account for most ($\approx 75\%$) of the FP scatter (in quadrature).

On the other hand, non-homology (as parameterised by Sérsic index n) seems to account for $\approx 20\%$ of the FP scatter (Fig. 18); at fixed σ_e and R_e , the range in n is not broad enough to significantly affect the FP.

Together, Υ_* and n account for most of the FP scatter, leaving little space for any scatter in the rest of the FP equation (2), i.e. dark-matter fraction $1 - f_*$ and IMF trends $\Upsilon_{\text{IMF}}/\Upsilon_*$. This may point either to the under-estimation of the uncertainties on Υ_* and/or n or to the existence of physical correlations between these galaxy properties that reduce their impact on the FP scatter.

Dust could in principle reduce the FP scatter. At fixed σ_e and R_e , the youngest galaxies have the lowest Υ_* and so the largest positive deviations above the plane. If these galaxies also had the largest dust fractions, dust attenuation would reduce the deviation and hence the scatter. In practice this effect amounts to $rms = 0.01\text{--}0.02$ dex and is therefore negligible for the sample considered here (Appendix D).

If SSP trends contribute a non-negligible fraction of the FP intrinsic scatter, it should then be possible to use information encoded in SSP properties to reduce this scatter, provided that the uncertainties in the SSP measurements do not overwhelm the potential gains (as is presently the case with SSP age).

6 SUMMARY AND CONCLUSIONS

In this work, we used a volume- and mass-limited sample of morphologically-selected early-type galaxies from the SAMI Galaxy Survey to study the impact of systematic trends of stellar population parameters and non-homology on the tilt and scatter of the Fundamental Plane (FP). Our key advantage is the combination of high-quality aperture spectra with a carefully selected sample and sophisticated analysis techniques, which yields both accurate and representative results.

Once the sample selection criteria are taken into account, the parameters of our fiducial FP (Table 3) are consistent with previous works. We find that:

(i) The FP scatter is dominated by stellar population effects: among the structural properties considered, only Sérsic index anticorrelates with the FP residuals (four standard deviations, § 4.3 and Table 4). In contrast, stellar age, r -band mass-to-light ratio and α -element abundance all have statistically significant anticorrelations with the FP residuals (eight standard deviations, § 4.4 and Table 4).

(ii) Our results are qualitatively unchanged if we alter a range of assumptions: sample selection (volume- and mass-limited vs no limits; ellipticals only vs early-types), outliers rejection, aperture size and shape, adopted photometry, measurement uncertainties and correlated noise, or model and algorithm used (3-d Gaussian vs least-trimmed squares, Table 3).

(iii) In agreement with previous works, we find that the relation between stellar mass-to-light ratio Υ_* and surface mass density Σ_{vir} is tighter than the relation between Υ_* and either virial mass or gravitational potential ($\Upsilon_* - \Sigma_{\text{vir}}$ relation, § 4.5).

(iv) We find a strong anticorrelation between the residuals of the $\Upsilon_* - \Sigma_{\text{vir}}$ relation and the FP residuals. The strong correlation between the FP residuals and Υ_* (and stellar age) is due to the large intrinsic scatter in the $\Upsilon_* - \Sigma_{\text{vir}}$ (and age- Σ_{vir}) relations (§ 4.6).

(v) For fixed IMF, stellar-population relations account for approximately 75% of the FP scatter, whereas non-homology accounts for approximately 20% (§ 4.7).

(vi) For fixed IMF, stellar-population relations do not fully explain the FP tilt. In fact, in the direction of $\log R_e$, the stellar-population relations tilt the virial plane in the wrong direction with respect to the observed FP (§ 4.7). Given the properties of our sample, non-homology appears to have a negligible effect on the FP tilt.

(vii) The remaining FP tilt not explained by stellar populations or non-homology is presumably due to varying dark-matter fractions and systematic trends in IMF shape; this tilt is roughly proportional to virial mass.

ACKNOWLEDGEMENTS

We thank the referee for their constructive report, which improved the quality of this manuscript. We also thank Michele Cappellari for his comments and suggestions on the fitting algorithms and Elena Dalla Bontà for her suggestions. FDE acknowledges funding through the H2020 ERC Consolidator Grant 683184, and by the Australian Research Council Centre of Excellence for All-sky Astrophysics (CAASTRO; grant CE110001020). NS acknowledges support of an Australian Research Council Discovery Early Career Research Award (project number DE190100375) funded by the Australian Government. This research was supported by the Australian Research Council Centre of Excellence for All-sky Astrophysics (CAASTRO), through project number CE110001020, and by the Australian Research Council Centre of Excellence for All-sky Astrophysics in 3 Dimensions (ASTRO 3D), through project number CE170100013. RLD acknowledges travel and computer grants from Christ Church, Oxford and support from the Oxford Hintze Centre for Astrophysical Surveys which is funded by the Hintze Family Charitable Foundation. RLD was also supported by the Science & Technology Facilities Council grant num-

bers ST/H002456/1, ST/K00106X/1 and ST/J 002216/1. JvdS acknowledges support of an Australian Research Council Discovery Early Career Research Award (project number DE200100461) funded by the Australian Government. SB acknowledges funding support from the Australian Research Council through a Future Fellowship (FT140101166). JBH is supported by an ARC Laureate Fellowship that funds Jesse van de Sande and an ARC Federation Fellowship that funded the SAMI prototype. JJB acknowledges support of an Australian Research Council Future Fellowship (FT180100231). MSO acknowledges the funding support from the Australian Research Council through a Future Fellowship (FT140100255).

The SAMI Galaxy Survey is based on observations made at the Anglo-Australian Telescope. The Sydney-AAO Multi-object Integral-field spectrograph (SAMI) was developed jointly by the University of Sydney and the Australian Astronomical Observatory, and funded by ARC grants FF0776384 (Bland-Hawthorn) and LE130100198. The SAMI input catalog is based on data taken from the Sloan Digital Sky Survey, the GAMA Survey and the VST ATLAS Survey. The SAMI Galaxy Survey is funded by the Australian Research Council Centre of Excellence for All-sky Astrophysics (CAASTRO), through project number CE110001020, and other participating institutions. The SAMI Galaxy Survey website is <http://sami-survey.org/>.

Funding for SDSS-III has been provided by the Alfred P. Sloan Foundation, the Participating Institutions, the National Science Foundation, and the U.S. Department of Energy Office of Science. The SDSS-III web site is <http://www.sdss3.org/>.

GAMA is a joint European-Australasian project based around a spectroscopic campaign using the Anglo-Australian Telescope. The GAMA input catalogue is based on data taken from the Sloan Digital Sky Survey and the UKIRT Infrared Deep Sky Survey. Complementary imaging of the GAMA regions is being obtained by a number of independent survey programmes including GALEX MIS, VST KiDS, VISTA VIKING, WISE, Herschel-ATLAS, GMRT and ASKAP providing UV to radio coverage. GAMA is funded by the STFC (UK), the ARC (Australia), the AAO, and the participating institutions. The GAMA website is <http://www.gama-survey.org/>.

Based on observations made with ESO Telescopes at the La Silla Paranal Observatory under programme ID 179.A-2004.

This work made extensive use of the freely available Debian GNU/Linux operative system. We used the Python programming language (van Rossum 1995), maintained and distributed by the Python Software Foundation. We further acknowledge the use of NUMPY (Harris et al. 2020), SCIPY (Jones et al. 2001), MATPLOTLIB (Hunter 2007), EMCEE (Foreman-Mackey et al. 2013), CORNER (Foreman-Mackey 2016), ASTROPY (Astropy Collaboration et al. 2013), PATHOS (McKerns et al. 2011), MGEFIT Cappellari (2002), LTSFIT (C13), LOESS (Cappellari et al. 2013b), DYNESTY (Speagle 2020) and SEXTRACTOR (Bertin & Arnouts 1996).

During the preliminary analysis we have made extensive use of TOPCAT (Taylor 2005).

DATA AVAILABILITY

The data used in this work is available in the public domain, through the SAMI Data Release 3 (Croom et al. 2021). Ancillary data comes from the GAMA Data Release 3 (Baldry et al. 2018) and raw data is from SDSS DR7 (Abazajian et al. 2009), SDSS DR9 (Ahn et al. 2012) and VST (Shanks et al. 2013, 2015).

Regularised MGE fits and the 3dG software can be obtained [contacting the corresponding author](#).

References

- Abazajian K. N., et al., 2009, *ApJS*, **182**, 543
 Abolfathi B., et al., 2018, *ApJS*, **235**, 42
 Ahn C. P., et al., 2012, *ApJS*, **203**, 21
 Allen J. T., et al., 2015, *MNRAS*, **446**, 1567
 Astropy Collaboration et al., 2013, *A&A*, **558**, A33
 Baldry I. K., et al., 2012, *MNRAS*, **421**, 621
 Baldry I. K., et al., 2018, *MNRAS*, **474**, 3875
 Barat D., et al., 2019, *MNRAS*, **487**, 2924
 Barat D., D’Eugenio F., Colless M., Sweet S. M., Groves B., Cortese L., 2020, *MNRAS*,
 Barone T. M., et al., 2018, *ApJ*, **856**, 64
 Barone T. M., D’Eugenio F., Colless M., Scott N., 2020, *ApJ*, **898**, 62
 Bender R., Burstein D., Faber S. M., 1992, *ApJ*, **399**, 462
 Bernardi M., et al., 2003, *AJ*, **125**, 1866
 Bernardi M., Domínguez Sánchez H., Margalef-Bentabol B., Nikakhtar F., Sheth R. K., 2020, *MNRAS*, **494**, 5148
 Bertin E., 2011, in Evans I. N., Accomazzi A., Mink D. J., Rots A. H., eds, *Astronomical Society of the Pacific Conference Series Vol. 442, Astronomical Data Analysis Software and Systems XX*. p. 435
 Bertin E., Arnouts S., 1996, *A&AS*, **117**, 393
 Bertin G., Ciotti L., Del Principe M., 2002, *A&A*, **386**, 149
 Beutler F., et al., 2011, *Monthly Notices of the Royal Astronomical Society*, **416**, 3017
 Bezanson R., Franx M., van Dokkum P. G., 2015, *ApJ*, **799**, 148
 Bland-Hawthorn J., et al., 2011, *Optics Express*, **19**, 2649
 Blanton M. R., Roweis S., 2007, *AJ*, **133**, 734
 Bolton A. S., Burles S., Treu T., Koopmans L. V. E., Moustakas L. A., 2007, *ApJ*, **665**, L105
 Bolton A. S., Treu T., Koopmans L. V. E., Gavazzi R., Moustakas L. A., Burles S., Schlegel D. J., Wayth R., 2008, *ApJ*, **684**, 248
 Brough S., et al., 2017, *ApJ*, **844**, 59
 Bryant J. J., Bland-Hawthorn J., Fogarty L. M. R., Lawrence J. S., Croom S. M., 2014, *MNRAS*, **438**, 869
 Bryant J. J., et al., 2015, *MNRAS*, **447**, 2857
 Bundy K., et al., 2015, *ApJ*, **798**, 7
 Cappellari M., 2002, *MNRAS*, **333**, 400
 Cappellari M., 2016, *ARA&A*, **54**, 597
 Cappellari M., 2017, *MNRAS*, **466**, 798
 Cappellari M., Emsellem E., 2004, *PASP*, **116**, 138
 Cappellari M., et al., 2006, *MNRAS*, **366**, 1126
 Cappellari M., et al., 2011, *MNRAS*, **413**, 813
 Cappellari M., et al., 2013a, *MNRAS*, **432**, 1709
 Cappellari M., et al., 2013b, *MNRAS*, **432**, 1862
 Carollo C. M., Danziger I. J., Buson L., 1993, *MNRAS*, **265**, 553
 Chabrier G., 2003, *PASP*, **115**, 763
 Cheung E., et al., 2012, *ApJ*, **760**, 131
 Chiu M.-C., Ko C.-M., Shu C., 2017, *Phys. Rev. D*, **95**, 063020
 Ciotti L., Lanzoni B., Renzini A., 1996, *MNRAS*, **282**, 1
 Colless M., Saglia R. P., Burstein D., Davies R. L., McMahan R. K., Wegner G., 2001, *MNRAS*, **321**, 277
 Conroy C., van Dokkum P. G., 2012, *ApJ*, **760**, 71

- Cortese L., et al., 2016, *MNRAS*, **463**, 170
- Cowie L. L., Songaila A., Hu E. M., Cohen J. G., 1996, *AJ*, **112**, 839
- Croom S. M., et al., 2012, *MNRAS*, **421**, 872
- Croom S. M., et al., 2021, *MNRAS*, **421**, 872
- D'Eugenio F., et al., 2020, *MNRAS*, **497**, 389
- Dalla Bontà E., Davies R. L., Houghton R. C. W., D'Eugenio F., Méndez-Abreu J., 2018, *MNRAS*, **474**, 339
- DeGroot M., 1970, *Optimal statistical decisions*. McGraw-Hill, New York, NY [u.a.]
- Desmond H., Wechsler R. H., 2017, *MNRAS*, **465**, 820
- Djorgovski S., Davis M., 1987, *ApJ*, **313**, 59
- Dressler A., Lynden-Bell D., Burstein D., Davies R. L., Faber S. M., Terlevich R., Wegner G., 1987, *ApJ*, **313**, 42
- Driver S. P., et al., 2011, *MNRAS*, **413**, 971
- Emsellem E., Monnet G., Bacon R., 1994, *A&A*, **285**, 723
- Emsellem E., et al., 2011, *MNRAS*, **414**, 888
- Falcón-Barroso J., Sánchez-Blázquez P., Vazdekis A., Ricciardelli E., Cardiel N., Cenarro A. J., Gorgas J., Peletier R. F., 2011, *A&A*, **532**, A95
- Fang J. J., Faber S. M., Koo D. C., Dekel A., 2013, *ApJ*, **776**, 63
- Feroz F., Hobson M. P., Bridges M., 2009, *MNRAS*, **398**, 1601
- Forbes D. A., Ponman T. J., Brown R. J. N., 1998, *ApJ*, **508**, L43
- Foreman-Mackey D., 2016, *The Journal of Open Source Software*, **1**, 24
- Foreman-Mackey D., Hogg D. W., Lang D., Goodman J., 2013, *PASP*, **125**, 306
- Gallazzi A., Bell E. F., 2009, *ApJS*, **185**, 253
- Gallazzi A., Charlot S., Brinchmann J., White S. D. M., Tremonti C. A., 2005, *MNRAS*, **362**, 41
- Gallazzi A., Charlot S., Brinchmann J., White S. D. M., 2006, *MNRAS*, **370**, 1106
- Ganda K., et al., 2007, *MNRAS*, **380**, 506
- Goodman J., Weare J., 2010, *Communications in Applied Mathematics and Computational Science*, **5**, 65
- Graham A., Colless M., 1997, *MNRAS*, **287**, 221
- Graves G. J., Faber S. M., 2010, *ApJ*, **717**, 803
- Graves G. J., Faber S. M., Schiavon R. P., Yan R., 2007, *ApJ*, **671**, 243
- Graves G. J., Faber S. M., Schiavon R. P., 2009, *ApJ*, **698**, 1590
- Green A. W., et al., 2018, *MNRAS*, **475**, 716
- Harris C. R., et al., 2020, *Nature*, **585**, 357
- Higson E., Handley W., Hobson M., Lasenby A., 2019, *Statistics and Computing*, **29**, 891
- Hill D. T., et al., 2011, *MNRAS*, **412**, 765
- Holden B. P., van der Wel A., Kelson D. D., Franx M., Illingworth G. D., 2010, *ApJ*, **724**, 714
- Hudson M. J., Smith R. J., Lucey J. R., Schlegel D. J., Davies R. L., 1999, *ApJ*, **512**, L79
- Hunter J. D., 2007, *Computing in Science and Engineering*, **9**, 90
- Hyde J. B., Bernardi M., 2009, *MNRAS*, **396**, 1171
- Johnson A., et al., 2014, *MNRAS*, **444**, 3926
- Jones E., Oliphant T., Peterson P., et al., 2001, *SciPy: Open source scientific tools for Python*, <http://www.scipy.org/>
- Jørgensen I., Franx M., Kjaergaard P., 1996, *MNRAS*, **280**, 167
- Kelly B. C., 2007, *ApJ*, **665**, 1489
- Kelvin L. S., et al., 2012, *MNRAS*, **421**, 1007
- Kelvin L. S., et al., 2014, *MNRAS*, **439**, 1245
- Kobayashi C., 2005, *MNRAS*, **361**, 1216
- Koopmans L. V. E., et al., 2009, *ApJ*, **703**, L51
- Krajinović D., et al., 2011, *MNRAS*, **414**, 2923
- Kroupa P., 2001, *MNRAS*, **322**, 231
- Liu Y., et al., 2016, *ApJ*, **818**, 179
- Loveday J., et al., 2012, *MNRAS*, **420**, 1239
- Magoulas C., et al., 2012, *MNRAS*, **427**, 245
- Maraston C., 2005, *MNRAS*, **362**, 799
- McDermid R. M., et al., 2015, *MNRAS*, **448**, 3484
- McKerns M. M., Strand L., Sullivan T., Fang A., Aivazis M. A. G., 2011, in *Proc. 10th Python in Sci. Conf. Texas*, p. 76 ([arXiv:1202.1056](https://arxiv.org/abs/1202.1056))
- Mehlert D., Thomas D., Saglia R. P., Bender R., Wegner G., 2003, *A&A*, **407**, 423
- Metropolis N., Rosenbluth A. W., Rosenbluth M. N., Teller A. H., Teller E., 1953, *J. Chem. Phys.*, **21**, 1087
- Mould J., 2020, *Frontiers in Astronomy and Space Sciences*, **7**, 21
- Nelan J. E., Smith R. J., Hudson M. J., Wegner G. A., Lucey J. R., Moore S. A. W., Quinney S. J., Suntzeff N. B., 2005, *ApJ*, **632**, 137
- Nipoti C., Londrillo P., Ciotti L., 2002, *MNRAS*, **332**, 901
- Oke J. B., Gunn J. E., 1983, *ApJ*, **266**, 713
- Oldham L. J., Houghton R. C. W., Davies R. L., 2017, *MNRAS*, **465**, 2101
- Owers M. S., et al., 2017, *MNRAS*, **468**, 1824
- Owers M. S., et al., 2019, *ApJ*, **873**, 52
- Pahre M. A., Djorgovski S. G., de Carvalho R. R., 1995, *ApJ*, **453**, L17
- Pahre M. A., Djorgovski S. G., de Carvalho R. R., 1998, *AJ*, **116**, 1591
- Peng C. Y., Ho L. C., Impey C. D., Rix H.-W., 2002, *AJ*, **124**, 266
- Planck Collaboration et al., 2016, *A&A*, **594**, A13
- Press W. H., Teukolsky S. A., Vetterling W. T., Flannery B. P., 2007, *Numerical recipes: The art of scientific computing*, 3rd edn. Cambridge Univ. Press, Cambridge, UK
- Prichard L. J., et al., 2017, *ApJ*, **850**, 203
- Prugniel P., Simien F., 1997, *A&A*, **321**, 111
- Renzini A., 1977, in Bouvier P., Maeder A., eds, *Saas-Fee Advanced Course 7: Advanced Stages in Stellar Evolution*. p. 151
- Riess A. G., et al., 2016, *ApJ*, **826**, 56
- Robotham A. S. G., Obreschkow D., 2015, *Publ. Astron. Soc. Australia*, **32**, e033
- Rousseeuw P. J., Driessen K., 2006, *Data Min. Knowl. Discov.*, **12**, 29
- Saglia R. P., et al., 2010, *A&A*, **524**, A6
- Saglia R. P., et al., 2016, *A&A*, **596**, C1
- Said K., Colless M., Magoulas C., Lucey J. R., Hudson M. J., 2020, *MNRAS*,
- Sánchez-Blázquez P., et al., 2006, *MNRAS*, **371**, 703
- Sánchez-Blázquez P., Forbes D. A., Strader J., Brodie J., Proctor R., 2007, *MNRAS*, **377**, 759
- Sánchez S. F., et al., 2012, *A&A*, **538**, A8
- Saracco P., Gargiulo A., La Barbera F., Annunziatella M., Marchesini D., 2020, *MNRAS*, **491**, 1777
- Schiavon R. P., 2007, *ApJS*, **171**, 146
- Scott N., et al., 2009, *MNRAS*, **398**, 1835
- Scott N., et al., 2015, *MNRAS*, **451**, 2723
- Scott N., et al., 2017, *MNRAS*, **472**, 2833
- Scott N., et al., 2018, *MNRAS*, **481**, 2299
- Scott N., et al., 2020, *MNRAS*, **497**, 1571
- Scrimgeour M. I., et al., 2016, *MNRAS*, **455**, 386
- Shanks T., et al., 2013, *The Messenger*, **154**, 38
- Shanks T., et al., 2015, *MNRAS*, **451**, 4238
- Sharp R., et al., 2006, in *Society of Photo-Optical Instrumentation Engineers (SPIE) Conference Series*. p. 62690G ([arXiv:astro-ph/0606137](https://arxiv.org/abs/astro-ph/0606137)), [doi:10.1117/12.671022](https://doi.org/10.1117/12.671022)
- Sharp R., et al., 2015, *MNRAS*, **446**, 1551
- Skilling J., 2004, in Fischer R., Preuss R., Toussaint U. V., eds, *American Institute of Physics Conference Series Vol. 735, Bayesian Inference and Maximum Entropy Methods in Science and Engineering: 24th International Workshop on Bayesian Inference and Maximum Entropy Methods in Science and Engineering*. pp 395–405, [doi:10.1063/1.1835238](https://doi.org/10.1063/1.1835238)
- Skilling J., 2006, *Bayesian Anal.*, **1**, 833
- Speagle J. S., 2020, *MNRAS*, **493**, 3132
- Speagle J. S., Steinhardt C. L., Capak P. L., Silverman J. D., 2014, *ApJS*, **214**, 15

- Springob C. M., et al., 2012, *MNRAS*, **420**, 2773
 Springob C. M., et al., 2014, *MNRAS*, **445**, 2677
 Taylor M. B., 2005, in Shopbell P., Britton M., Ebert R., eds, *Astronomical Society of the Pacific Conference Series Vol. 347, Astronomical Data Analysis Software and Systems XIV*. p. 29
 Taylor E. N., et al., 2011, *MNRAS*, **418**, 1587
 Thob A. C. R., et al., 2019, *MNRAS*, **485**, 972
 Thomas D., Maraston C., Bender R., Mendes de Oliveira C., 2005, *ApJ*, **621**, 673
 Thomas D., Maraston C., Schawinski K., Sarzi M., Silk J., 2010, *MNRAS*, **404**, 1775
 Tonry J. L., Blakeslee J. P., Ajhar E. A., Dressler A., 2000, *ApJ*, **530**, 625
 Trager S. C., Worthey G., Faber S. M., Burstein D., González J. J., 1998, *ApJS*, **116**, 1
 Vincent R. A., Ryden B. S., 2005, *The Astrophysical Journal*, **623**, 137
 Wolf J., Martinez G. D., Bullock J. S., Kaplinghat M., Geha M., Muñoz R. R., Simon J. D., Avedo F. F., 2010, *MNRAS*, **406**, 1220
 Woo J., Dekel A., Faber S. M., Koo D. C., 2015, *MNRAS*, **448**, 237
 Worthey G., Faber S. M., Gonzalez J. J., Burstein D., 1994, *ApJS*, **94**, 687
 Wright A. H., et al., 2016, *MNRAS*, **460**, 765
 Wu P.-F., et al., 2018, *ApJ*, **868**, 37
 Wuyts S., van Dokkum P. G., Kelson D. D., Franx M., Illingworth G. D., 2004, *ApJ*, **605**, 677
 Zaritsky D., Gonzalez A. H., Zabludoff A. I., 2006, *ApJ*, **638**, 725
 Zibetti S., Gallazzi A. R., Hirschmann M., Consolandi G., Falcón-Barroso J., van de Ven G., Lyubenova M., 2020, *MNRAS*, **491**, 3562
 da Cunha E., Charlot S., Elbaz D., 2008, *MNRAS*, **388**, 1595
 de Graaff A., et al., 2020, *ApJ*, **903**, L30
 de Zeeuw P. T., et al., 2002, *MNRAS*, **329**, 513
 van Dokkum P. G., Stanford S. A., 2003, *ApJ*, **585**, 78
 van Dokkum P. G., van der Marel R. P., 2007, *ApJ*, **655**, 30
 van Rossum G., 1995, CWI Technical Report, CS-R9526
 van de Sande J., Kriek M., Franx M., Bezanson R., van Dokkum P. G., 2014, *ApJ*, **793**, L31
 van de Sande J., et al., 2017a, *MNRAS*, **472**, 1272
 van de Sande J., et al., 2017b, *ApJ*, **835**, 104
 van de Sande J., et al., 2018, *Nature Astronomy*, **2**, 483
 van de Sande J., et al., 2020, arXiv e-prints, p. [arXiv:2011.08199](https://arxiv.org/abs/2011.08199)
 van der Wel A., Franx M., van Dokkum P. G., Rix H. W., 2004, *ApJ*, **601**, L5

APPENDIX A: NORMALISING A CENSORED 3-D GAUSSIAN

To calculate the normalisation factor f_i defined in equation (19), we introduce the matrix \mathbf{A}_i given by

$$\left(\mathbf{R}^T \boldsymbol{\Sigma} \mathbf{R} + \mathbf{E}_i\right)^{-1} \equiv \mathbf{A}_i^{-1} \equiv \begin{bmatrix} a_{11} & a_{12} & a_{13} \\ a_{21} & a_{22} & a_{23} \\ a_{13} & a_{23} & a_{33} \end{bmatrix} \quad (\text{A1})$$

where, for brevity, we dropped the dependence on i from the matrix elements. With this notation, the equation for f_i becomes

$$\frac{1}{f_i(L_{\min})} = \int_{-\infty}^{\infty} dx_1 \int_{-\infty}^{\infty} dx_2 \int_{\log L_{\min} - \mu_3}^{\infty} dx_3 \mathcal{N}_{\mathbf{0}, \mathbf{A}_i}(\mathbf{x}) \quad (\text{A2})$$

The argument of the exponential function in the Gaussian function above can be decomposed into the sum of three

squares as

$$\begin{aligned} -\frac{1}{2} \langle \mathbf{x}, \mathbf{A}_i^{-1} \mathbf{x} \rangle &= -\frac{1}{2} (\xi_1^2 + \xi_2^2 + \xi_3^2) \\ \xi_1 &\equiv \sqrt{a_{11}} x_1 + \frac{a_{12} x_2 + a_{13} x_3}{\sqrt{a_{11}}} \\ \xi_2 &\equiv \sqrt{a_{22} - \frac{a_{12}^2}{a_{11}}} x_2 + \frac{a_{23} - \frac{a_{12} a_{13}}{a_{11}}}{\sqrt{a_{22} - \frac{a_{12}^2}{a_{11}}}} x_3 \\ \xi_3 &\equiv \sqrt{a_{33} - \frac{a_{13}^2}{a_{11}} - \frac{\left(a_{23} - \frac{a_{12} a_{13}}{a_{11}}\right)^2}{a_{22} - \frac{a_{12}^2}{a_{11}}}} x_3 \equiv \sqrt{\mathcal{D}_i} x_3 \end{aligned} \quad (\text{A3})$$

We can therefore change variables in the multiple integral and, since the adopted change of variables has a Jacobian determinant equal to $\sqrt{\det \mathbf{A}_i}$, we get

$$\frac{1}{f_i(L_{\min})} = \int_{-\infty}^{\infty} d\xi_1 \int_{-\infty}^{\infty} d\xi_2 \int_{\sqrt{\mathcal{D}_i}(\log L_{\min} - \mu_3)}^{\infty} d\xi_3 \mathcal{N}_{\mathbf{0}, \mathbf{I}}(\boldsymbol{\xi}) \quad (\text{A4})$$

This readily evaluates to

$$\frac{1}{f_i(L_{\min})} = \frac{1}{2} \left[1 - \operatorname{erf} \left(\sqrt{\frac{\mathcal{D}_i}{2}} (\log L_{\min} - \mu_3) \right) \right] \quad (\text{A5})$$

and \mathcal{D}_i can be simplified to

$$\mathcal{D}_i = \frac{\det \mathbf{A}_i^{-1}}{a_{11} a_{22} - a_{12}^2} \quad (\text{A6})$$

It may also be useful to recall that, in the more general case where x_3 is censored at both extremes α and β , then

$$\frac{1}{f_i(L_{\min})} = \frac{1}{2} \left[\operatorname{erf} \left(\sqrt{\frac{\mathcal{D}_i}{2}} (\beta - \mu_3) \right) - \operatorname{erf} \left(\sqrt{\frac{\mathcal{D}_i}{2}} (\alpha - \mu_3) \right) \right] \quad (\text{A7})$$

Where more than one variable is censored, the integrating factor can be computed by Cholesky decomposition (see M12, their equation A3).

APPENDIX B: ORTHOGONAL VS DIRECT FORMULATION OF THE LEAST-SQUARES PROBLEM WITH CORRELATED, HETEROSCEDASTIC MEASUREMENT UNCERTAINTIES

In this section, we provide a formula to include correlated, heteroscedastic measurement uncertainties in the expression for the direct fit to 2-d and 3-d linear relations. While they may or may not be biased for galaxy-evolution studies, there is no questioning the importance of direct-fit methods to the FP use as a distance indicator. Because these methods minimise the uncertainty on the dependent variable from which distances are inferred, they also minimise the uncertainty on the FP-derived distances (e.g. Bernardi et al. 2003; Said et al. 2020). Despite this importance, we are not aware of any study providing the correct expression to include correlated uncertainties. For comparison, we also give the corresponding expressions for the orthogonal fit, even though these are

already available in the literature (Robotham & Obreschcow 2015).

Generally, in the FP literature, direct fits optimise the χ^2 defined by

$$\chi_{\text{direct}}^2 \equiv \sum_{i=0}^{N-1} \frac{(z_i - m x_i - b y_i - c)^2}{\sigma_{\text{int}}^2} \quad (\text{B1})$$

where a , b and c are the FP coefficients, σ_{int} is the intrinsic scatter along the z axis, and (x_i, y_i, z_i) , $i \in 0, \dots, N$, are the data. Orthogonal fits minimise

$$\chi_{\perp}^2 = \sum_{i=0}^{N-1} \frac{(z_i - a x_i - b y_i - c)^2}{\sigma_{\perp}^2 (a^2 + b^2 + 1)} \quad (\text{B2})$$

where σ_{\perp} is the FP intrinsic scatter, orthogonal to the FP. When adding uncorrelated measurement uncertainties $(\sigma_{x,i}, \sigma_{y,i}, \sigma_{z,i})$, the expression for χ_{\perp}^2 is generally modified to be

$$\chi_{\perp}^2 = \sum_{i=0}^{N-1} \frac{(z_i - a x_i - b y_i - c)^2}{\sigma_{\perp}^2 + \sigma_{z,i}^2 + a^2 \sigma_{x,i}^2 + b^2 \sigma_{y,i}^2} \quad (\text{B3})$$

However, we argue that this expression is properly appropriate to χ_{direct}^2 , with the substitution $\sigma_{\perp} \rightarrow \sigma_{\text{int}}$. This claim can be verified by considering the perfect symmetry between $\sigma_{z,i}$ (along the z axis) and σ_{\perp} (that should be orthogonal to the plane); clearly, if equation (B3) is to be the expression for χ_{\perp}^2 , these two terms cannot add in an unweighted quadrature: either σ_{\perp} must be projected along the z -axis or $\sigma_{z,i}$ must be projected orthogonal to the plane before they can be added in quadrature. Moreover, taking the limit $(\sigma_{x,i}, \sigma_{y,i}, \sigma_{z,i}) \rightarrow \mathbf{0}$, equation (B3) implies $\chi_{\perp}^2 \rightarrow \chi_{\text{direct}}^2$, which is incorrect (again, with the substitution $\sigma_{\perp} \rightarrow \sigma_{\text{int}}$).

Hence we propose to modify equation (B3) as follows

$$\chi_{\perp}^2 \equiv \sum_{i=0}^{N-1} \frac{(z_i - a x_i - b y_i - c)^2}{(a^2 + b^2 + 1) \sigma_{\perp}^2 + \langle (a, b, -1), \mathbf{E}_i(a, b, -1) \rangle} \quad (\text{B4})$$

which manifestly tends to the correct expression for χ_{\perp}^2 when measurement uncertainties are negligible. In vector notation, defining the unit normal to the plane as $\hat{\mathbf{n}} \equiv (a, b, -1)/\sqrt{a^2 + b^2 + 1}$, $d \equiv c/\sqrt{a^2 + b^2 + 1}$ as the orthogonal distance between the plane and the origin, and \mathbf{E}_i as the covariance matrix of measurement uncertainties, the expression becomes

$$\chi_{\perp}^2 \equiv \sum_{i=0}^{N-1} \frac{(\langle \hat{\mathbf{n}}, \mathbf{x}_i \rangle - d)^2}{\sigma_{\perp}^2 + \langle \hat{\mathbf{n}}, \mathbf{E}_i \hat{\mathbf{n}} \rangle} \quad (\text{B5})$$

which is rotationally symmetric. Similarly, the expression for the direct fit is

$$\chi_{\text{direct}}^2 \equiv \sum_{i=0}^{N-1} \frac{(z_i - a x_i - b y_i - c)^2}{\sigma_{\text{int}}^2 + \langle (a, b, -1), \mathbf{E}_i(a, b, -1) \rangle} \quad (\text{B6})$$

which, as it should be, cannot be written in rotationally-symmetric form, but has complete symmetry between σ_{int} and $\sigma_{z,i} = \sqrt{\langle \mathbf{E}_i \rangle_{z,z}}$. In principle, this expression can be derived from equation (29) of Kelly (2007), using the same approach as they use to derive the corresponding 2-d expression (their equation 24).

These expressions can be easily derived in the 2-d case, by considering the probability distribution of a 2-d Gaussian with uncorrelated scatter along two independent directions

\mathbf{v}_1 and \mathbf{v}_2 (direct fit) or along two orthogonal directions (orthogonal fit). If we write the Gaussian correlation matrix in the reference frame $[\mathbf{v}_1, \mathbf{v}_2]$ as

$$\Sigma \equiv \begin{bmatrix} \sigma_1^2 & 0 \\ 0 & \sigma_2^2 \end{bmatrix} \quad (\text{B7})$$

then the expressions for the 2-d analogues of the χ^2 can be obtained by maximising the likelihood function in the limit $\sigma_1 \rightarrow \infty$. If we write the transformation between the coordinates (v_1, v_2) and (x, y) as $\mathbf{v} = \mathbf{T}\mathbf{x}$, the probability of the data given the model can be written as

$$p(\mathbf{x}_i | \text{model}) = \prod_{i=0}^{N-1} \mathcal{N}_{\mu, \mathbf{T}^{-1} \Sigma (\mathbf{T}^T)^{-1} + \mathbf{E}_i}(\mathbf{x}_i) \quad (\text{B8})$$

where μ is the centroid and

$$\mathbf{T} \equiv \begin{bmatrix} 1/\cos \vartheta & 0 \\ -\sin \vartheta / \cos \vartheta & 1 \end{bmatrix} \quad (\text{B9})$$

if the scatter σ_2 is along the z axis (direct fit) whereas

$$\mathbf{T} \equiv \begin{bmatrix} \cos \vartheta & \sin \vartheta \\ -\sin \vartheta & \cos \vartheta \end{bmatrix} \quad (\text{B10})$$

if the scatter σ_2 is orthogonal to the line (orthogonal fit). The expression for $p(\mathbf{x}_i | \text{model})$ can be written explicitly. For each data point i , the argument of the Gaussian exponentials are (apart from a factor $-1/2$)

$$\chi_{i,\text{direct}}^2 \equiv \frac{(\sin \vartheta (x_i - \mu_x) - \cos \vartheta (y_i - \mu_y))^2}{\cos^2 \vartheta \sigma_{\text{int}}^2 + \sin^2 \vartheta \sigma_{x,i}^2 + \cos^2 \vartheta \sigma_{y,i}^2} - 2\rho_i \sin \vartheta \cos \vartheta \sigma_{x,i} \sigma_{y,i} \quad (\text{B11})$$

and

$$\chi_{i,\perp}^2 \equiv \frac{(\sin \vartheta (x_i - \mu_x) - \cos \vartheta (y_i - \mu_y))^2}{\sigma_{\perp}^2 + \sin^2 \vartheta \sigma_{x,i}^2 + \cos^2 \vartheta \sigma_{y,i}^2} - 2\rho_i \sin \vartheta \cos \vartheta \sigma_{x,i} \sigma_{y,i} \quad (\text{B12})$$

Notice that in the limit $\sigma_1 \rightarrow \infty$ the probability distribution $p(\mathbf{x}_i | \text{model})$ is no longer integrable. Using this distribution as a probability requires some truncation along x at a ‘large’ distance from the centroid μ . With this caveat, maximising the ‘probability’ of the ‘infinitely-extended’ Gaussian is akin to minimising the sum of the squares χ_i^2 (we neglect the normalisation factor). So the expression for χ_{direct}^2 in 2-d can be written either as

$$\chi_{\text{direct}}^2 = \sum_{i=0}^{N-1} \frac{(\sin \vartheta (x_i - \mu_x) - \cos \vartheta (y_i - \mu_y))^2}{\cos^2 \vartheta \sigma_{\text{int}}^2 + \sin^2 \vartheta \sigma_{x,i}^2 + \cos^2 \vartheta \sigma_{y,i}^2} - 2\rho_i \sin \vartheta \cos \vartheta \sigma_{x,i} \sigma_{y,i} \quad (\text{B13})$$

which reduces the bias for steep slopes, or in the more familiar form

$$\chi_{\text{direct}}^2 = \sum_{i=0}^{N-1} \frac{(a x_i + b - y_i)^2}{\sigma_{\text{int}}^2 + a^2 \sigma_{x,i}^2 + \sigma_{y,i}^2 - 2\rho_i a \sigma_{x,i} \sigma_{y,i}} \quad (\text{B14})$$

where $a = \tan \vartheta$ and $b = \mu_y - a \mu_x$ are the slope and zero-point of the line. The expressions for the orthogonal 2-d fit are

$$\chi_{\perp}^2 = \sum_{i=0}^{N-1} \frac{(\sin \vartheta (x_i - \mu_x) - \cos \vartheta (y_i - \mu_y))^2}{\sigma_{\perp}^2 + \sin^2 \vartheta \sigma_{x,i}^2 + \cos^2 \vartheta \sigma_{y,i}^2} - 2\rho_i \sin \vartheta \cos \vartheta \sigma_{x,i} \sigma_{y,i} \quad (\text{B15})$$

and

$$\chi_{\perp}^2 = \sum_{i=0}^{N-1} \frac{(a x_i + b - y_i)^2}{(1 + a^2) \sigma_{\perp}^2 + a^2 \sigma_{x,i}^2 + \sigma_{y,i}^2 - 2\rho_i a \sigma_{x,i} \sigma_{y,i}} \quad (\text{B16})$$

Clearly, some constraints on σ_{intr} and σ_{\perp} are required before minimising these expressions.

APPENDIX C: THE LTS_PLANEFIT ANALYSIS

If we repeat our analysis using the LTS_PLANEFIT algorithm instead of the 3dG algorithm we find a FP different to the fiducial FP (cf. Figs 9 and C1), as well as different slope and significance for the residual trends (as expected from the underlying probabilistic models, § 3.4; Figs C2, C3 and C4). However, the ranking of the most significant residual trends is the same between the two methods, so our conclusions are qualitatively the same and are not an artefact of the particular algorithm adopted. In Fig. C1 we show the LTS FP. The best-fit value of the coefficient $b = 0.896 \pm 0.024$ is statistically consistent with the 3dG equivalent, but both $a = 1.149 \pm 0.033$ and $c = 7.389 \pm 0.072$ are statistically different. The origin of this difference is due to different underlying models, yet the normal to the LTS FP is very close ($3.2 \pm 1.0^\circ$) to the normal to the fiducial FP (Table 2, column 5).

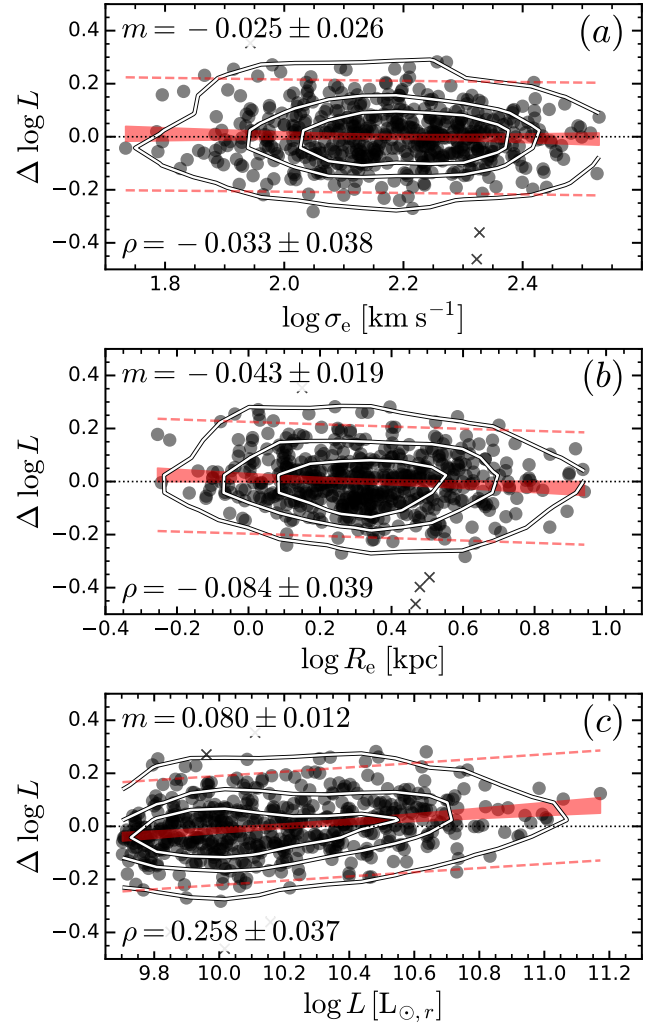


Figure C2. The residuals of the LTS FP exhibit the expected correlations with the FP observables: $\log \sigma_e$ (top), $\log R_e$ (middle) and $\log L$ (bottom). Each circle represents a SAMI galaxy; the white contours enclose the 90th, 67th and 30th percentiles of the distribution. The red line traces the best-fit linear relation; the red regions are the 95% confidence intervals and the dashed red lines are the 95% prediction intervals. The best-fit linear slope m and the Spearman rank correlation coefficient are reported at the top left and bottom left of each panel.

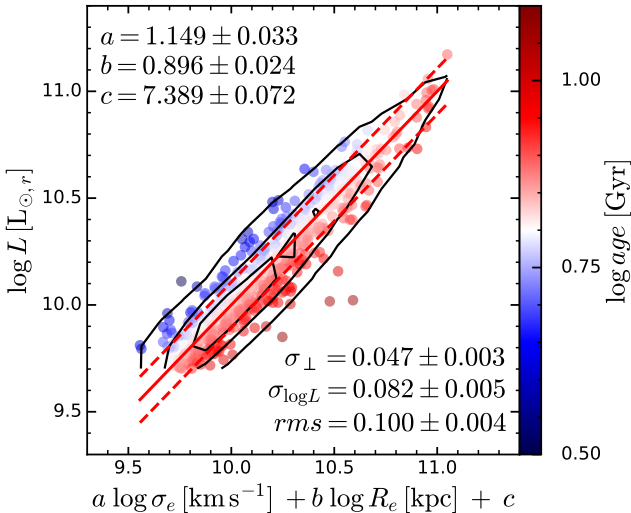


Figure C1. The LTS FP for the SAMI ETGs, showing a clear age gradient across the plane. Each circle represents a SAMI galaxy, colour-coded by the (LOESS-smoothed) SSP age. The best-fit FP is traced by the solid red line; the dashed red lines encompass $\pm rms$. The black contours enclose the 90th, 67th and 30th percentiles of the distribution. There is a clear age gradient across the FP: at fixed σ_e and R_e , old galaxies (red hues) are underluminous and tend to lie below the best-fit plane.

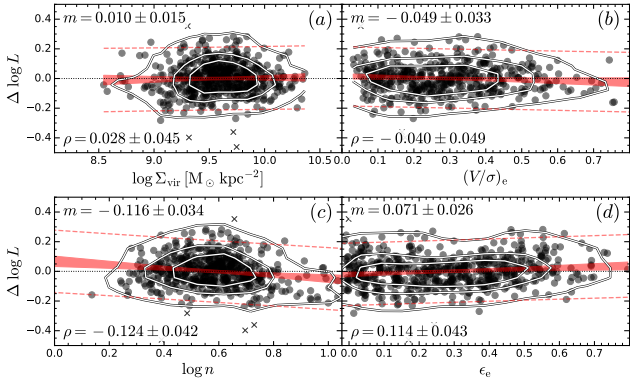


Figure C3. The residuals of the LTS FP have weak or no correlation with the structural observables considered here: dynamical surface mass density Σ_{vir} (panel a), $(V/\sigma)_e$ (panel b), Sérsic index (panel c) and projected ellipticity (d). The symbols are the same as in Fig. C2. We find evidence of a correlation only for n ($\approx 3\sigma$ significance).

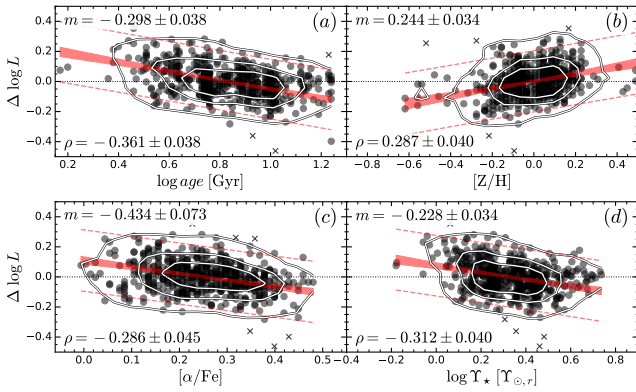


Figure C4. Like the residuals of the fiducial FP (Fig. 14), also the residuals of the LTS FP correlate most strongly with stellar population $\log \text{age}$ ($\approx 8\sigma$ significance; panel a). The other stellar population properties considered here all show significant correlations, including $[Z/H]$ (panel b), $[\alpha/\text{Fe}]$ (c) and $\log \Upsilon_*$ (d). The symbols are the same as in Fig. C2.

APPENDIX D: EXTINCTION ACROSS THE FUNDAMENTAL PLANE

The GAMA database provides two different SED fits, therefore two different values of the r -band extinction A_r . Given that the extinction measurements are very noisy, and are not present for the cluster galaxies, we proceed as follows.

We assume that extinction correlates primarily with stellar population age and inclination, so we start by smoothing the A_r distribution on the $\log \text{age}-\epsilon$ plane; we then interpolate the smooth distribution, and finally for each galaxy in the mock we infer the interpolated value of A_r . L_{synth} is then corrected down to account for the inferred extinction. The resulting FP has lower scatter, by 0.02 dex (when using $E(B-V)$ from Taylor et al. 2011) or by 0.01 dex (when using τ_V derived from MAGPHYS, da Cunha et al. 2008).

We conclude that extinction could play a role in the FP,

by reducing the scatter due to the spread in stellar population age, but given the available precision of the measurements of A_r , the inferred reduction is marginal.

This paper has been typeset from a $\text{T}_{\text{E}}\text{X}/\text{L}^{\text{A}}\text{T}_{\text{E}}\text{X}$ file prepared by the author.